

國立交通大學
環境工程研究所

博士論文

聚氯化鋁水解物種之混凝行為：膠體去穩定機制及膠羽形成分析

COAGULATION BEHAVIOR OF HYDROLYZED PACl SPECIES:
COLLOID DESTABILIZATION MECHANISMS AND
FLOCS FORMATION ANALYSIS

研究生：林志麟

指導教授：黃志彬 博士

中華民國九十七年七月

聚氯化鋁水解物種之混凝行為：膠體去穩定機制及膠羽形成分析

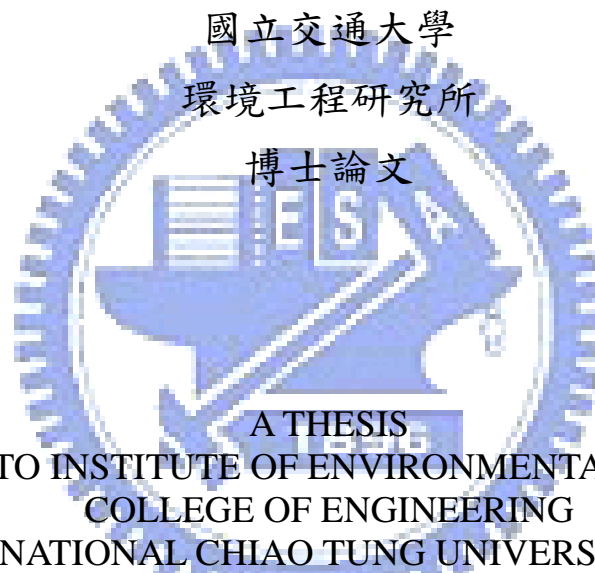
COAGULATION BEHAVIOR OF HYDROLYZED PACl SPECIES:
COLLOID DESTABILIZATION MECHANISMS AND
FLOCS FORMATION ANALYSIS

研究生：林志麟

Student : Jrlin Lin

指導教授：黃志彬 博士

Advisor : Dr. Chihpin Huang



A THESIS
SUBMITTED TO INSTITUTE OF ENVIRONMENTAL ENGINEERING
COLLEGE OF ENGINEERING
NATIONAL CHIAO TUNG UNIVERSITY
IN PARTIAL FULFILLMENT OF THE REQUIREMENTS
FOR THE DEGREE OF
DOCTOR OF PHILOSOPHY
IN
ENVIRONMENTAL ENGINEERING

JULY 2008

HSINCHU, TAIWAN, REPUBLIC OF CHINA

中華民國九十七年七月

聚氯化鋁水解物種之混凝行為：膠體去穩定機制及膠羽形成分析

研究生：林志麟

指導教授：黃志彬 博士

國立交通大學環境工程研究所

摘要

在水及廢水處理過程中，聚氯化鋁(PACl)是最常被使用於混凝程序以去穩定顆粒之混凝劑。聚氯化鋁混凝劑之效用取決於水解物種與水中顆粒間之作用。水解的鋁物種如聚合鋁及氫氧化鋁會嚴重地影響膠體顆粒之混凝機制，然後會影響膠羽的形成。因為水解鋁物種會隨 pH 及總鋁濃度改變，故瞭解各種聚氯化鋁混凝劑之鋁形態分佈及在各 pH 值與加藥量下之主要水解鋁物種對於 PACl 之應用相當重要。

首先，以瓶杯試驗及Ferron法評估混凝過程中各種鋁水解物種對高嶺土顆粒去穩定之影響，並利用即時的診斷技術探究膠羽的形成及表面結構。同時，進行膠羽表面之鋁元素組成分析。此外，藉由輕敲式原子力顯微鏡及濕式掃描式電子顯微鏡觀察 Al_{13} 聚集體與氫氧化鋁之表面結構。

在中性條件下，無論加藥量多寡，PACl-C混凝膠羽之形成主要依賴氫氧化鋁沉澱物。相對的，在鹼性條件下，具有高 Al_{13} 含量之PACl-E主要以 Al_{13} 聚集體行電性補釘及電性中和之混凝機制。在鹼性及低加藥量條件下，高純度聚氯化鋁(PACl- Al_{13})混凝主要以電性補釘去穩定顆粒；在足夠加藥量下，由於具有電中性之 Al_{13} 聚集體形成促使顆粒間架橋變成主要的混凝機制。

在沉澱絆除或掃除機制及電性補釘機制下形成之膠羽，隨著加藥量增加，膠羽結構變成較密實，此時膠羽遭遇破碎會增加膠羽之碎形維度。相反地，PACl- Al_{13} 混凝之膠羽結構隨著加藥量增加而變鬆散。另一方面，沉澱絆除或掃除機制下形

成之膠羽具有粗糙的外觀，而電性補釘及電性中和機制下形成之膠羽具有光滑的表面。PACl-Al₁₃混凝所形成之架橋作用會造成鬆散的結構且毛茸的外觀。此條件下，存在一些由盤繞的Al₁₃所構成之線條狀Al₁₃聚集體與其他碎形結構之Al₁₃聚集體。

本質上，富含氫氧化鋁的膠羽不具有良好的晶形結構，而含有Al₁₃聚集體膠羽則具有類似Al₁₃的晶形結構。在富含氫氧化鋁的膠羽表面上，有許多無定形結晶之氫氧化鋁沉澱物具有四面體或八面體結構，而膠體狀之氫氧化鋁具有凹陷的表面。在鹼性條件下，Al₁₃聚集體被證實存在於PACl-Al₁₃之混凝膠羽表面。



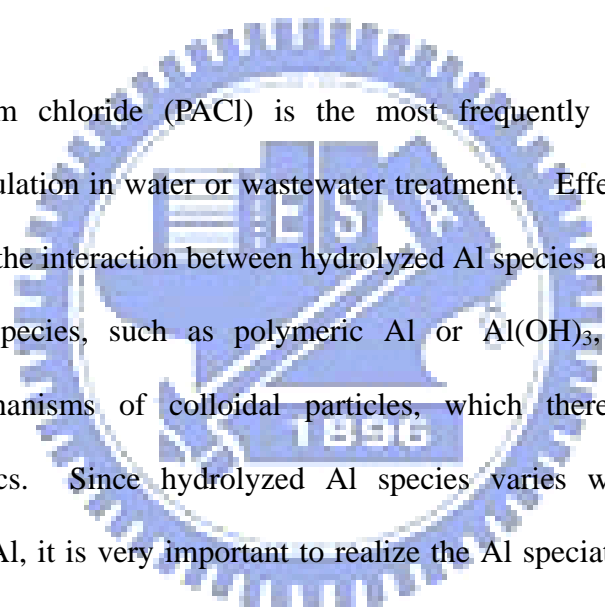
Coagulation Behavior of Hydrolyzed PACl Species: Colloid Destabilization Mechanisms and Flocs Formation Analysis

Student: Jrlin Lin

Advisor: Dr. Chihpin Huang

Institute of Environmental Engineering
National Chiao Tung University

ABSTRACT



Polyaluminum chloride (PACl) is the most frequently used to destabilize particles for coagulation in water or wastewater treatment. Effective coagulation by PACl depends on the interaction between hydrolyzed Al species and particles in water. Hydrolyzed Al species, such as polymeric Al or $\text{Al}(\text{OH})_3$, affect significantly coagulation mechanisms of colloidal particles, which thereafter influence the formation of flocs. Since hydrolyzed Al species varies with pH as well as concentration of Al, it is very important to realize the Al speciation of various PACl coagulants, and their predominant hydrolyzed Al species at various pH values and dosages for coagulation in practice.

Effects of various hydrolyzed Al species on the destabilization of kaolin particles in coagulation were evaluated by jar test as well as Ferron method. Formation of and structure of flocs were also investigated via an in-situ diagnostic technology. In-situ morphology of the flocs formed after coagulation was viewed through a wet SEM assay, and the Al composition of these flocs were further surveyed by XPS. Moreover, in-situ configuration of the Al_{13} aggregates as well as $\text{Al}(\text{OH})_3$ precipitates were also observed by TM-AFM and WSEM, respectively.

The formation of sweep flocs by PACl-C coagulation at neutral pH relied on $\text{Al}(\text{OH})_3$ precipitates regardless of the dosage applied. By contrast, the PACl-E containing a high percentage of Al_{13} caused either electrostatic patch or charge neutralization mechanisms with Al_{13} aggregates at alkaline pH. For high-purity PACl (PACl- Al_{13}) coagulation, electrostatic patch was responsible for particle destabilization at alkaline pH and low dosage. Interparticle bridging becomes the major mechanism at sufficient dosage due to the formation of Al_{13} aggregates with nearly zero charge.

The structure of flocs formed by enmeshment or sweep flocculation and electrostatic patch becomes more compact with dosage, in which the breakage of flocs increases the fractal dimension of flocs. On the contrary, flocs coagulated by PACl- Al_{13} become looser with dosage. On the other hand, enmeshment or sweep flocculation caused sweep flocs with a rough and ragged contour, while electrostatic patch or charge neutralization induced flocs with a smooth and glossy surface. PACl- Al_{13} coagulation induced by interparticle bridging brought the flocs of a looser structure with a fluffy contour. At such condition, some larger linear Al_{13} aggregates composed of a chain of coiled Al_{13} and several coiled Al_{13} aggregates with different dimensions can be observed.

Intrinsically, the $\text{Al}(\text{OH})_3$ -rich flocs do not possess well-formed crystalline structure, while the Al_{13} -aggregate flocs possess a Al_{13} -like crystalline structure. There are multitude of amorphous $\text{Al}(\text{OH})_3$ precipitates that involve either tetrahedral $\text{Al}^{\text{IV}}(\text{O})_4$ or octahedral $\text{Al}^{\text{VI}}(\text{O})_6$ center on the surface of $\text{Al}(\text{OH})_3$ -rich flocs, while the colloidal $\text{Al}(\text{OH})_{3(s)}$ has a sunken surface. It has been proved that the existence of Al_{13} aggregates on the surface of flocs coagulated by PACl- Al_{13} at alkaline pH.

誌 謝

「透過人生的孤寂，到達成功的彼岸」，這句話是中學時老師勉勵同學的話。在五年的交大求學歲月中，孤寂陪伴我度過無數撰寫研究計畫、報告及研讀學術論文的日子。在此過程中，感謝黃志彬教授於研究報告撰寫上的教導及鞭策，使我能學術研究的表達上有所進步。同時，感謝袁如馨老師對學生的細心關懷及鼓勵，在學生求學過程中遭遇困難時，給予莫大的幫助。此外，要感謝秦靜如老師在學術研究及論文撰寫上的協助，並能在忙碌的教學及研究外，撥空與學生討論研究的方向及實驗的規劃。口試期間，承蒙葉宣顯教授、康世芳教授、李篤中教授及張淑閔老師對本論文的撰寫提供寶貴的意見，使學生受益良多。

在博士班的修業過程中，感謝阿甘學長、佳欣、容忍、柏廷、肇毅、韋弘、宏杰、欣慧、育俊、文彬、奕甫、嘉玲、靜逸、璧如、雅茹（OK）及伶秀（狗狗）等學弟妹於研究工作上的協助與幫忙，使我能順利完成研究計畫及報告的工作。在生活上，感謝昌郁、政倫及文善在研究之餘的陪伴及關心，使我能忘卻煩惱，勇往直前。此外，感謝中國科學院生態環境研究中心曲久輝教授及王東升教授熱心提供高純度聚氯化鋁混凝劑，特別感謝王東升教授在膠體混凝研究上的啟發。同時，亦感謝中國科學院生態環境研究中心李濤博士對於本論文實驗規劃上的幫忙。

在個人成長及求學過程中，最感謝爸爸及媽媽對我的支持及鼓勵，以及奶奶的關心，讓我能一路從小到大無後顧之憂的唸書。感謝康世芳教授對學生的鼓勵，使我能完成博士學位。感謝靖宜在博士班修業最後一年中於論文撰寫上的幫忙及生活上的照顧，使我能順利完成學業。最後，僅將完成此論文的喜悅獻給我的家人及身邊的朋友，願你們與我分享。

CONTENTS

摘要.....	I
ABSTRACT.....	III
誌謝.....	V
CONTENTS.....	VI
LIST OF TABLES.....	IX
LIST OF FIGURES.....	X
CHAPTER I INTRODUCTION.....	1
1.1 Background.....	1
1.2 Scope and objectives.....	4
1.3 Outlines.....	5
CHAPTER II LITERATURE REVIEW.....	8
2.1 Characterization of Aluminum Coagulants.....	8
2.1.1 Chemistry of Hydrolyzing Aluminum.....	9
2.1.2 Identification of Hydrolyzing Aluminum Species.....	12
2.1.3 Synthesis and Characteristics of Al ₁₃	14
2.2 Alum Coagulation.....	18
2.2.1 Colloidal Interaction Forces.....	19
2.2.2 Mechanisms of Coagulation.....	22
2.3 Coagulation Dynamics.....	28
2.3.1 Floc Formation.....	29
2.3.2 Floc Breakage and Restructuring.....	31
2.4 Floc Physical Characteristics.....	33
2.4.1 Floc Size.....	34
2.4.2 Fractal Dimension.....	35
2.4.3 Floc Strength.....	37
2.5 Surface Observation by Atomic Force Microscopy.....	38
CHAPTER III EXPERIMENTAL MATERIALS AND METHODS.....	41
3.1 Materials.....	41
3.1.1 Synthetic Water Sample.....	41
3.1.2 Coagulants.....	43
3.2 Methods.....	44

3.2.1	Ferron Assay.....	44
3.2.2	²⁷ Al-Nuclear Magnetic Resonance (NMR).....	47
3.2.3	Preparation and Characterization of PACl-Al ₁₃	48
3.2.4	Coagulation Experiments.....	54
3.2.5	Measurement of Floc Size and Structure.....	57
3.2.6	Solid-state ²⁷ Al Magic-angle Spinning Nuclear Magnetic Resonance.....	59
3.2.7	Wet Scanning Electron Microscope.....	60
3.2.8	Atomic Force Microscope.....	62
3.2.9	Field-Emission Electron Microscope.....	63
3.2.10	High-resolution X-ray Powder Diffractometer.....	63
3.2.11	Fourier Transform Infrared Spectra.....	63
3.2.12	X-ray Photoelectron Spectroscopy.....	64

CHAPTER IV EFFECT OF Al SPECIES TRANSFORMATION ON COLLOID DESTABILIZATION MECHANISMS.....65

4.1	Effects of pH on Coagulation.....	65
4.1.1	Characterization of Coagulants.....	66
4.1.2	Effects of pH on Turbidity Removal.....	68
4.1.3	Effects of pH on Al Speciation in Coagulation.....	70
4.1.4	Effects of Al Speciation on Particle Destabilization Mechanisms.....	72
4.2	Effects of Dosage on Coagulation Efficiency.....	74
4.2.1	Effects of Dosage on Particle Destabilization.....	74
4.2.2	Reactive Al Species of Floccs.....	79
4.3	Summary.....	82

CHAPTER V FORMATION AND STRUCTURE OF FRACTAL FLOCS INDUCED BY VARIOUS DESTABILIZATION MECHANISMS.....83

5.1	Dynamic Growth of Al-Floc.....	84
5.2	Fractal Structure of Al-Flocs.....	88
5.2.1	Effects of Dynamic Growth of Floc on Fractal Structure.....	88
5.2.2	In-situ Observation on the Morphology of Floccs.....	94
5.3	In-situ Observation on the Morphology of Al ₁₃ Aggregates.....	97
5.4	Predominant Destabilization Mechanisms Model.....	101
5.5	Summary.....	105

CHAPTER VI SURFACE Al COMPOSITION OF Al(OH)₃-RICH AND Al₁₃-AGGREGATE FLOCS.....106

6.1	Structure of Al-Flocs.....	107
-----	----------------------------	-----

6.1.1	Surface structure of Floccs.....	107
6.1.2	Crystalline Structure of Floccs.....	111
6.2	In-situ Observation of Al(OH) ₃ Precipitates.....	113
6.3	Surface Composition of Al-Floccs.....	115
6.4	Summary.....	119
CHAPTER VII CONCLUSIONS AND RECOMMENDATIONS.....		120
7.1	Conclusions.....	120
7.2	Recommendations.....	122
BIBLIOGRAPHY.....		123

VITA



LIST OF TABLES

Table 2.1	Summary of thermodynamic data for Al hydrolysis reactions (25°C).....	10
Table 3.1	FTIR vibrational assignment of Al ₁₃ powder.....	53
Table 4.1	Characteristics of coagulants by Ferron assay and ²⁷ Al-NMR methods...	67
Table 5.1	Fractal dimension (<i>D_s</i>) of various flocs during coagulation.....	93

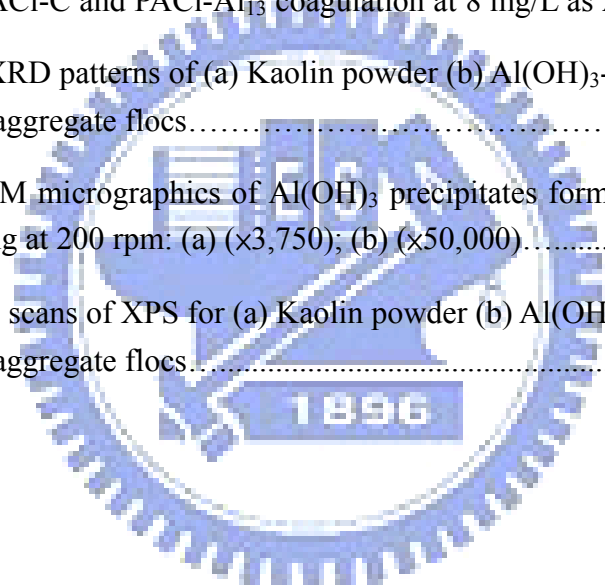


LIST OF FIGURES

Figure 1.1	Schematic diagram of this thesis.....	7
Figure 2.1	Solubility of amorphous aluminum hydroxide.....	11
Figure 2.2	Polymerization of $\text{Al}_2(\text{OH})_2^{4+}$	11
Figure 2.3	The ϵ -Keggin structure of Al_{13} polycation.....	16
Figure 2.4	Schematic diagram of coagulation process: (a) coagulant hydrolysis (b) destabilization of colloidal particles, and (c) aggregation of destabilized colloidal particles.....	18
Figure 2.5	Potential energy versus distance profiles of DLVO interactions. (a) van der Waals and electrostatic forces (b) primary-minimum of the potential energy (c) secondary-minimum of the potential energy and (d) potential energy of a stable suspended particles.....	21
Figure 2.6	Electrostatic patch model of the interaction between negatively charged particles and adsorbed cationic polymers.....	24
Figure 2.7	Fractal flocs formed by (a) particle-cluster aggregation (b) cluster-cluster aggregation.....	30
Figure 2.8	Two proposed mechanisms for the breakage of aggregates at different shear conditions: (a) Splitting (b) Surface Erosion.....	32
Figure 2.9	Schematic diagram of atomic force microscope.....	38
Figure 2.10	Illustration of the interaction force between tip-to-sample surface distance.....	39
Figure 3.1	SEM micrographics of purified kaolin powders.....	42
Figure 3.2	Particle size distribution of the kaolin suspension	42
Figure 3.3	Illustration of Ferron colorimetric method.....	46
Figure 3.4	The SEM images of $\text{Al}_{13}\text{-(SO}_4)_n$ precipitate ($\times 700$).....	49
Figure 3.5	Solid-state ^{27}Al -NMR spectrum of solid Al_{13} powder.....	52
Figure 3.6	HR-XRD pattern of solid Al_{13} powder.....	52
Figure 3.7	FTIR spectra of Al_{13} powder.....	53

Figure 3.8	G curve for flat paddle in the gator jar.....	56
Figure 3.9	Construction of laboratory coagulation system incorporated with SASLS.....	57
Figure 3.10	Setup of WSEM: (a) Top scheme of QX-102 capsule and (b) Cross-section scheme of capsule.....	61
Figure 3.11	Setup of liquid tapping mode atomic force microscope.....	63
Figure 4.1	²⁷ Al-NMR spectra of (a) PACl-C (b) PACl-E (c) PACl-Al ₁₃	67
Figure 4.2	The residual turbidity and the zeta potential for (a) PACl-C (7% Al ₁₃) (b) PACl-E (60% Al ₁₃) and (c) PACl-Al ₁₃ (96% Al ₁₃) coagulation at various pH values and 1mg/L as Al.....	69
Figure 4.3	Al speciation of (a) PACl-C (b) PACl-E (c) PACl-Al ₁₃ at various pH values under the concentration of 2×10 ⁻⁴ mol Al/L.....	71
Figure 4.4	Dosage effects on the residual turbidity and the zeta potential for (a) PACl-C (7% Al ₁₃) coagulation at pH 7.5 (b) PACl-E (60% Al ₁₃) and (c) PACl-Al ₁₃ (96% Al ₁₃) coagulation at pH 10.....	77
Figure 4.5	The zeta potential of Al species for PACl-Al ₁₃ coagulation at pH 10 and various dosages without kaolin particles.....	78
Figure 4.6	Solid-state ²⁷ Al MAS-NMR spectra of freeze-dried kaolin flocs coagulated by three coagulants at various dosages. PACl-C:(a) 1 mg/L (b) 8 mg/L; PACl-E:(c) 1 mg/L (d) 8 mg/L; PACl-Al ₁₃ :(e) 1 mg/L (f) 8 mg/L.....	81
Figure 5.1	The particle aggregation dynamics induced by (a) PACl-C coagulation at pH 7.5 and (b) PACl-E and (c) PACl-Al ₁₃ coagulation at pH 10.....	87
Figure 5.2	The fractal dimensions (<i>D_s</i>) of flocs coagulated by (a) PACl-C at pH 7.5 and (b) PACl-E and (c) PACl-Al ₁₃ at pH 10 and various dosages.....	92
Figure 5.3	The WSEM micrographics of flocs coagulated at various coagulants and dosages under 1 min rapid mixing followed by 20 min slow mixing. PACl-C: (a) 1mg/L and (b) 8 mg/L; PACl-E: (c) 1 mg/L and (d) 8 mg/L; PACl-Al ₁₃ : (e) 1 mg/L and (f) 8 mg/L.....	96
Figure 5.4	TM-AFM topographic image of the Al ₁₃ adsorbed on the mica in liquid system for PACl-Al ₁₃ coagulation at 8 mg/L and pH 10 without kaolin particles. (a) and (b) two-dimension (c) three-dimension.....	99

Figure 5.5	Size distributions of Al_{13} in PACl- Al_{13} coagulation without kaolin particles at various dosages (rapid mixing: 200 rpm; reaction time: 1 min).....	100
Figure 5.6	Schematic representation of the destabilization mechanism induced by PACl-C coagulation at neutral pH. (a) Precipitation Charge Neutralization (b) Enmeshment.....	103
Figure 5.7	Schematic representation of the destabilization mechanism induced by Al_{13} aggregates. (a) Electrostatic Patch (b) Interparticle Bridging.....	104
Figure 6.1	SEM micrographics of $Al(OH)_3$ -rich and Al_{13} -aggregate flocs formed by PACl-C and PACl- Al_{13} coagulation at 8 mg/L as Al.....	109
Figure 6.2	HR-TEM images of (a) $Al(OH)_3$ -rich and (b) Al_{13} -aggregate flocs formed by PACl-C and PACl- Al_{13} coagulation at 8 mg/L as Al.....	110
Figure 6.3	HR-XRD patterns of (a) Kaolin powder (b) $Al(OH)_3$ -rich and (c) Al_{13} -aggregate flocs.....	112
Figure 6.4	WSEM micrographics of $Al(OH)_3$ precipitates formed after 1 min rapid mixing at 200 rpm: (a) ($\times 3,750$); (b) ($\times 50,000$).....	114
Figure 6.5	Al 2p scans of XPS for (a) Kaolin powder (b) $Al(OH)_3$ -rich and (c) Al_{13} -aggregate flocs.....	118



CHAPTER I

INTRODUCTION

1.1 Background

In water or wastewater treatment, coagulation process is most commonly applied as an essential pretreatment process to destabilize colloidal material and suspended impurities, including organic and inorganic substances, for subsequent removal by separation processes such as sedimentation, flotation and filtration. Coagulation usually requires the addition of chemicals, namely coagulant, as an aid to the aggregation of particles for particle removal. Hydrolyzed metal salts such as aluminum and ferric salts are regularly used as coagulants, particularly alum and polyaluminum chloride (PACl). After the addition of aluminum coagulants, the hydrolysis reactions form a series of soluble ionic species, including monomeric and polymeric aluminum species, and solid precipitates. Because an efficient coagulation is required to yield colossal and compact flocs through the destabilization of colloidal particles with various hydrolyzed aluminum species for subsequent rapid separation of flocs from water, the aggregation process such as growth and breakup of flocs affects the coagulation efficiency significantly. However, the production of flocs mainly depends on the interaction of destabilized colloidal particles in coagulation. Therefore, it is essential to understand the physicochemical reactions between the colloidal particles and hydrolyzed aluminum species of PACl in order to clarify the predominant mechanism of coagulation in practice.

Chemistry of alum and PACl coagulants have been extensively studied, and various hydrolyzed aluminum species in water are proposed and suggested. PACl is the most frequently used to destabilize particles for coagulation in water or

wastewater treatment. Effective coagulation by PACl depends on the interaction between hydrolyzed aluminum species and colloidal particles in water. Many studies have proved that Al(III) species is driven into various hydrolyzed Al species such as $[\text{Al}(\text{OH})]^+$, $[\text{Al}(\text{OH})]^{2+}$, $[\text{Al}_2(\text{OH})_2]^{4+}$, $[\text{Al}_3(\text{OH})_4]^{5+}$, $[\text{Al}_{13}\text{O}_4(\text{OH})_{24}(\text{H}_2\text{O})_{12}]^{7+}$, and aluminum hydroxide ($\text{Al}(\text{OH})_3$) in the hydrolysis process, which are governed by the $[\text{OH}^-]/[\text{Al}]$ ratio (Akitt and Fathing, 1981; Bertsch et al., 1986b; Bottero et al., 1987). Poor performance of aluminum coagulants has been blamed on its low content in critical hydrolysis products, especially the polycationic aluminum (Al_{13}). Al_{13} is the highly charged polymeric aluminum species, $[\text{AlO}_4\text{Al}_{12}(\text{OH})_{24}(\text{H}_2\text{O})_{12}]^{7+}$, which has been commonly acknowledged as the critical species in colloidal particles coagulation by strong charge neutralization that facilitates the solid-liquid separation process (Gao et al., 2005; Wang and Hsu, 1994). In the past decade, a PACl with over 70% Al_{13} of total Al concentration has been produced by controlling the $[\text{OH}^-]/[\text{Al}]$ ratio during the preparation of PACl (Liu et al., 1999; Wang et al., 2004). PACl containing over 90% Al_{13} has also been successfully prepared by sulfate precipitation and nitrate metathesis ($\text{SO}_4^{2-}/\text{Ba}^{2+}$ separation method) from the pre-hydrolyzed PACl solution produced by alkaline titration method (Shi et al., 2007). However, the stabilization of hydrolyzed Al species have a profound effect on coagulation mechanisms that is closely related to the formation of flocs as well as particles removal.

Different aqueous Al species possessing different specific hydroxo-Al structure deprotonate with pH. Al(III) species transforms into voluminous amorphous aluminum hydroxide ($\text{Al}(\text{OH})_{3(\text{am})}$) at neutral pH (Van Benschoten and Edzwald, 1990), while Al_{13} is metastable with respect to $\text{Al}(\text{OH})_3$ and transforms to various $\text{Al}(\text{OH})_3$ such as gibbsite and bayerite over time upon the hydrolysis process

(Violante and Huang, 1985; Bradley et al., 1993). The condensation of Al_{13} could form at a specific pH due to shear-induced mixing (Furrer et al., 2002). During condensation, Al_{13} can transform into various Al_{13} aggregates with increasing $[OH^-]/[Al]$ ratio and total Al concentration (Bottero et al., 1987). On the contrary, Al_{13} aggregates can be decomposed by H^+ as the pH value decreases (Furrer et al., 1992). Furthermore, different oxygen sites of Al_{13} have different water exchange rates which relate to decomposition and condensation of Al_{13} (Phillips et al., 2000), resulting in various Al_{13} aggregates. However, there are many debates on the formation pathway of the Al_{13} aggregates, which depends on the reaction conditions such as Al concentration, pH, temperature, and aging processes (Sposito, 1996).

Many researchers have clarified that coagulation mechanisms of various PACl coagulants for the removal of colloid particles or organic matter (Gao et al., 2005; Hu et al., 2006; Kazpard et al., 2006; Yan et al., 2007), involving charge neutralization, complexation, and enmeshment (sweep flocculation). Moreover, it has been inferred that Al_{13} aggregates could destabilize particles by either electrostatic patch or bridging when PACl containing high Al_{13} contents is applied at high pH and sufficient dosage (Chen et al., 2006; Ye et al., 2007; Wu et al., 2007). However, these assumptions have never been verified and could not accurately illustrate the coagulation behavior of Al_{13} aggregates because it is a formidable task to quantify the Al_{13} aggregates. For the application of PACl in water or wastewater treatment, further investigations on the unknown hydrolyzed Al species, particularly Al_{13} aggregates, and their real conformations and composition during coagulation are dearly necessary to identify the predominant interaction between various hydrolyzed Al species and colloidal particles.

1.2 Scope and Objectives

The overall goals of the research presented in this thesis are to provide in-depth understanding of particles interaction in coagulation with various PACl coagulants. Effects of various hydrolyzed Al species on the destabilization of kaolin particles in coagulation were evaluated by jar tests, and the growth of flocs was also studied via in-situ diagnostic technology. In-situ observation of flocs formed after coagulation was conducted through a novel wet scanning electron microscope (WSEM) assay. Configuration of the Al_{13} aggregates as well as $Al(OH)_3$ precipitates were also observed by using tapping mode atomic force microscope (TM-AFM) and WSEM in liquid system, respectively. Several surface analysis technologies, including scanning electron microscope (SEM), high-resolution transmission electron microscope (HR-TEM), high-resolution X-ray powder diffractometer (HR-XRD), X-ray photoelectron spectroscopy (XPS), were employed to further survey the Al composition on the surface of $Al(OH)_3$ -rich and Al_{13} -aggregate flocs in order to comprehend the characteristics of hydrolyzed Al species thoroughly. The specific objectives for this research are summarized as follows:

1. To investigate the effects of Al(III) speciation on the predominant destabilization mechanism.
2. To study dynamic growth and structure of Al-flocs formed under various destabilization mechanisms.
3. To determine the role of Al_{13} aggregates in colloid coagulation.
4. To identify the composition of reactive Al species on the surface of $Al(OH)_3$ -rich and Al_{13} -aggregate flocs.

1.3 Outlines

Chapter I present the background and motivation of this research. The scope and objectives of this work are discussed. A literature review pertinent to this study, including Al hydrolysis chemistry, coagulation mechanisms, coagulation dynamics, characteristics of flocs and the application of AFM on surface observation, is presented in Chapter II.

Chapter III describes the experimental materials and methods, and the procedures of this study. A recipe for the analysis of Al speciation is presented. The preparation process of high-purity PACl was investigated. Liquid TM-AFM was developed to in-situ observe the aggregated Al_{13} molecules in an aqueous environment. The coagulation efficiency of various PACl coagulants as well as coagulation dynamics of fractal flocs was evaluated. Also, the surface Al composition of coagulated flocs was examined.

The major content of this thesis is shown as **Fig. 1.1**. Chapter IV highlights the effects of Al species transformation on the predominant destabilization mechanisms. The effects of various parameters (i.e., pH, Al speciation, and dosage) on particle destabilization mechanisms were identified. Various destabilization mechanisms by PACl were postulated from the results of coagulation experiments and the analysis of Al species transformation.

Effects of coagulation dynamics on the formation and structure of flocs induced by various destabilization mechanisms were explored in Chapter V. Dynamic particles aggregation and breakages of flocs were evaluated by small angle static light scattering (SASLS) to monitor the growth profile of coagulated flocs. Characteristics of flocs such as d_{50} size, mean size and fractal dimension during coagulation process were also determined, and the flocs were viewed by WSEM. In

addition, the morphology of Al_{13} aggregates was scanned by TM-AFM in liquid environment. Potential coagulation behavior of $Al(OH)_3$ precipitates as well as Al_{13} aggregates was proposed.

Surface Al composition of $Al(OH)_3$ -rich and Al_{13} -aggregate flocs were estimated by surface analysis technology in Chapter VI. The results of SEM and HR-TEM imaging were compared. The morphology of $Al(OH)_3$ precipitates were in-situ observed by WSEM. The crystalline structure of $Al(OH)_3$ -rich and Al_{13} -aggregate flocs were identified by HR-XRD. The tetrahedral and octahedral Al on the surface of $Al(OH)_3$ -rich and Al_{13} -aggregate flocs were identified via XPS survey. Finally, conclusions and recommended future investigations are stated in Chapter VII.



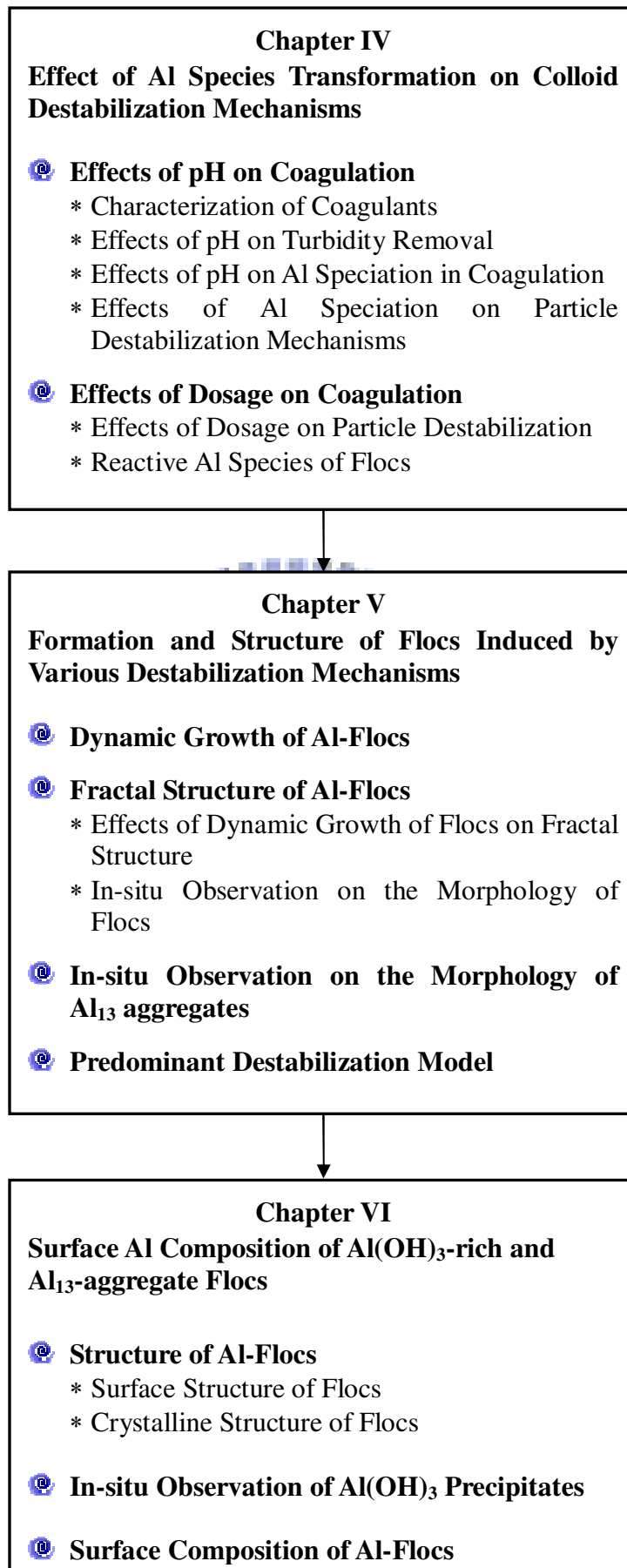


Fig. 1.1 Schematic diagram of this thesis.

CHAPTER II

LITERATURE REVIEW

The aims of coagulation with aluminum coagulants in water or wastewater treatment are mainly focused on destabilization and aggregation of colloidal particles. Aggregation of colloidal particles and the breakage of flocs are affected by the interaction forces between particles after the addition of coagulants. Colloidal interaction forces depend on the interactions of aluminum coagulant species present during coagulation with particles in water. In this section, the literatures related to the chemistry of aluminum coagulant in aqueous system, the behavior of particles aggregation and breakup of flocs during coagulation, the interparticle forces in liquid system and the application of atomic force microscope (AFM) on surface observation are reviewed.

2.1 Characterization of Aluminum Coagulants

Inorganic aluminum coagulants are commonly used to aggregate the colloidal particles in water or wastewater treatment. In general, they can be divided into aluminum salts and partially neutralized aluminum salts (i.e., polymeric aluminum coagulants). Aluminum coagulants speciation is governed by the hydrolysis characteristics of aqueous Al(III). Alum corresponds to a series of monomeric aluminum species in equilibrium with an amorphous or crystalline aluminum hydroxide precipitate ($\text{Al}(\text{OH})_3$). Polymeric aluminum coagulants such as polyaluminum chloride (PACl) are partially neutralized during prehydrolysis process, which promotes the formation of polymeric aluminum except a few monomeric aluminum species.

PACl are produced by controlling the titration of aluminum salts (e.g., AlCl_3) with base and are characterized by the degree of neutralization ($\gamma = [\text{OH}^-/\text{Al}]$) or basicity ($((\gamma/3)\times 100\%)$). The value of γ vary from zero to three, corresponding to basicities of 0 to 100%. The basicity affects the alkalinity consumption of coagulant as well as the aluminum species distribution.

2.1.1 Chemistry of Hydrolyzing Aluminum

The chemical behavior of Al(III) in dilute solution affects the hydrolysis of aluminum that restricts the quality of coagulant in the process of coagulant production. In dilute solutions, the aluminum forms various monomeric and polymeric hydrolyzed aluminum species other than aluminum hydroxide precipitate ($\text{Al}(\text{OH})_3$). Studies have concluded that aluminum solubility can be described by the presence of monomeric and polymeric aluminum species in equilibrium with an amorphous $\text{Al}(\text{OH})_3$ solid phase (Baes and Mesmer, 1976; Benefield et al., 1982; Pouillot and Suty, 1992). The thermodynamic data for these species are summarized in **Table 2.1**. From this, the solubility of monomeric and polymeric species and an amorphous precipitate can be plotted as a function of pH. The solubility diagram for amorphous aluminum hydroxide ($\text{Al}(\text{OH})_{3(\text{am})}$) can be depicted as shown in **Fig. 2.1**. The hydrolyzed monomers include Al^{3+} , $[\text{Al}(\text{OH})]^{2+}$, $[\text{Al}(\text{OH})_2]^{+}$, and the familiar hydrolyzed polymer such as $[\text{Al}_2(\text{OH})_2]^{4+}$ as well as tridecamer ($[\text{Al}_{13}(\text{OH})_{24}]^{7+}$), in addition to $\text{Al}(\text{OH})_{3(\text{am})}$ or $\text{Al}(\text{OH})_{3(\text{s})}$ that occur near neutral pH. All of these polymeric aluminum species are formed by a series of bridging between hydroxyl of Al^{3+} caused by deprotonation of its bound water as pH rises, which is also called polymerization. For example, $[\text{Al}_2(\text{OH})_2]^{4+}$ formed through two deprotonated octahedral Al^{3+} bridges each other (Baes and Mesmer, 1976), as shown in **Fig. 2.2**.

Solubility of aluminum species is also influenced by the temperature of solution (Pernitsky and Edzwald, 2003), as well as the anions such as sulfate that can be incorporated into polymeric aluminum species to form visible precipitate (Wang et al., 2002). In fact, many aluminum species are metastable in hydrolysis process. Therefore, in-situ hydrolyzed aluminum species can further hydrolyze and vary with aging (Wang et al., 2004). It is very important to discover various unknown aluminum species to further understand the roles of various aluminum species on coagulation efficiency except these existent aluminum species proposed by theoretical calculation in the Al hydrolysis reactions.

Table 2.1 Summary of thermodynamic data for Al hydrolysis reactions (25 °C)

Products	Chemical Equation	pK	Ref.
Monomer	$\text{Al}^{3+} + \text{H}_2\text{O} \leftrightarrow \text{Al}(\text{OH})^{2+} + \text{H}^+$	5.0	(1)
	$\text{Al}^{3+} + 2\text{H}_2\text{O} \leftrightarrow \text{Al}(\text{OH})_2^+ + 2\text{H}^+$	9.39	(1)
	$\text{Al}^{3+} + 4\text{H}_2\text{O} \leftrightarrow \text{Al}(\text{OH})_4^- + 4\text{H}^+$	23.0	(1)
Polymer	$2\text{Al}^{3+} + 2\text{H}_2\text{O} \leftrightarrow \text{Al}_2(\text{OH})_2^{4+} + 2\text{H}^+$	6.27	(2)
	$6\text{Al}^{3+} + 15\text{H}_2\text{O} \leftrightarrow \text{Al}_6(\text{OH})_{15}^{3+} + 15\text{H}^+$	47.0	(2)
	$8\text{Al}^{3+} + 20\text{H}_2\text{O} \leftrightarrow \text{Al}_8(\text{OH})_{20}^{4+} + 20\text{H}^+$	68.7	(2)
	$13\text{Al}^{3+} + 28\text{H}_2\text{O} \leftrightarrow \text{Al}_{13}(\text{OH})_{24}^{7+} + 32\text{H}^+$	98.7	(3)
Precipitate	$\text{Al}(\text{OH})_{3(\text{am})} \leftrightarrow \text{Al}^{3+} + 3\text{OH}^-$	31.5	(3)
	$\text{Al}(\text{OH})_{3(\text{s})} \leftrightarrow \text{Al}^{3+} + 3\text{OH}^-$	33.5	(3)

Source: (1) Baes and Mesmer (1976)

(2) Benefield et al. (1982)

(3) Pouillot and Suty (1992)

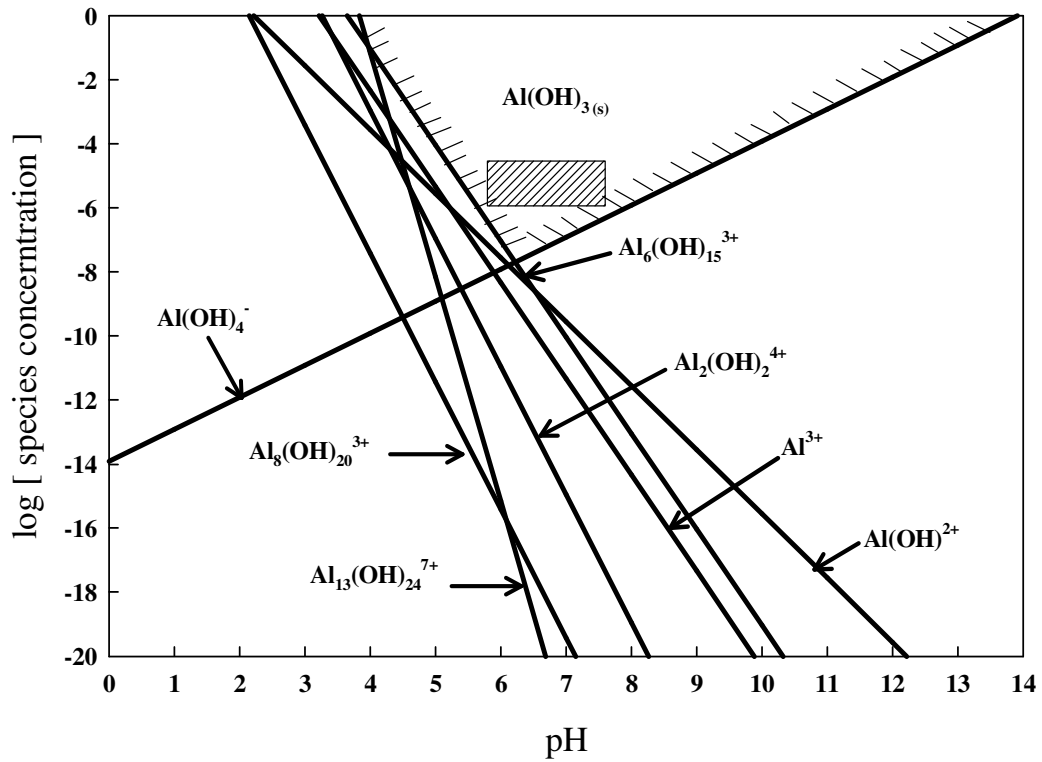


Fig. 2.1 Solubility of amorphous aluminum hydroxide.

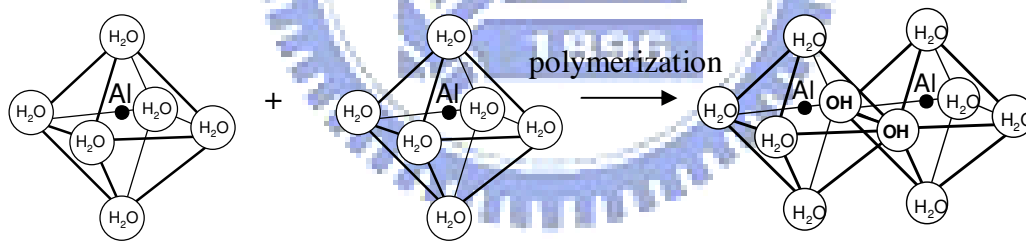


Fig. 2.2 Polymerization of $\text{Al}_2(\text{OH})_2^{4+}$. (Baes and Mesmer, 1976)

2.1.2 Identification of Hydrolyzing Aluminum Species

The identification of Al speciation is beneficial to further realize the reaction kinetics between particles and coagulants during coagulation. In the 1960s, various Al species have been proposed based on the theoretical physical chemistry, particularly polymeric aluminum species. However, the structures of these species were not further identified until the invention of nuclear magnetic resonance (NMR). Up to now, many researchers continue to identify new polymeric aluminum species (e.g., Al_{30}) or less prevalent polymers and to determine their formation mechanisms (Allouche et al., 2000; Chen et al., 2006; Rowsell et al., 2000). In most researches, Ferron colorimetric method and ^{27}Al -NMR method were adopted to identify the Al speciation of coagulants.

Since 1971, Ferron colorimetric method developed by Smith (1971) has been widely adopted to quantify different aluminum species. Smith identified three forms of aluminum in partially neutralized solutions that exhibit differential reaction kinetics with ferron agent (8-hydroxy-7-iodo-5-quinoline-sulfonic acid). He suggested that the aluminum reacting instantaneously with ferron is mononuclear, while intermediate polymeric aluminum species displays pseudo-first-order reaction kinetics with ferron, and that the aluminum fraction possessing an imperceptible reaction rate with ferron is composed of giant polymeric species or incipient solid phases. Recently, the researches have proposed a modified Ferron colorimetric method to avoid some unstable features (Wang et al., 2004). Based on the kinetic difference of the reactions between the aluminum and Ferron agent, the hydrolyzed aluminum species can be divided into monomeric (Al_a), polymeric (Al_b), and colloidal (Al_c), respectively. However, the structure of various aluminum species can not be clearly identified only by Ferron colorimetric method. Thus, there are still many debates on

the structure of these aluminum species determined by this method, especially polymeric aluminum species.

Direct ^{27}Al -NMR investigations have cast doubt on such indirect method since ^{27}Al -NMR spectroscopy has provided direct evidence for the existence of a number of polymeric species in a wide range of hydrolyzed Al solution (Bottero et al., 1980; Bertsch et al., 1986a; Akitt and Elders, 1988). The ^{27}Al -NMR can assist investigators in determining the coordination characteristics of the Al atoms contained in various polymers. By using ^{27}Al -NMR method, many investigations have definitively proved that the Al_{13} polycations ($[\text{Al}_{13}\text{O}_4(\text{OH})_{24}]^{7+}$) present generally in hydrolyzed Al solutions prepared from Al metal over various Al concentrations (from 10^{-5} to > 2 mol/L) by titration with bases (Bottero et al., 1987; Bertsch, 1987; Parker and Bertsch, 1992). In addition, the monomeric Al species, oligomer, and other polymeric Al species also can be identified by ^{27}Al -NMR method (Akitt and Farthing, 1981; Akitt, 1989).

However, there are many arguments on the correlation between the quantities of various species determined by Ferron and ^{27}Al -NMR methods. Many researches have indicated that the quantity of Al_{13} determined by ^{27}Al -NMR method can be roughly represented by that of Al_b measured by Ferron colorimetric method (Liu et al., 1999; Shi et al., 2007). On the contrary, it is the case that the imperfect agreement still remains between the results of Ferron and ^{27}Al -NMR methods, including the possibility that some implementation of Ferron method may overestimate monomeric Al fraction as well as polymeric species (Bertsch et al., 1986b). As a result, the comparison between the results of Ferron colorimetric method and ^{27}Al -NMR method must be conducted for each research that needs the identification of Al species.

2.1.3 Synthesis and Characteristics of Al₁₃

Tridecamer (i.e., Al₁₃) is the major polymeric species of the PACl. The production of Al₁₃ and its stability mainly depend on the synthesis parameters during hydrolysis process. In addition, the transformation of Al₁₃ principally varies with pH or time. The synthesis, structure and transformation of Al₁₃ are described as follows:

(1) Synthesis of Al₁₃

The quantity of Al₁₃ formed in hydrolysis process is controlled by many parameters, including basicity, total Al concentration (Al_T), temperature, the addition rate of base and mixing intensity. Parker and Bertsch (1992) have reported that polymeric fraction decreases with decreasing Al_T when Al_T is in the range from 5 × 10⁻³ M to 1 × 10⁻⁴ M. By contrast, the formation of Al₁₃ is not affected by Al concentration for Al_T between 10⁻¹ M and 10⁻³ M (Parthasarathy and Buffle, 1985). However, the Al₁₃ formed with the initial lower Al_T was not stable due to higher pH of solution after preparation. For γ ([OH⁻]/[Al])= 2.4, Al₁₃ is relatively insensitive to temperature below 85 °C, while the Al₁₃ transforms into Al₁₃ aggregates as the temperature is over 85 °C (Klopprogge et al., 1992). In general, the maximum fraction of Al₁₃ only can be produced when the value of γ is controlled between 2.2 and 2.4. Otherwise, the amount of Al₁₃ formed during titration is increased as a function of base injection rate and reaches a maximum at higher base addition rate (Bertsch, 1987). The slower base addition rate leads to the formation of stable Al₁₃, and the pH of solution decreases with aging (Parthasarathy and Buffle, 1985). On the other hand, mixing intensity could affect Al₁₃ production, stability and precipitation during PACl preparation. Poorer mixing is required for the formation of Al₁₃ during the preparation of PACl (Clark and Flora, 1991). Less intense mixing provides an interfacial disequilibrium for a long time that allows the favorable

chemical conditions for Al_{13} production to exist longer during base titration. On the contrary, other studies have indicated that the more mixing intensity results in higher content of Al_{13} after titration (Bertsch, 1987; Kloprogge et al., 1992). Because mixing efficiency depends on the mixing type and mixing energy, it is difficult to conclude that the more or less intense mixing is favorable for the Al_{13} production during base titration.

(2) Structure of Al_{13}

The Al_{13} molecule, $[\text{AlO}_4\text{Al}_{12}(\text{OH})_{24}(\text{H}_2\text{O})_{12}]^{7+}$, which is composed of a $\text{Al}(\text{O})_4$ tetrahedron surrounded by 12 octahedrally coordinated $\text{Al}(\text{O})_6$ sharing edges (Johansson, 1960) shown as **Fig. 2.3** in which $\mu_2\text{-OH}$ is a hydroxyl ligand bridging two Al atoms; $\mu_4\text{-O}\mu$ is an oxo ligand bridging four Al atoms; $\eta^1\text{-H}_2\text{O}$ is a bound and nonbridging water molecule. This kind of Al_{13} configuration has been commonly referred to as “Keggin” structure. The size of Al_{13} as determined by small angle X-ray scattering is approximately 1.2 nm (Bottero et al., 1982). However, there are many arguments about the formation mechanisms of Al_{13} in aqueous solution. One “inhomogeneous model” has been proposed that Al_{13} is generated at localized high basic strength region during base addition that allows $\text{Al}(\text{III})$ to become four-fold coordination, e.g., $\text{Al}(\text{OH})^4$, which is considered to be essential precursor for Al_{13} formation (Bertsch, 1987; Kloprogge et al., 1992).

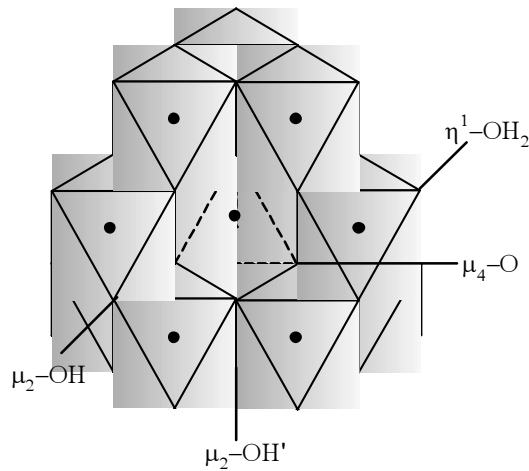
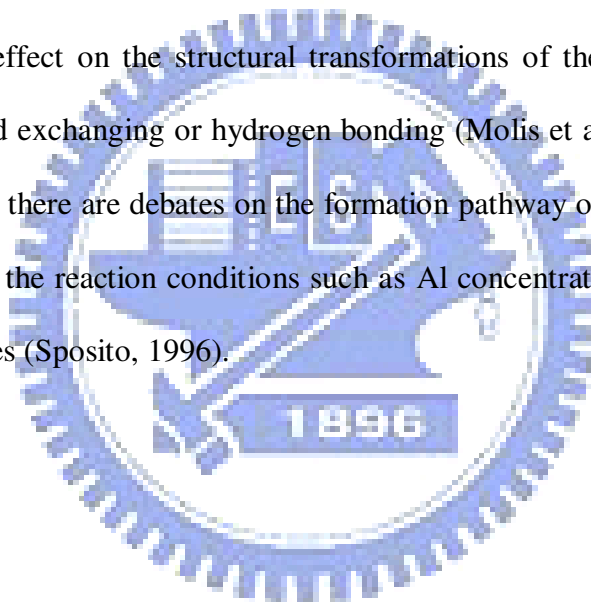


Fig. 2.3 The ϵ -Keggin structure of Al_{13} polycation. (Johansson, 1960)

(3) Transformation of Al_{13}

Al_{13} is metastable with respect to aluminium hydroxide ($\text{Al}(\text{OH})_3$), which transforms over time to crystalline $\text{Al}(\text{OH})_3$ such as gibbsite [α - $\text{Al}(\text{OH})_3$] or bayerite [γ - $\text{Al}(\text{OH})_3$] in the hydrolysis processes (Violante and Huang, 1985; Bradley et al., 1993). Because different oxygen sites of Al_{13} have different water exchange rates which relate to decomposition of Al_{13} (Phillips et al., 2000), the transformation Al_{13} occur when pH changes. Al_{13} favors aggregation when pH is over 6 (Furrer et al., 1992), and the size of Al_{13} aggregates increase gradually from 570 nm at pH 4.35 to 1200 nm at round pH 6.5 (Dubbin and Sposito, 2005). Moreover, the condensation of Al_{13} could form at a specific pH due to shear-induced mixing (Furrer et al., 2002). On the contrary, Al_{13} aggregates are easily decomposed by H^+ as the pH value decreases (Furrer et al., 1999). The Al_{13} deprotonation varies with the concentration of Al_{13} in addition to the pH of solution. During condensation, Al_{13} can transform into various Al_{13} aggregates with increasing $[\text{OH}]/[\text{Al}]$ ratio and total Al concentration (Bottero et al., 1987). The aggregation of Al_{13} often occurs at higher total Al concentrations. In concentrated Al solution ($>0.1 \cdot 10^{-3}$ mol/L) synthesized

or aged at a given temperature, other larger polymeric Al species that are categorized as "Al₁₃-like" polycations have been proposed and suggested (Akitt and Farthing, 1981; Fu et al., 1991). With aging, the Al₁₃ structure is gradually lost and that they eventually take on the crystalline structure of gibbsite (Bottero et al., 1987; Bradley et al., 1993). Other study has suggested that the in-situ formed Al₁₃ (i.e., metastable Al₁₃) during hydrolysis do not condense with aging, but undergo direct structural rearrangement and then transforms into small polymers of the gibbsite fragment configuration, and may nucleate and commence the process of gibbsite crystallite growth (Hsu, 1988). On the other hand, organic matters and inorganic anion also have a profound effect on the structural transformations of the aggregated Al₁₃ by complexing, ligand exchanging or hydrogen bonding (Molis et al., 1996; Wang et al., 2002). However, there are debates on the formation pathway of the Al₁₃ aggregates, which depends on the reaction conditions such as Al concentration, pH, temperature, and aging processes (Sposito, 1996).



2.2 Alum Coagulation

Coagulation reaction with aluminum coagulants involves three continuous sequential steps which can form various flocs at different conditions such as pH, dosage, mixing intensity and temperature. Schematic illustration of coagulation process is shown in **Fig. 2.4**. (a) Addition and activation of the coagulant through a series of hydrolysis reactions in water and form active coagulant species. (b) Reactions of the active coagulant species with the stabilized colloidal particles to destabilize them through "rapid-mixing". The primary function of the rapid-mixing is to disperse the coagulants uniformly in a short period of time in order to efficiently destabilize colloidal particles. (c) Aggregations of the destabilized colloidal particles and collide to form microflocs. Through "slow-mixing", namely flocculation, these microflocs can form readily settleable or filterable flocs that can be removed by the subsequent sedimentation and filtration. In this section, the researches with respect to colloidal interaction forces, coagulation mechanisms and removal of colloidal particles will be reviewed.

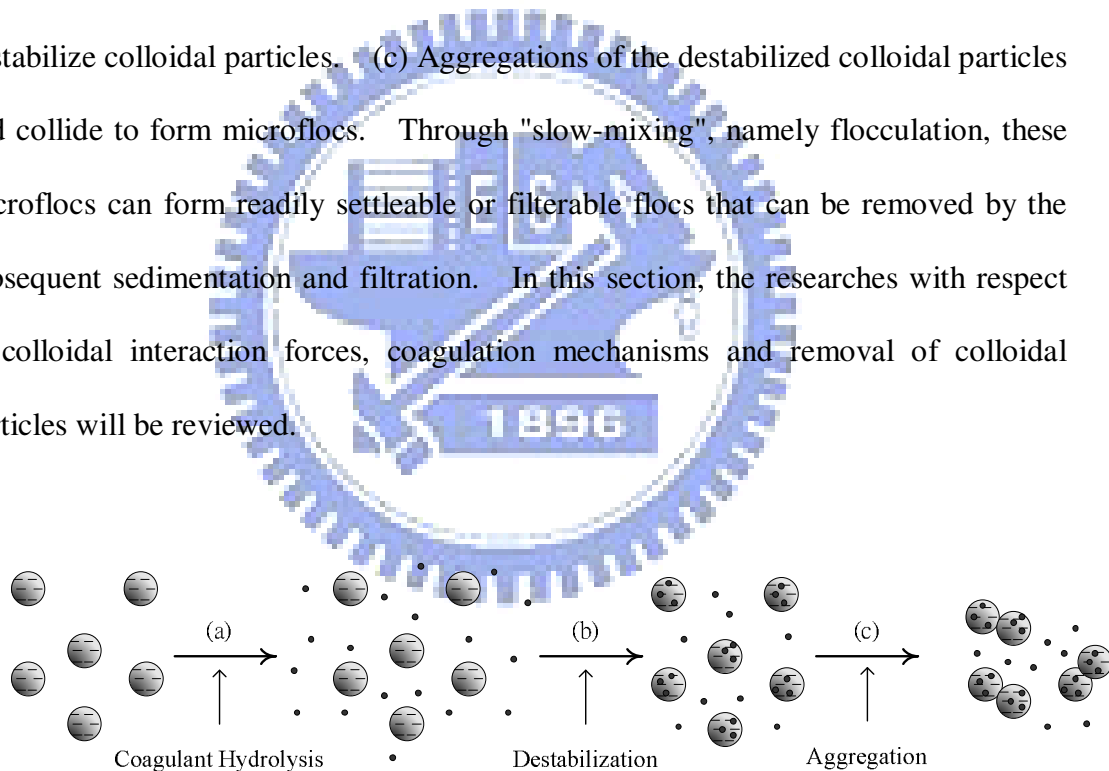


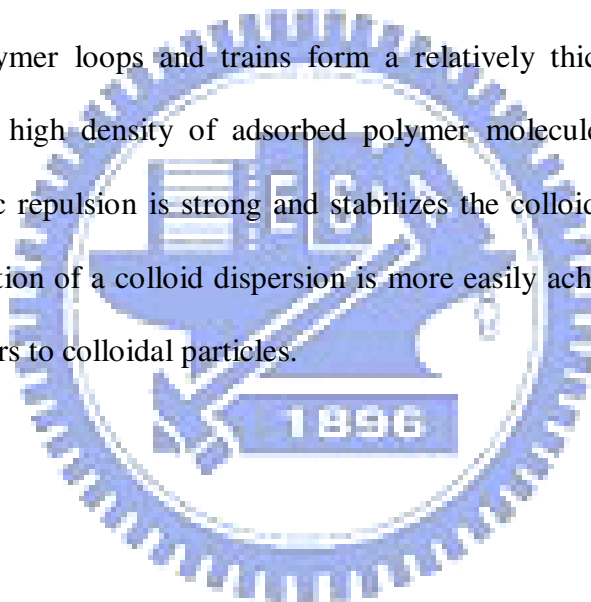
Fig. 2.4 Schematic diagram of coagulation process: (a) coagulant hydrolysis (b) destabilization of colloidal particles, and (c) aggregation of destabilized colloidal particles.

2.2.1 Colloidal Interaction Forces

Interaction forces between colloidal particles affect significantly the stability of colloidal particles and their aggregation when colloidal particles approach each other. The interparticle forces can be appropriately explained by the Derjaguin-Landau-Verwey-Overbeek (DLVO) theory (Derjaguin and Landau, 1941; Verwey and Overbeek, 1948). For DLVO theory, the magnitudes of the component and total interaction potentials at various distance of separation for two spheres with equal size are depicted in **Fig. 2.5**. In this theory, the van der Waals electrostatic forces were mainly considered, as indicated in **Fig. 2.5 (a)**. When the potential energy turns into more and more attractive as colloids approach one another, colloids can be aggregated in the primary minimum of the potential energy, as illustrated in **Fig. 2.5 (b)**. **Fig. 2.5 (c)** shows the second-minimum in the potential energy curve in which the potential energy becomes more and more attractive as colloids approach closer; however, the energy barrier arises after a certain separation distance. The aggregation of colloids also occurs by the long-range attraction under a long separation distance when the energy at second-minimum sink is favored, which can lead to the formation of fairly weak aggregates. By contrast, there is no aggregation between colloids and the colloids are stable when the potential energy keeps repulsive, as seen in **Fig. 2.5 (d)**. In addition, non-DLVO forces, including hydrophobic attraction and steric repulsion, are also the considered component in the colloids interaction process. These interaction forces are important for the understanding of the properties of various colloid dispersions of practical interest.

When a surface has no polar or ionic groups or hydrogen-bonding sites, there is no affinity for water and the surface is said to be hydrophobic (Elimelech et al., 1995). A hydrophobic surface is inert to water and can not bind water molecules by hydrogen

or ionic bonds (Israelachvili, 1991). The presence of a hydrophobic surface can restrict the natural structuring tendency of water, imposing a barrier which prevents the growth of clusters in a given direction. Water confined in a gap between two hydrophobic surfaces is unable to form clusters and result in an increased free energy of the water relative to bulk water. As a result, an attraction between hydrophobic surfaces shows up as a consequence of water molecules migrating from the gap to the bulk water. Such an attraction could be quite long range and play a major role in promoting flocculation. Steric repulsion often appears when two adsorbed layers of polymeric chain molecules overlap, where particle surface is saturated with polymer such that the polymer loops and trains form a relatively thick layer of adsorbed polymers. For a high density of adsorbed polymer molecules on the surface of particles, the steric repulsion is strong and stabilizes the colloid dispersions. Thus, the steric stabilization of a colloid dispersion is more easily achieved by attaching of long chain polymers to colloidal particles.



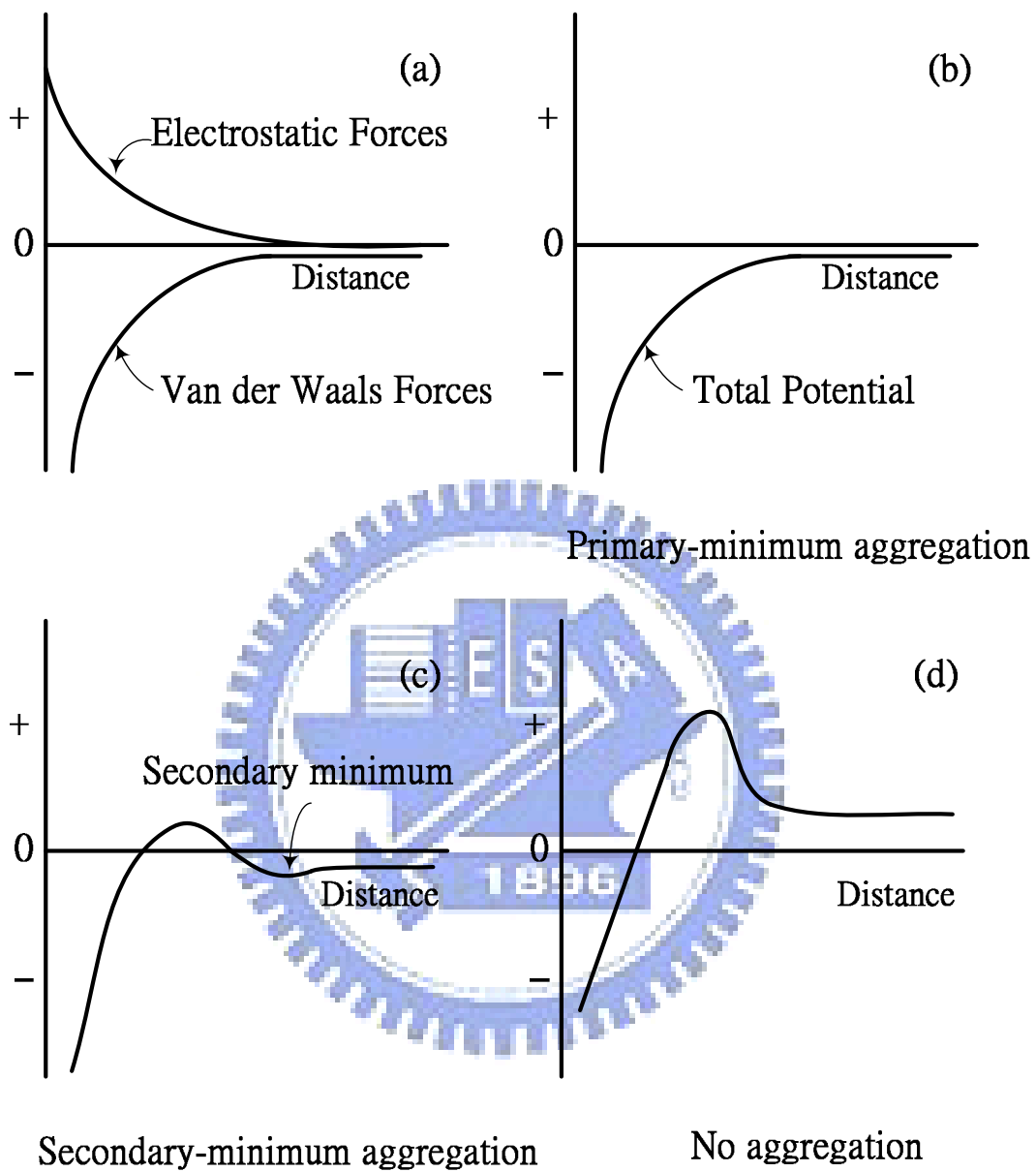


Fig. 2.5 Potential energy versus distance profiles of DLVO interactions. (a) van der Waals and electrostatic forces (b) primary-minimum of the potential energy (c) secondary-minimum of the potential energy and (d) potential energy of a stable suspended particles.

2.2.2 Mechanisms of Coagulation

The mechanisms of coagulation vary with the type of coagulants and the operational parameters. The destabilization of inorganic colloidal particles is dictated by principal mechanisms that substantially affect coagulation dynamics and the properties of flocs such as size, structure and strength. Destabilization of inorganic colloidal particles will be discussed in this section as follows:

(1) Electrical Double-Layer (EDL) Compression

Particles in liquid system in which ions are present are usually charged due to adsorption, ionization, hydration, or isomorphic replacement on the surfaces. These surface charges create an electrostatic field that causes a counter charge, and thus covers the electric surface charge. Some of the counter-ions might specifically adsorb near the surface and build an inner sub-layer, or so-called Stern layer; the outer part of the screening layer is called the diffuse layer (Lyklema, 1995). The electric potential has a maximum value at the particle surface and decreases with distance from the surface. The electric potential surrounding the particle is so-called zeta potential which is located in the diffuse layer. The electrical double layer is related to electrostatic interactions between particles, including surface potential and the electrical double layer thickness. Surface potentials can be influenced by the ionic strength and adsorbed counterions in the system. The electrical double layer thickness is formed by the surface charge of particles and the associated counter-ions charge. According to the DLVO theory, higher ionic strength can cause higher counter-ions concentration in the diffuse layer, which compresses the thickness of the diffused electrical double layer, lowering the surface potential and the energy barrier. Therefore, Al^{3+} is more efficient than Ca^{2+} or Na^{+} in the electrical double layer compression. The interaction between particles can be evaluated in terms of

potential energy. The overall interaction is unfavorable (repulsive) if the potential energy is positive. If the potential energy is negative, the net effect is attractive. Thus, the proper ionic strength in coagulation process is necessary to reduce the net potential energy for particle aggregation.

(2) Adsorption-Charge Neutralization

Inorganic particles such as alumino-silicates (clays) and silica particles are generally electrically charged due to the isomorphic substitution of ions in the bulk solid phase, or to the reactions of surface functional groups with dissolved ions in the aqueous phase (Sposito, 1993). The major inorganic colloids are generally negatively charged in water due to their low zero point of charge (Lerman, 1979). The positively charged Al(III) hydrolysis products such as Al_{13}^{7+} polycation can specifically be adsorbed on the surface of colloids, which can modify the original charge on the surface of colloids. These interactions can neutralize the surface charge of the colloids and then facilitate destabilization of the colloids, which are referred to as adsorption-charge neutralization. In addition, it has been proposed that the colloids can be coated with $Al(OH)_3$ precipitates and then the destabilization of the colloids occurs by adsorption-charge neutralization since a local precipitation of positively charged $Al(OH)_3$ on the colloids surface (Letterman et al., 1982). Dentel (1988) also has proposed that different kinds of coagulants cause different coagulation mechanisms with precipitation charge neutralization (PCN) to explain that charge neutralization can be achieved by partial coverage of positively charged hydroxide on negatively charged particle surface. The adsorption-charge neutralization mechanism is characterized by stoichiometry between the coagulant and the concentration of colloids. Destabilization by charge neutralization generally occurs

at low concentrations of polymer where the repulsive electrostatic forces between the particles (Gregory, 1987). Overdosing of the coagulant can eventually reverse the surface charge on colloids, and a subsequent charge reversal of colloids surface and the restabilization of colloids possibly occur. Gregory (1996) has also demonstrated that some regional charge heterogeneity can occur that leads to the arrangement of the polymers in patches on the particle surface, which is referred to as electrostatic patch, as illustrated in **Fig. 2.6**. This mechanism is generally observed when particles having a low charge are neutralized by the polymers with high charge densities. Electrostatic patch also could be caused by aluminum hydroxide precipitate for PACl coagulation in the presence of anion (Wang et al., 2002). Likewise, other study has suggested that the PACl containing high Al_{13} contents can bring electrostatic patch coagulation at alkaline pH to destabilize kaolin particles when Al_{13} aggregates forms (Ye et al., 2007).

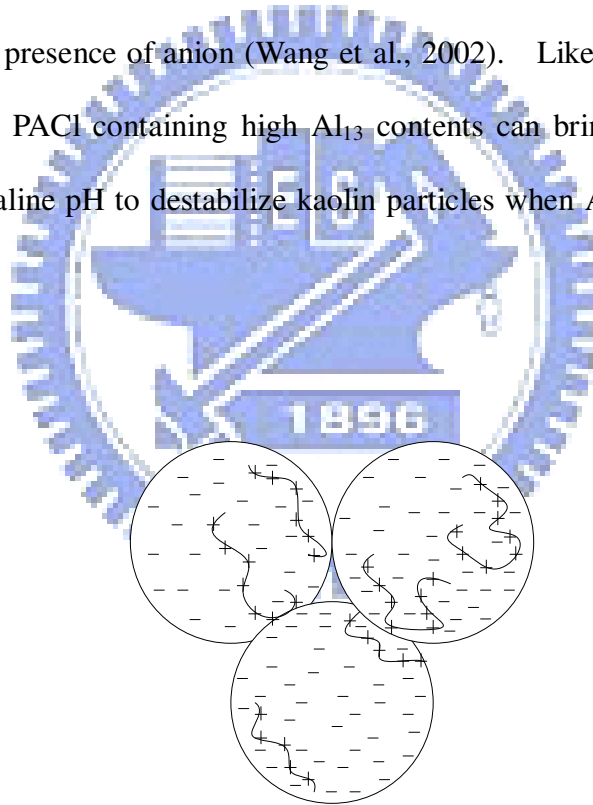


Fig. 2.6 Electrostatic patch model of the interaction between negatively charged particles and adsorbed cationic polymers. Redrawn from Gregory (1987)

(3) Enmeshment (Sweep flocculation)

Metal ions of high charge valence, e.g., Al^{3+} , hydrolyze to form insoluble metal hydroxide precipitates after the addition of large amounts of aluminum or iron salts. The initial aluminum hydroxide precipitates are amorphous. Over time, the solid is converted into a more stable crystalline phase. $\alpha\text{-Al(OH)}_3$ and $\gamma\text{-Al(OH)}_3$ are two ordinary forms. Enmeshment, or sweep flocculation, refers to physical mechanism where the colloids are entrapped in the aluminum hydroxide precipitates and the fine colloidal particles are swept together by sedimentation. The enmeshment is slower than other coagulation mechanisms because the $\text{Al(OH)}_{3(s)}$ require a few seconds to form (Letterman et al., 1973). Coagulation of alum salts undergoes enmeshment mostly at around neutral pH where the particle can be then aggregated as sweep flocs by both surface precipitation and adsorption of amorphous hydroxide precipitate on the surface of particles (Chowdhury and Amy, 1991). Optimal sweep flocculation is identified in the pH range of 6 to 8 or higher depending on alum dosage. When pH value is less than the isoelectric point of $\text{Al(OH)}_{3(am)}$ (pH 8) and the alum concentration is less than the dosage for sweep flocculation, the combination of sweep and adsorption occurs and the smaller positively charged aluminum hydroxide precipitates are adsorbed onto the larger negatively charged particles, which is called heterocoagulation (Amirtharajah and Mills, 1982). However, enmeshment or sweep flocculation also could occur for PACl coagulation of water when the PACl containing a considerable monomeric species that can hydrolyze into aluminum hydroxide precipitates. In enmeshment, the solid precipitates also increase the contact with colloidal particles and speed up the flocculation kinetics. This process is useful to remove particles from low turbidity water.

(4) Interparticle Bridging

Because of the strong adsorption of polymer toward colloidal particles, interparticle bridging occurs when the loops and tails of a polymer adsorbed to one colloidal particle attaches to one or more other colloidal particles. These processes are dictated by polymers which attach to several points of the colloidal surface and are large enough to extend free segments (i.e., loops and tails) excess the zone of electrostatic double layers so that they are capable of binding to each other (Gregory, 1987). The surface coverage of adsorbed polymer plays a major role in controlling the probability of bridging. Flocculation can occur as polymers are at equilibrium with the surface of colloidal particles (Pelssers et al. 1989), while non-equilibrium flocculation occurs before the polymers are able to completely collapse on the colloidal surface (Gregory, 1988).

The dosage of polymers also affects the conformation and coverage surface of the polymer on colloidal surface, which can influence the probability of occurring bridging flocculation (Zhou and Franks, 2006). Moreover, the time that polymers remain before equilibrium is predominant over flocculation. The time required to adsorb the polymers on the colloidal surface will be influenced by the particle/polymer ratio, the size of the particle, the surface area of the particle, the adsorption energy of the polymer segments and the collision frequency among the particles (Gregory, 1988; Biggs et al., 2000), which substantially affects the flocculation efficiency. For charged polymers, the ionic strength plays an important part in bridging flocculation. With increasing the ionic strength, the polymer is deformed, decreasing the rigidity of polymer, resulting in worsened flocculation. However, the high ionic strength will also reduce the interparticle repulsion, allowing particles easily approach to each other. Therefore, optimal interparticle bridging

induced by polymers generally occurs at intermediate charge densities or salt concentrations (Matsumoto and Adachi, 1998).

On the other hand, study has advocated that the PACl containing large amounts of Al_{13} or giant polymeric aluminum species (Al_{30}) may cause interparticle bridging flocculation at high pH because both Al_{13} and Al_{30} can further hydrolyze and restructure rapidly to form huger polymers when pH rises (Chen et al., 2006). However, it is difficult to directly verify the occurrence of interparticle bridging induced by Al_{13} or Al_{30} aggregates.



2.3 Coagulation Dynamics

During coagulation, the destabilized particles collide with each other to form clusters and continue to grow as flocs when they encounter other particles or clusters. For efficient coagulation, it is important to understand the process of particles movement during aggregation (i.e., dynamics of particles aggregation). Since particles aggregation is a kinetic and non-equilibrium growth process, the formation of clusters or flocs is through random collisions, and the structure of flocs is inherently related to the dynamics of aggregation, which in turn, is reflected by the time evolution of the cluster mass distribution. On the other hand, the breakage of flocs can be induced by a given shear force and the breakage behavior is affected by ambient physical and chemical conditions (Clark and Flora, 1991; Oles, 1992; Gregory and Dupont, 2001). As flocs grow larger, they increasingly become porous due to random collisions and collision efficiency comes lower (Brakalov, 1987). Once aggregate approach the length scales of turbulent eddies, hydrodynamic stress induced by mixing can fragment fragile flocs. However, the flocs strength is directly related to flocs structure and the inter-particle bonds between the components of flocs (Bache et al., 1997). Fractal dimension, which represents the scale-invariant branched structure formed as symmetric dilation (Mandelbrot, 1982), can be utilized to quantify the structure of flocs in coagulation process (Aubert and Cannell, 1986; Meakin, 1988; Lin et al., 1989). Intrinsically, the flocs with a fractal structure will form when the equilibrium between aggregation and breakage of flocs approach, which determines their strength during shearing. In this section, the studies about the dynamics of aggregation, the breakage of flocs and restructuring will be extensively reviewed.

2.3.1 Flocculation Formation

Witten and Sander (1981) have introduced the growth of flocs is dictated entirely by diffusion controlled aggregation model (i.e., diffusion-limited aggregation, DLA) in particle aggregation. In DLA, there is no repulsion between colloidal particles, so that particles attach permanently to other particles at the first contact and then grow to clusters or flocs via rapid random-walk trajectories (i.e., ‘rapid’ perikinetic aggregation) originating from outside of region occupied by the cluster. In this model, the sticking probability is equal to one and every collision between particles is effective. The fractal structures of flocs formed in this way are random ramified and insensitive to the sticking probability. Another model is the reaction-limited aggregation (RLA), for which a considerable number of collision (i.e., ‘slow’ orthokinetic aggregation) are needed between particles before sticking (Meakin and Witten, 1983). Obviously, in this model the sticking probability is small than one and only a small fraction of particles collisions lead to a permanent contact. This process produces more compact clusters or flocs whose density is irrelevant to distance. During coagulation, DLA and RLA will dominate over the fractal growth of particles, which results in different flocs structure (Elimelech et al., 1995). RLA produces a much narrower aggregate size distribution than DLA (Kostansek, 2004).

For difference in size and structure of flocs, particle-cluster and cluster-cluster aggregation provide a good explanation, illustrated in **Fig. 2.7**. In particle-cluster aggregation, a particle is able to penetrate into a cluster before encountering another particle and sticking, which leads to a more compact structure, as seen in **Fig. 2.7 (a)**. As shown in **Fig. 2.7 (b)**, two clusters could collide and then stick at the first contact before the clusters have interpenetrated to a significant extent, resulting in much more open structure. Torres et al. (1991) have found that flocs formed by cluster-cluster

aggregation are very similar to those formed by DLA. At RLA, particles need to collide many times before sticking occurs due to low collision efficiency, which increases opportunities for particle interpenetration. For this reason, flocs formed by RLA are more compact than those formed by DLA (Lin et al., 1989).

Moreover, flocs structure may change during coagulation, which gives more compact forms. Aubert and Cnnell (1986) have found that silica particle aggregation induced by DLA initially gives loose flocs with low fractal dimension, but denser flocs with higher fractal dimension are observed after a period of time. It is likely that shear induced by mixing can cause some deformation and rearrangement of flocs, leading to some compact flocs. On the other hand, it has been generally acknowledged that the turbulent energy dissipation with increasing floc size as a result of increasing porosity (Tambo and Watanabe, 1979; Kusters, 1991), and the porosity within the flocs could be depicted by use of fractal concepts in shearing (Sonntag and Russell, 1986).

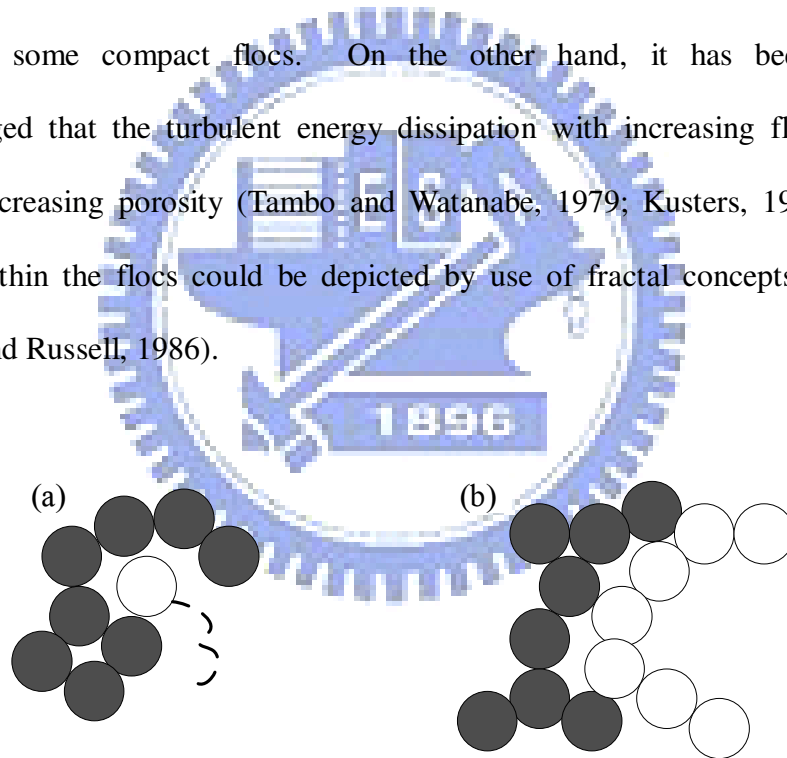


Fig. 2.7 Fractal flocs formed by (a) particle-cluster aggregation (b) cluster-cluster aggregation.

2.3.2 Floc Breakage and Restructuring

Because of the inherent complexity, fragility of flocs and variation in floc size, shape and composition, the breakage behavior of flocs is not easily identified. It has been generally accepted that two model of flocs rupture induced by shear stress, including splitting and erosion (Francois, 1987; Mikkelsen and Keiding, 2002). These stresses have been manifested as splitting (i.e., large-scale fragmentation) and surface erosion, as demonstrated in **Fig. 2.8**.

Splitting is due to the instantaneous velocity differences across the body of the flocs, which produce several flocs fragments of a size similar to the parent flocs (Thomas, 1965). In addition, since fluid drag forces can strip primary particles or small clusters from the surface of flocs, called surface erosion, leading to an increase in the small particle size ranges. Glasgow and Luecke (1980) have observed experimentally that splitting is the dominant mechanism for flocs fragmentation. However, Williams et al. (1992) have suggested that more compact flocs structures were more likely to suffer surface erosion, while more open flocs would fracture by splitting. On the other hand, Potanin (1993) has modeled the shear-induced fragmentation of fractal flocs and advocated a combination of soft and rigid characteristics of actual flocs. From it, two or more fragments with mean daughter floc size are observed. These fragments are denser than parent flocs and there is no direct relationship between parent and daughter structure.

During coagulation, irregular flocs with a fractal structure suffered any shearing is probably to produce packed structure when particle-particle links shift to location with higher effective coordination numbers. This can not only occur in fragmentation, but also a change in fractal structure can often happen in the period of coagulation. Jiang and Logan (1996) have proposed that the fractal dimension of

flocs can increase with increasing floc size in coagulation. In other case, however, the fractal dimension of flocs can decrease over time in the initial stages of flocs formation for alum coagulation of latex microspheres (Chakraborti et al., 2003). The discrepancy can be attributed to restructuring of flocs that is the most prevalent compaction mechanism as a steady state is approached between aggregation and fragmentation during coagulation (Spicer and Pratsinis, 1996).

(a) Splitting

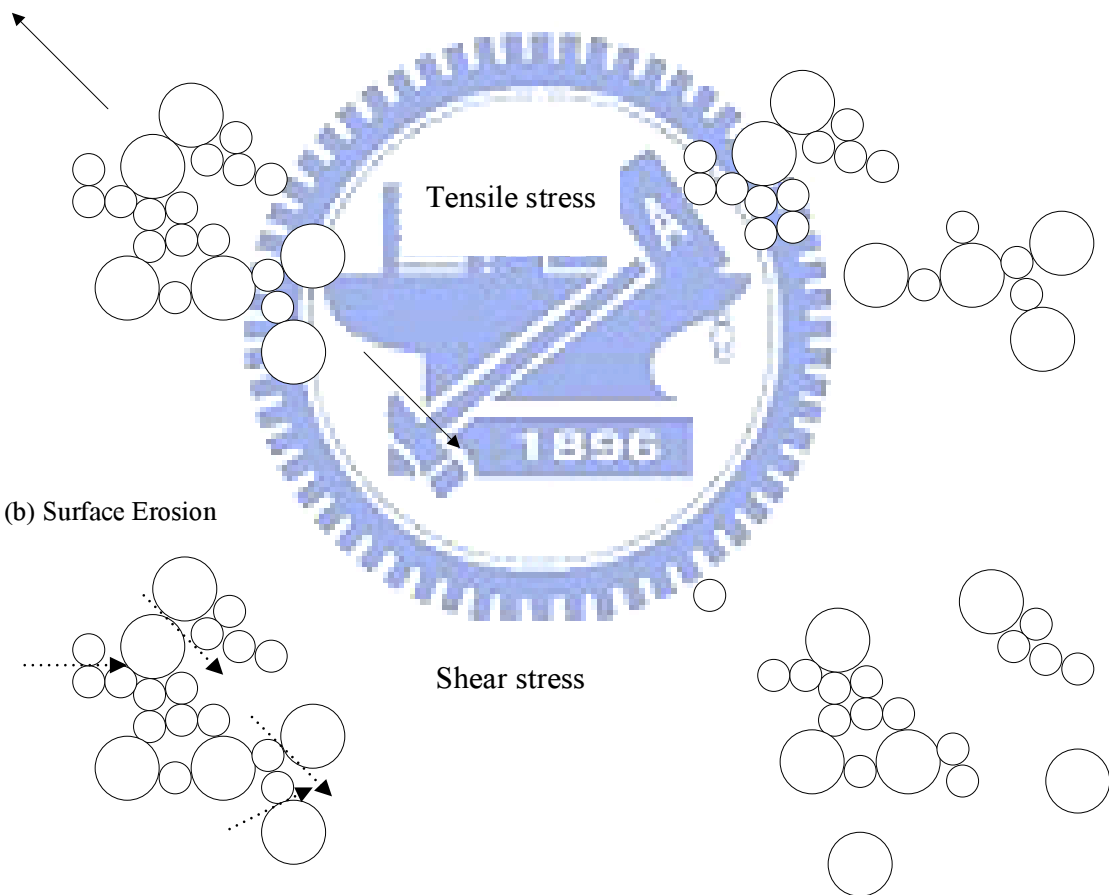


Fig. 2.8 Two proposed mechanisms for the breakage of aggregates at different shear conditions: (a) Splitting (b) Surface Erosion. Redrawn from Jarvis et al. (2005)

2.4 Floc Physical Characteristics

When particles aggregate, the resulting flocs may be formed through several different ways and thus numerous floc size and structures are possibly created. In real aggregation, either hundreds or thousands of primary particles can contact and thus bonds to form irregular fractal flocs. Thus, it is a formidable task to realize the detailed characteristics of them. In the past, many researchers have used optical analyzer to determine the characteristics of flocs such as size, shapes and fractal dimension. However, these characteristics of flocs are varied with the source of particles, the type of coagulants and agitation conditions applied in coagulation.

It has been recognized that the floc physical characteristics affect particle removal by sedimentation and filtration (Gregory, 1997; McCurdy et al., 2004). Characteristics of flocs are closely related to coagulation process where the aggregation and break-up is very important. The equilibrium between aggregation and break-up significantly affect the eventual flocs structure that determines the size, fractal dimension and strength of flocs.

In summary, the flocs physical characteristics are relevant to coagulation and consequent process in water treatment. In this section, a detailed description is given for flocs nature such as particles size, fractal dimension and strength.

2.4.1 Floc Size

In general, the size of a spherical regular and homogenous particle can be defined simply by its diameter. All most particles in water treatment, however, are irregular and heterogeneous. For irregular particles such as flocs, size is usually designated as a characteristic diameter or an equivalent diameter. On the whole, flocs are measured by image analysis method such as microscopic or microphotographic manner that can only capture two-dimensional patterns of the three-dimensional particle and calculate various particle sizes and shape parameters from two-dimensional images, in which the two-dimensional characteristic diameter or equivalent diameter is commonly called “projected diameter”. Among these projected diameters, projected area diameter, perimeter diameter, Feret’s diameter that is the maximum distance from edge to edge, Martin’s diameter that is the length of line that cuts the particle into two equal parts, are useful for characterizing floc size.

One of the principal projected area diameters calculated is circle equivalent diameter which is the diameter of a circle with the same area as the two-dimensional image of particle. Different shaped particles will have an influence on this circle equivalent diameter. However, it is only a single number that either gets larger or smaller as the irregular particle is imaged, and it is not suitable to measure the multi-scale particles distribution system, e.g., natural water, as the single value depends upon which individual particle is chosen. Hence, a more appropriate single characteristic number such as mean or median would be preferable to be the characteristic diameter in a normal size distribution system. In most case, use of the mass median equivalent diameter, d_{50} , is common practice. The d_{50} is the particle size that divides the frequency distribution in half.

2.4.2 Fractal Dimension

Flocs or aggregates have been recognized as fractal objects (Mandelbrot, 1982; Meakin, 1988). For a large number of flocs, the mass of flocs scales with their characteristic size (e.g., diameter). The relationship between flocs mass, M , and size, l , is:

$$M \propto l^{D_f} \quad (\text{Eq. 2.1})$$

Essentially, the structure of fractal flocs is characterized by the magnitude of its fractal dimension, D_f . Fractal flocs have a self-similar structure (Sonntag and Russell, 1986), which is scale-invariant and independent of the type of particles (e.g., clay, latex or gold). Various geometrical properties and methods have been presented in detail via arithmetic simulation (Jiang and Logan, 1991). These researchers concluded that fractal dimensions relate floc size to some property in n -dimensions, where n can be equal to 1, 2, or 3. In practice, fractal dimensions of flocs imbedded in two-dimensional and three-dimensions are:

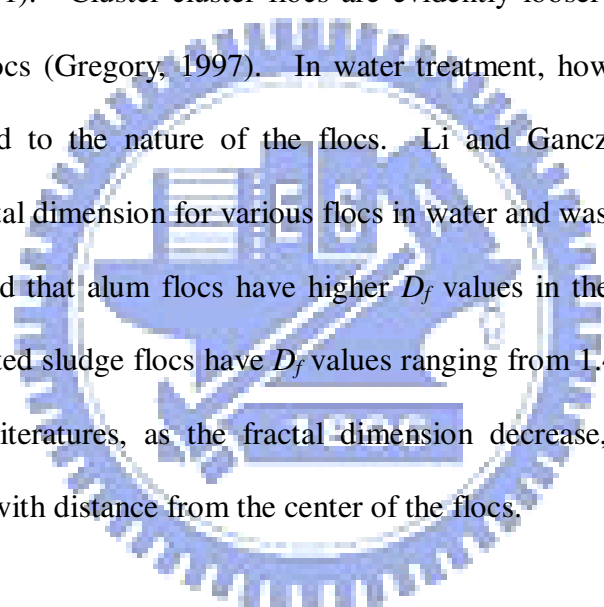
$$A \propto l^{D_2} \quad (\text{Eq. 2.2})$$

$$N_p \propto l^{D_3} \quad (\text{Eq. 2.3})$$

where l is the maximum floc size, A is the projected flocs area, and N_p is the number of particles in flocs. The higher the fractal dimension, the more compact is the flocs structure. Fractal dimension varies between 1, representing a linear floc, and 3, representing a solid floc. For Euclidean objects, D_f is usually an integer (Waite, 1999), but the values of D_f are non-Euclidean dimensionality for fractal objects. Two-dimensional fractal dimensions of flocs are well correlated with their three-dimensional fractal dimensions when primary particles are inorganic colloids (Lee and Kramer, 2004).

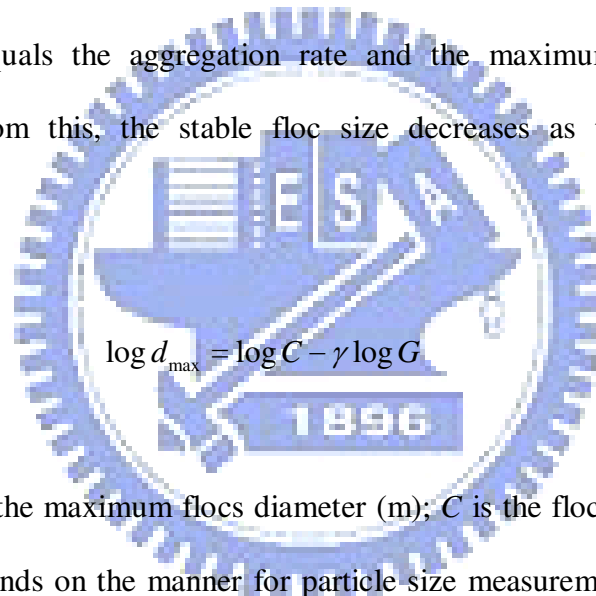
Fractal theories provide an original method to describe the structure of particulate

aggregates or flocs (Lee et al., 2002). Computer simulation of DLA as reported by Meakin (1988), with single-particle addition, gives fairly dense structures with D_f about 2.5. In real case, particles are not single-scale or identical throughout most of an aggregation process, flocs growth occurs as a result of cluster-cluster collisions. Computer modeling and experimental studies describing various model colloids have shown that cluster-cluster flocs have D_f values of around 1.8 at DLA and 2.1 at RLA, respectively (Lin et al., 1989). For particle-cluster aggregation induced by shear coagulation, much more compact structures result with D_f values in excess of 2.5 (Torres et al., 1991). Cluster-cluster flocs are evidently looser on the average than particle-cluster flocs (Gregory, 1997). In water treatment, however, the magnitude of D_f is subjected to the nature of the flocs. Li and Ganczarczyk (1989) have estimated the fractal dimension for various flocs in water and waste treatment process. They demonstrated that alum flocs have higher D_f values in the range from 1.59 to 2.32, while activated sludge flocs have D_f values ranging from 1.4 to 2.07. From the results of these literatures, as the fractal dimension decrease, the density of the particles falls off with distance from the center of the flocs.



2.4.3 Flocculation Strength

Experimental studies have indicated that the flocs strength is closely related to fractal dimension and flocs structure that are significantly affected by the intensity of turbulence (Tambo and Hozumi, 1979; Sonntag and Russell, 1986). Flocculation strength represents the resistance of a floc against rupture induced by shear stress. As flocs expose to a given shear condition, the flocculation strength can be measured by applying an increased shear rate to the aggregates and relating velocity gradient applied to the maximum floc size (Francois, 1987). There are simple relationship on a log/log scale between the G -value at a steady-state condition in which the rate of disaggregation equals the aggregation rate and the maximum flocs diameter in equilibrium. From this, the stable floc size decreases as the mixing intensity increases:



$$\log d_{\max} = \log C - \gamma \log G \quad (\text{Eq. 2.4})$$

where d_{\max} is the maximum flocs diameter (m); C is the flocculation strength coefficient that strongly depends on the manner for particle size measurement; G is the average velocity gradient (s^{-1}) and γ is the stable floc size constant, exponent dependent upon flocculation breakup mode and the size of eddies that causes the breakage. A plot of the maximum floc size remaining against the average velocity gradient gives a line with a characteristic slope that indicates flocculation strength and breakup mode. Likewise, the steeper the slope γ , the more inclined the flocs are to break into smaller size with increasing shear force, and thus the γ value is considered as a factor of flocculation strength. Generally, flocculation strength is positively correlated with fractal dimension (Li et al., 2007).

2.5 Surface Observation by Atomic Force Microscopy

Atomic force microscopy (AFM) can provide both digital images and interaction forces between surface and scanning tip from micro-range to nano-range in air or liquid environment. **Fig. 2.9** is a standard schematic of AFM with a cantilever for surface imaging. The cantilever is usually formed by one or more beams of silicon or silicon nitride. As the piezoelectric scanner on which the sample is located approaches the nano-scale sharp probe closely, and then the sample is scanned by the piezoactuator, the sensitive cantilever deflection due to interactive force between tip and surface atoms of the sample is monitored continuously. This cantilever deflection is quantified by optical technology, of which a beam from a vertical laser diode is focused onto an end of cantilever and its deflective position is monitored by a photodiode. AFM converts the changes in the position of the laser spot on the photodetector in voltage into the change of optical pathlength. By this way, the topographic images can be obtained by recording the cantilever deflection.

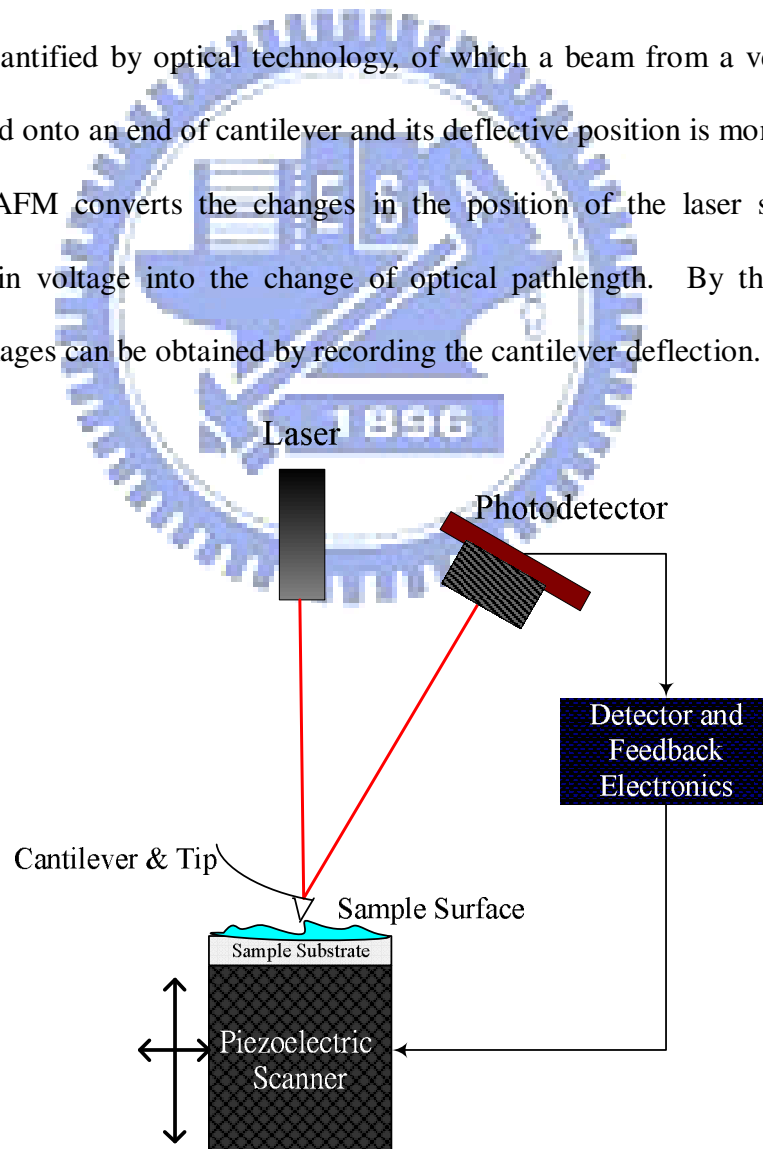


Fig. 2.9 Schematic diagram of atomic force microscope.

The AFM can be conducted in many modes. These different techniques are categorized “imaging modes” by the way of motion of AFM probe over the sample surface during scanning. They provide a multi-function imaging manner to scan different types of samples. Three primary imaging modes are known as contact mode, non-contact mode and tapping mode. Because the tip-surface interaction is affected by the nature of the sample, the choice of appropriate imaging mode depends on the specific application in different ambient conditions. **Fig. 2.10** shows the relationship between interactive force and tip-to-sample distance, which illustrates the interactive force domain of three imaging modes.

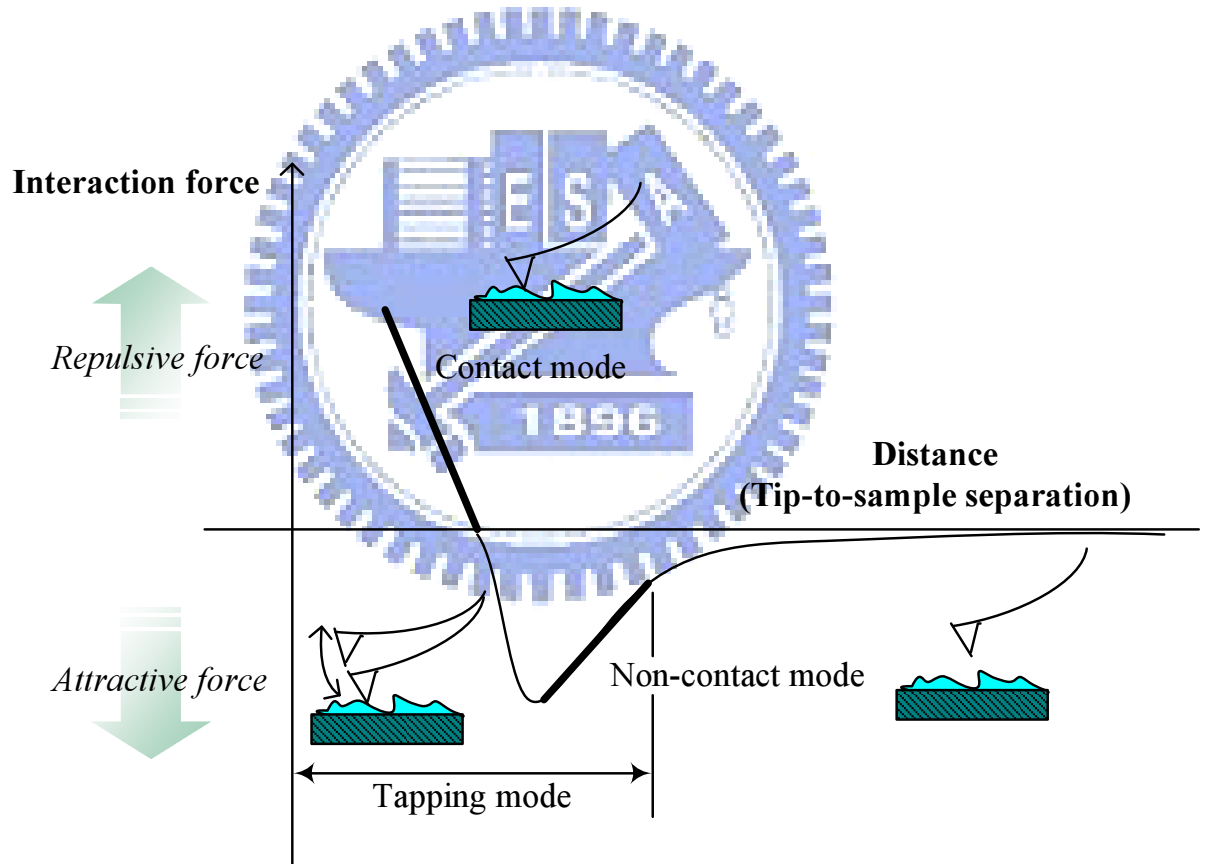


Fig. 2.10 Illustration of the interaction force between tip-to-sample surface distance.

In the past decade, AFM has been more extensively used to observe various materials including hydrophilic and hydrophobic surfaces, and biological molecules with different mode of operation. AFM makes it possible to in-situ observe the detailed structure of a single polymer on a molecular scale. A few attempts have been carried out to observe single polymers as well as Al_{13} on surfaces, using either tapping-mode AFM or the noncontact-mode AFM (Akari et al., 1996; Hu et al., 2005; Shu et al., 2001). However, these experiments were conducted under dry conditions so that the morphology observed may differ from the structure of polymers in the solution, because the morphology of polymers will change in the drying process. For this reason, contact-mode AFM was tried to in-situ observe the structure of a polymer, adsorbed on mica surface in water (Stipp, 1996). But the images obtained are not necessarily of high resolution and are strongly affected by the samples used, which is due to the fact that the samples are often destroyed at contact-mode AFM. Lately, many studies have been successfully conducted to in-situ observe the polymers and how polymers relax with time using tapping-mode AFM in aqueous environment on molecular-scale (Arita et al., 2004; Yamamoto et al., 2005). Biological matters also have been widely examined by tapping-mode AFM in liquid system at which the condensation and aggregation driven by capillary forces that changes the structure of sample in air can be avoided (Putman et al., 1994; Ikai, 1996; Wadu-Mesthrige et al., 2001). Thus, AFM is a powerful tool for in-situ molecular-scale observation of the biological and polymeric materials applied in water/wastewater treatment process.

CHAPTER III

EXPERIMENTAL MATERIALS AND METHODS

3.1 Materials

3.1.1 Synthetic Water Sample

The purified kaolin (Sigma Chemical Co., USA), which is polygonal as illustrated in **Fig. 3.1**, was mixed with RO water and dispersed for 30 minutes to a concentration of 2.5 g/L. In order to produce the well-suspended particles in synthetic water sample, the larger particles were removed from water by settling. After 24 hours settling, the supernatant was used as the synthetic stock solution, from which the RO water was added to prepare the turbid water samples to the desired turbidity of 50 NTU, which is about 20.3 mg/L. Particle size distribution of the synthetic suspension was analyzed by a particle size analyzer (Mastersizer 2000, Malvern Inc., UK) and the result is shown in **Fig. 3.2**. The mean particle size of the synthetic water sample was 2.9 μm . The specific conductivity of the working suspension was adjusted by 10^{-3} M NaClO_4 solution (Merck Inc., USA) and the alkalinity was adjusted by 10^{-3} M Na_2CO_3 (Merck Inc., USA).

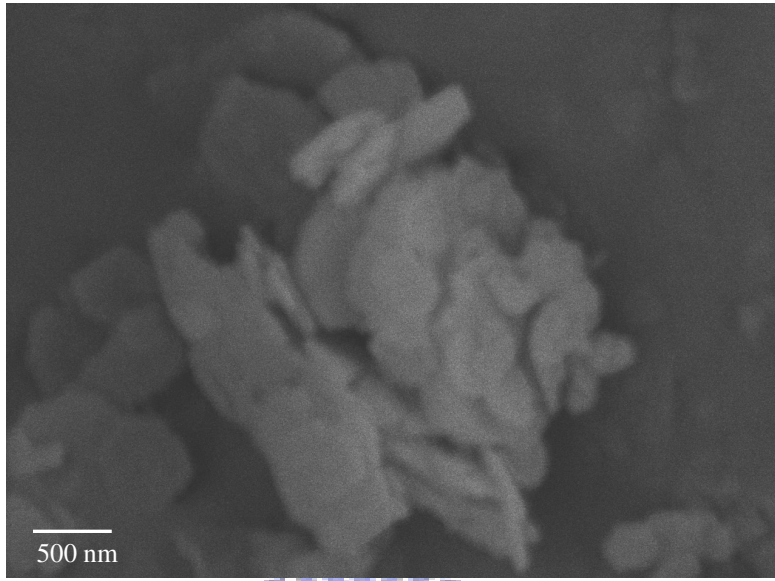


Fig. 3.1 SEM micrographics of purified kaolin powders.

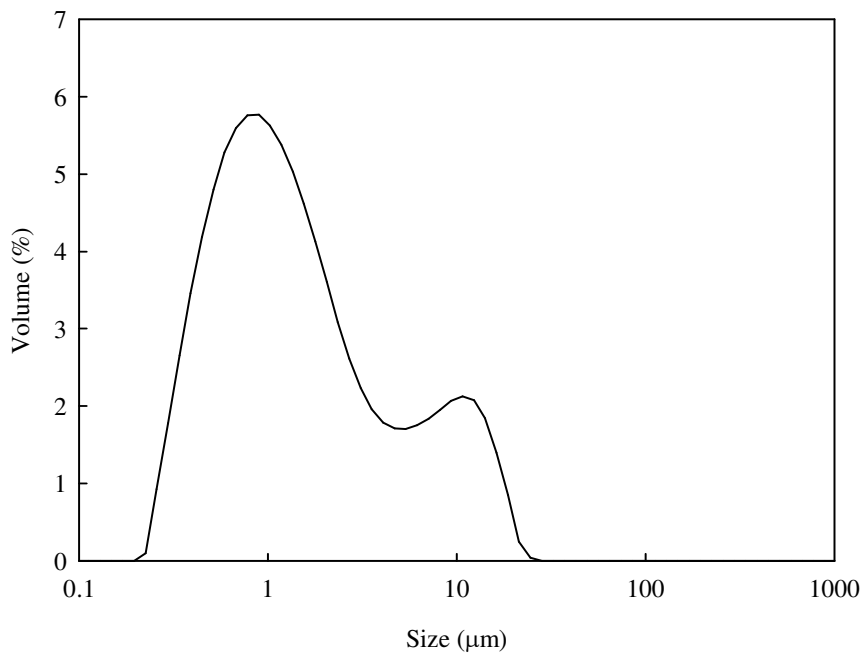


Fig. 3.2 Particle size distribution of the kaolin suspension.

3.1.2 Coagulants

Three PACl coagulants were used in this study. The reagent-grade PACl ($\text{Al}_2\text{O}_3 = 10\%$) was purchased from Showa Chemicals Inc., which is designated as PACl-C in this article. Another PACl named PACl-E, made by an electrochemical process, was a gift obtained from Research Center for Eco-environmental Sciences, Chinese Academy of Sciences in China. The $[\text{OH}^-]/[\text{Al}]$ ratio of PACl-C and PACl-E is 1.4 and 2.1, respectively. The other PACl is named PACl- Al_{13} which contains high Al_{13} contents separated from preformed PACl by sulfate precipitation and nitrate metathesis ($\text{SO}_4^{2-}/\text{Ba}^{2+}$ separation method) as reported elsewhere (Shi et al., 2007). The detail preparation process of PACl- Al_{13} is described in the section of Methods.

The working solutions containing 1,000 mg Al/L were freshly prepared from the stock solution before each experiment. Aluminum concentration was analyzed by an inductively coupled plasma atomic emission spectrometry (ICP-AES) (JY24, Jobin-Yvon Inc., France). The Al speciation of PACl-C, PACl-E and PACl- Al_{13} was identified by both Ferron assay and ^{27}Al nuclear magnetic resonance (^{27}Al -NMR) method that are described in next section.

3.2 Methods

Various PACl coagulants were prepared and characterized to evaluate the destabilization of kaolin particles in coagulation experiments that were carried out with jar tests. The predominant destabilization mechanisms of coagulation with various PACl coagulants were determined. Flocs growth was monitored during coagulation, and the regimes of particle aggregation were evaluated. Furthermore, characteristics of flocs formed under various coagulation mechanisms such as size, fractal dimension, morphology, and surface Al composition were also identified. On the other hand, the size and morphology of Al_{13} aggregates formed at various Al concentrations were examined.

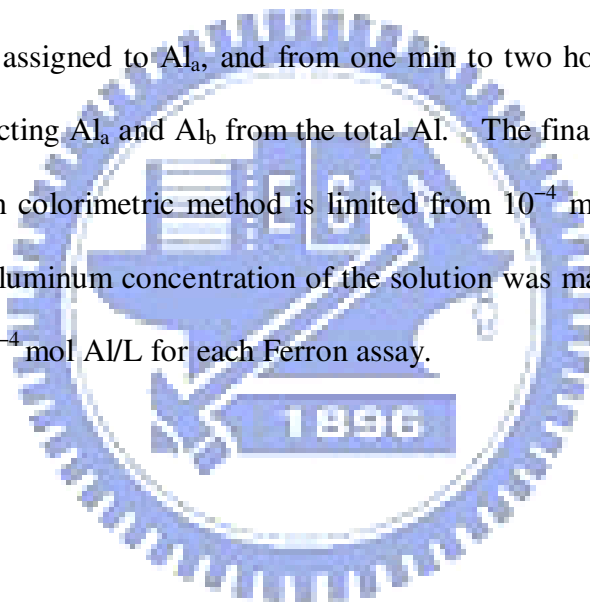
3.2.1 Ferron Assay

In this study, a slightly modified version of the Ferron colorimetric method was used, which avoids some unstable features (Wang et al., 2004). The major procedure of Ferron assay was depicted as follows:

Three reagents are first prepared and mixed as Ferron colorimetric solution. Reagent A (0.2% ferron) for which 2g ferron (8-hydroxy-7-iodo-5-quinoline-sulfonic acid, Merck Inc., USA) was dissolved in 1020 mL distilled water and then boiled to remove dissolved CO_2 . After that, the boiled solution was filtered and preserved in a 1 L volumetric bottle. Reagent B (20% w/v NaAc) for which 200g NaAc was dissolved in 1 L distilled water. Reagent C (1:9 v/v HCl) for which 100 mL HCl (37%) was mixed with 900 mL distilled water.

Prior to Ferron assay, three reagents was mixed as a Ferron colorimetric solution according to a specific volumetric ratio (A:B:C=2.5:2:1). In mixing process, the reagent B and C are mixed first before the addition of reagent A. Then, 5.5 mL

mixed Ferron colorimetric solution was transferred into 25 mL graduated plastic tube and diluted to certain volume with distilled water. The 5 mL coagulant sample was then added into the tube and quickly diluted to 25 mL. After homogeneous mixing, the reacting sample was quickly added to a 1-cm glass cuvette to quantify Al species by carrying out timed absorbance measurements at 366 nm with UV-Visible spectrometer (U3010, Hitachi Inc., Japan). The illustration of Ferron colorimetric method is given in **Fig. 3.3**. Based on the kinetics of the reactions between the aluminum species and Ferron agent, the hydrolyzed Al species can be categorized into three groups: Al_a, monomeric; Al_b, polymeric; and Al_c, colloidal. The absorbance in the first minute is assigned to Al_a, and from one min to two hours to Al_b. Al_c was obtained by subtracting Al_a and Al_b from the total Al. The final concentration of the solution for Ferron colorimetric method is limited from 10⁻⁴ mol Al/ L to 10⁻⁵ mol Al/L. The total aluminum concentration of the solution was maintained in the range of 2 × 10⁻⁴ to 4 × 10⁻⁴ mol Al/L for each Ferron assay.



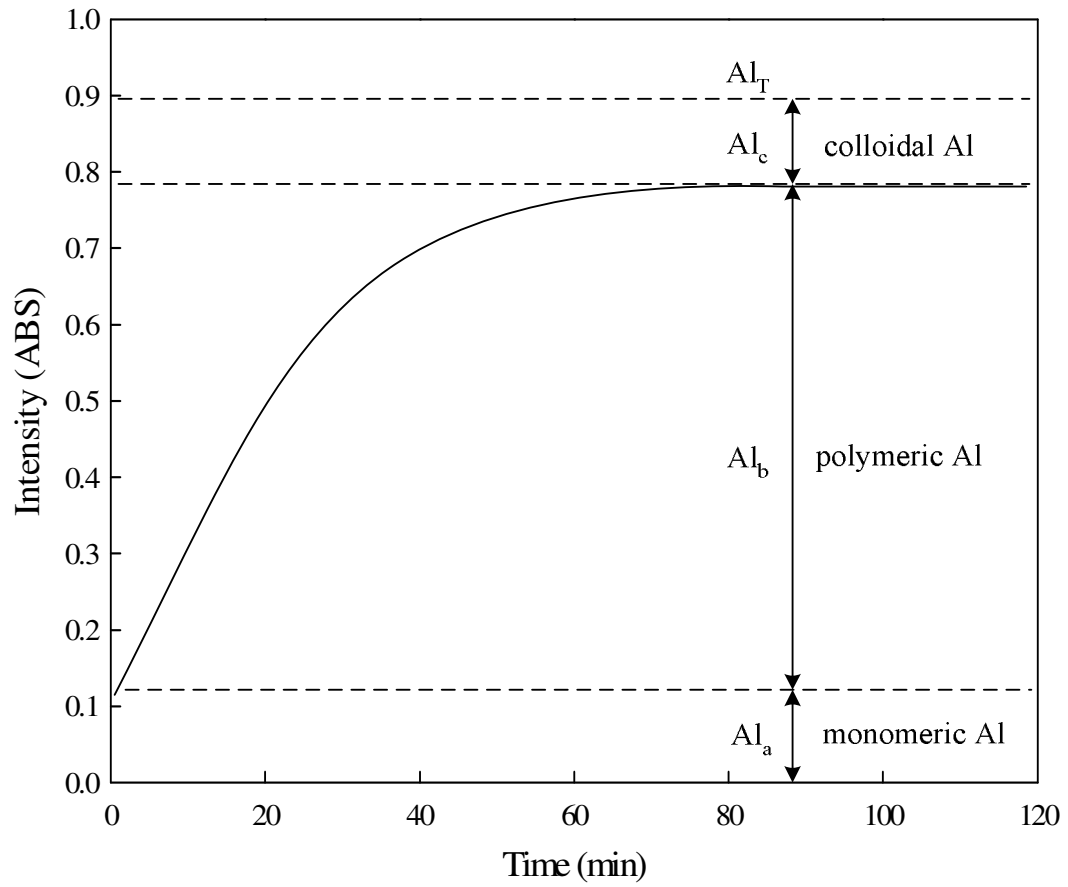
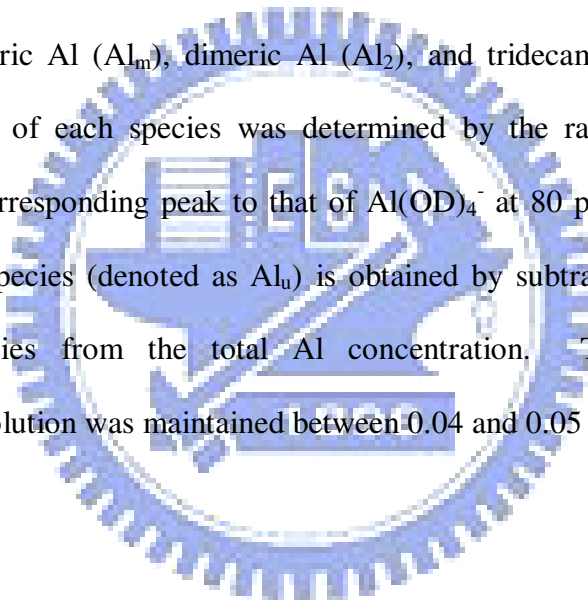


Fig. 3.3 Illustration of Ferron colorimetric method.



3.2.2 ^{27}Al -Nuclear Magnetic Resonance (NMR)

The distributions of hydrolyzed species of PACl , PACl-E and PACl-Al_{13} in solution were determined with a 500 MHz ^{27}Al -NMR (Uniytinova-500, Varian, USA). The operation parameters for the NMR analysis are spectrometer frequency, solvent, and temperature, which are 130.246 MHz, D_2O , and 298K. A 5-mm sample tube (Wilmad 507-pp, SP Industries Inc., USA) containing 3 mL Al solution and a 4.2-mm sample tube (Wilmad WGS-5BL, SP Industries Inc., USA) containing 1 mL 0.05 M $\text{Al}(\text{OD})_4^-$ solution were inserted together as the inner standard. The chemical shift of $\text{Al}(\text{OD})_4^-$ is at 80 ppm. The signals in the proximity of 0, 3 to 4, and 62.5 ppm represent monomeric Al (Al_m), dimeric Al (Al_2), and tridecamer Al_{13} , respectively. The concentration of each species was determined by the ratio of the integrated intensity of the corresponding peak to that of $\text{Al}(\text{OD})_4^-$ at 80 ppm. The amount of the undetectable species (denoted as Al_0) is obtained by subtracting the sum of the detected Al species from the total Al concentration. The total aluminum concentration of solution was maintained between 0.04 and 0.05 mol/L.



3.2.3 Preparation and Characterization of PACl- Al_{13}

A PACl solution was first prepared with the mixing of aluminum chloride ($\text{AlCl}_3 \cdot 6\text{H}_2\text{O}$) and sodium carbonate (Na_2CO_3) solid powder. Pre-weighed amount of aluminum chloride was dissolved into a 500 mL glass beaker, and then at intense agitation, sodium carbonate was slowly added into the beaker. The dosing speed of Na_2CO_3 was well adjusted to avoid the occurrence of visible precipitates. The amount of Na_2CO_3 was determined according to target basicity ($\gamma=2.3$). Temperature was held at 60 ± 2 °C. After the addition of Na_2CO_3 , the reaction system was cooled down to room temperature. After preparation, the PACl solution was set for at least 24 hours of aging at room temperature, and then stored in refrigerator.

A given tailor-made PACl was chosen to be purified by $\text{SO}_4^{2-}/\text{Ba}^{2+}$ separation method. Hundred millilitre of PACl solution was poured into a 1 L glass beaker, and then a precalculated amount of Na_2SO_4 solution was introduced with 1:1 $\text{SO}_4^{2-}/\text{Al}$ molar ratio under magnetic stirring. The concentration of Na_2SO_4 solution was adjusted according to the designed total Al concentration of 0.1 M (denoted as Al_T) in the reaction process. Based on the different reaction rate between SO_4^{2-} and various Al species, the rapid precipitation (SO_4^{2-} -colloidal Al precipitates) obviously occurs after 5 min; however, the reaction between Al_{13} and SO_4^{2-} was very slow (Xu et al., 2003). Because, the transition period between sulfate with colloidal Al and Al_{13} are quite short and its transition rate tremendously depends on the Al_T , scanning electron microscope (SEM) was used to observe the precipitate morphology and determine the optimum reaction time for the separation between colloidal Al and Al_{13} . **Fig. 3.4** presents the images of precipitates formed at a given $\text{SO}_4^{2-}/\text{Al}$ molar ratio, reaction time and Al_T , which are 1.0, 5 min and 0.1 M, respectively. In this insert, tetrahedral-shaped crystals were found, which is attributed to the precipitates formed

via the complexation of sulfate with Al_{13} (Xu et al., 2003). This result indicates that a certain amount of Al_{13} -sulfate crystals occurs and the reaction between colloidal Al and sulfate has been profound after 5 min reaction for the study. Thus, samples in the mixed solution here were taken after 5 min agitation and filtered in 2 min using G3 filter (Kimax, USA) to separate the colloidal Al and Al_{13} from the tailor-made PACl. The filtrate was set after 24 hours and consequently the occurrence of precipitate, and then it is filtered by membrane whose pore size is $0.45\ \mu m$ (Advantec MFS Inc., USA). The precipitates obtained were dried at room temperature and stored for the next metathesis process. These precipitates mainly consist of Al_{13} -sulfate crystals (term as $Al_{13}-(SO_4)_n$).

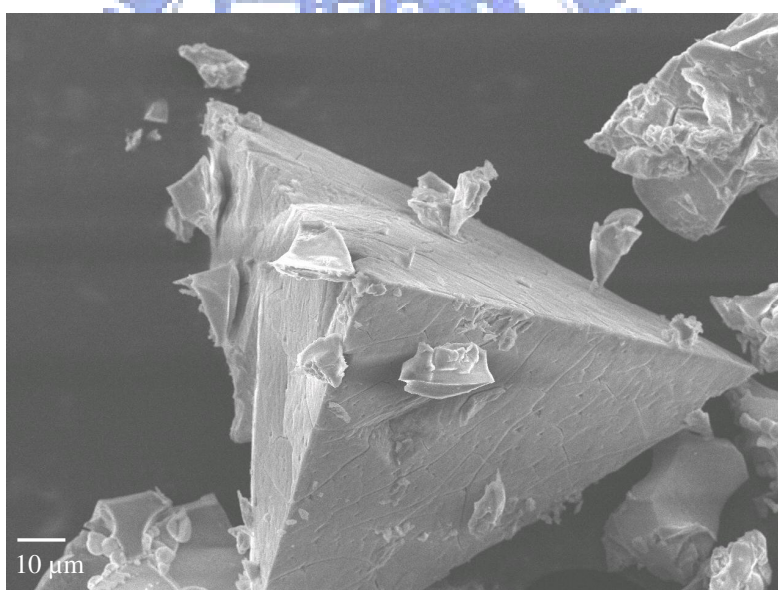
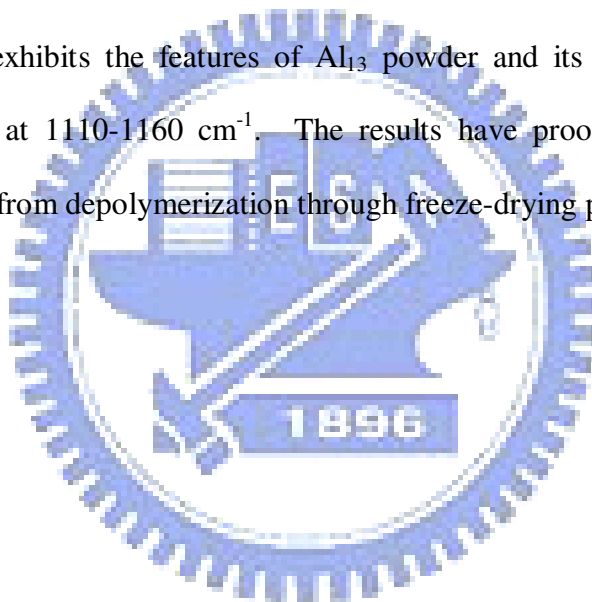


Fig. 3.4 The SEM images of $Al_{13}-(SO_4)_n$ precipitate. (700)

In order to obtain soluble Al_{13} products, further ion metathesis reaction was performed to release Al_{13} from solids into solutions. This metathesis process was conducted by 0.3 M $Ba(NO_3)_2$ solution. A 2.73 grams of $Al_{13}-(SO_4)_n$ solid was transferred into a 200 mL glass beaker, and 20 mL of distilled water was added to pre-disperse the solid, then a certain amount of $Ba(NO_3)_2$ solution was intensively mixed with $Al_{13}-(SO_4)_n$ suspension for 90 min. After metathesis process, insoluble solids and soluble Al_{13} were separated by filtration with membrane of 0.45 μm . The Al_{13} solution after metathesis reaction was put into a vacuum freeze-dryer (FD2-D, Kingmech Co., Ltd, Taiwan) and then dried at around -50 by freeze-drying. Dried solid Al_{13} was collected and sealed in a plastic bottle, which can provide a long-term preservation of Al_{13} .

To verify whether the Al_{13} structure could be destructed during the freeze-drying process of this study, the freeze-drying Al_{13} powder was analyzed by solid-state ^{27}Al -NMR (DSX-400WB, Bruker, Germany), FTIR and high-resolution XRD (D1, Bede, UK). As shown in **Fig. 3.5**, solid-state ^{27}Al -NMR spectra represents that the chemical shift peaks at 63 ppm obviously, which indicates Keggin Al_{13} subsists in the solid Al_{13} powder. On the other hand, the HR-XRD pattern illustrates that solid Al_{13} powder has no well formed crystalline structure except for the diffraction peaks at 8.1° which is assigned to the solid Al_{13} crystalline structure (Cheng and Chou, 2000), as presented in **Fig. 3.6**. Furthermore, FTIR spectra of Al_{13} powder are depicted in **Fig. 3.7** and various vibrational assignments are listed in **Table 3.1**. The frequency between 3400 and 3600 cm^{-1} , corresponding to the O-H stretching vibration of H-bonded water (Johnston et al., 1992; Madejova et al., 2002), is observed. The ambiguous stretching band at around 2400 cm^{-1} is assigned to characteristic vibration of Al-O (Wang et al., 2006). It also can be seen that the symmetric H-O-H bending

vibration of water molecules presents at about 1640 cm^{-1} , which should be attributed to increase of water content due to the interaction of hydroxyl-Al cations into the interlayer space of Al_{13} powder. The obvious band at around 729 cm^{-1} is ascribed to the symmetric Al-O stretching vibration in the Keggin hydroxyl-Al (i.e., $[\text{AlO}_4\text{Al}_{12}(\text{OH})_{24}(\text{H}_2\text{O})_{12}]^{7+}$), similar to the previous study (Bradley, et al., 1993). Furthermore, some of the frequencies between 400 and 1000 cm^{-1} are the vibration of surface OH group. For example, the band at around 630 and 494 cm^{-1} , corresponding to Al-OH and Al-OH₂ stretching vibration, are gained. The Al-OH-Al bending vibration is also found at the frequency of 990 cm^{-1} . The figure of FTIR spectra exhibits the features of Al_{13} powder and its sulfate that shows a typical S-O band at 1110 - 1160 cm^{-1} . The results have proved that Al_{13} can be preserved in solid form from depolymerization through freeze-drying process.



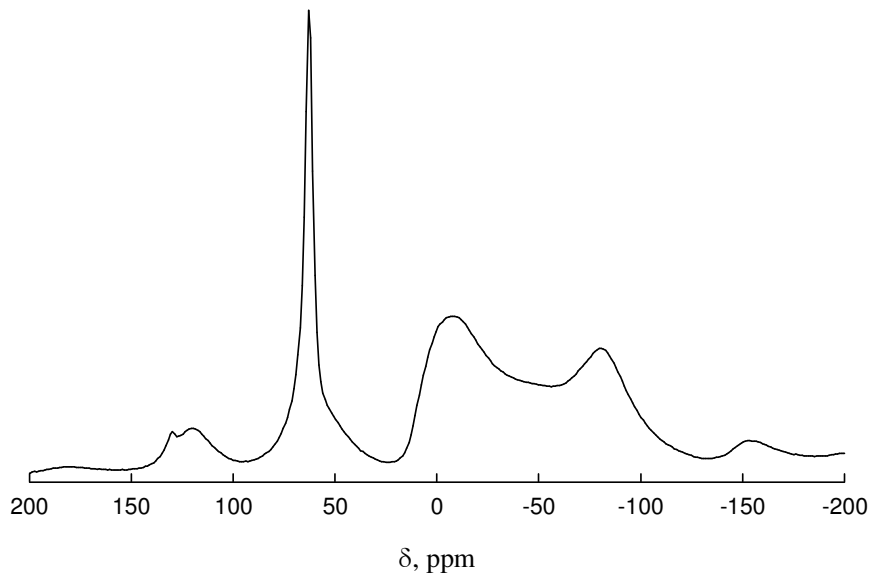


Fig. 3.5 Solid-state ^{27}Al -NMR spectrum of solid Al_{13} powder.

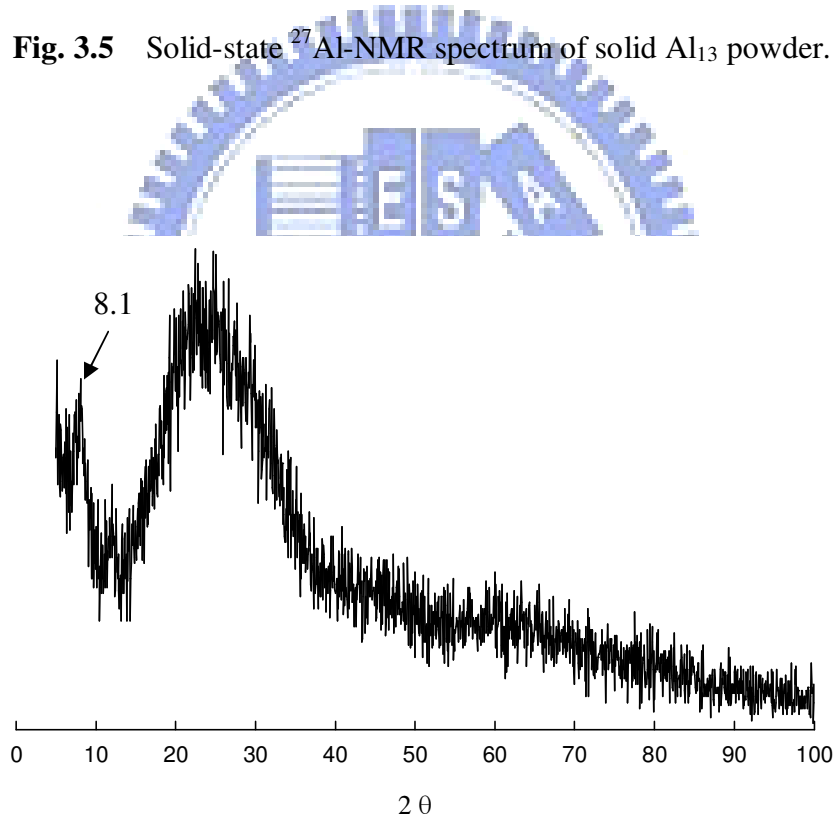


Fig. 3.6 HR-XRD pattern of solid Al_{13} powder.

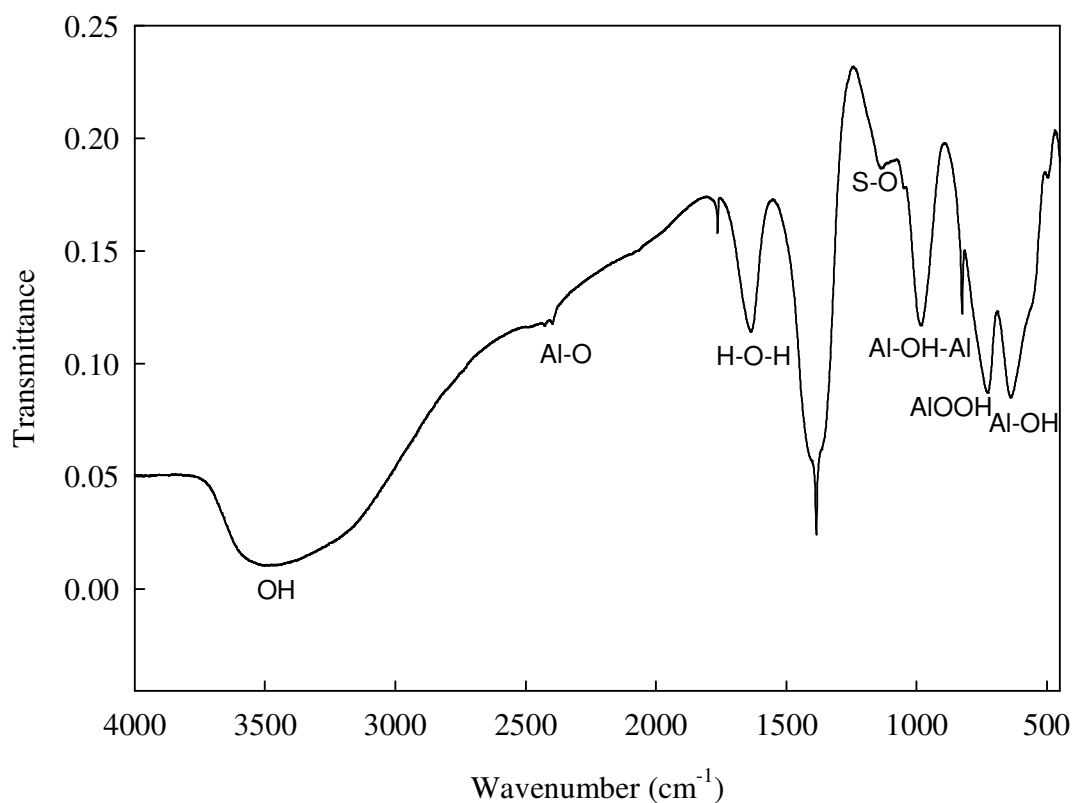


Fig. 3.7 FTIR spectra of Al₁₃ powder.

Table 3.1 FTIR vibrational assignment of Al₁₃ powder

Wavenumber (cm ⁻¹)	Assignment
3400-3600	OH
2400	Al-O
1641	H-O-H
1100-1160	S-O
990	Al-OH-Al
729	Keggin-Al ^{IV} OOH
630	Al-OH
494	Al-OH ₂

3.2.4 Coagulation Experiments

Standard jar tests were conducted in one-liter beakers to evaluate coagulation efficiencies and predominant coagulation mechanism. The mixing device was a square acrylic vessel (11.5 cm in length 11.5 cm in width 21 cm in height) which was commonly applied to as a gator jar. The flat rectangular blade with a 76 mm 25 mm, driven by a single thin spindle via a motor of adjustable speed up to 300 revolutions per minute (rpm) (Hsingtai Co., Taiwan), was centrally located in the vessel while mixing for each experiment. The coagulant was slowly injected above the liquid surface. This mode of injection can avoid the unstable and inaccurate dosing. The velocity gradient (G-values) was determined as reported by Cornwell and Bishop (AWWA, 1992), as shown in **Fig. 3.8**. In the jar test of this study, an initial rapid mixing was conducted at 200 rpm ($G = 350 \text{ s}^{-1}$) for one min followed by a slow mixing at 30 rpm ($G = 25 \text{ s}^{-1}$) for 20 min. Zeta potential (ZP) was measured immediately by a Zeta-meter (Zetasizer nano ZS, Malvern Inc., UK) without dilution after the rapid mixing. The suspension was left undisturbed for 20 min. After settling, the residual turbidity (RT) of the supernatant was measured by turbidimeter (2100 P, Hach Inc.).

On the other hand, the effects of pH on Al speciation in coagulation were investigated via Ferron assay to understand the transformation of Al species. For this evaluation, solutions contained $10^{-3} \text{ M NaOCl}_4$ and $10^{-3} \text{ M Na}_2\text{CO}_3$ to maintain the conductivity and ionic strength for each test. Various amounts of NaOH and HCl solutions were added to the solutions to maintain the final pH. After the addition of the coagulant, the solution was stirred at 200 rpm for one min followed by the Ferron assay. The total aluminum concentration of the solution was held at 0.2 mM Al for each pH condition. All the experiments were carried out at $23 \pm 1^\circ\text{C}$.

To study the effects of dosage on the size of Al_{13} aggregates, the solution without particles were employed as the blank sample. The PACI- Al_{13} was used as a coagulant to evaluate the formation of Al_{13} aggregates after dosing in the blank sample. After the addition of PACI- Al_{13} , the sample was first stirred at 200 rpm for one min under pH 10 and then a small amount of sample was withdrawn for size measurement and AFM imaging. At the same mixing condition, the PACI-C was added into blank sample to evaluate the formation of $Al(OH)_3$ precipitates at neutral pH by WSEM in order to in-situ observe the morphology of $Al(OH)_3$ precipitates.



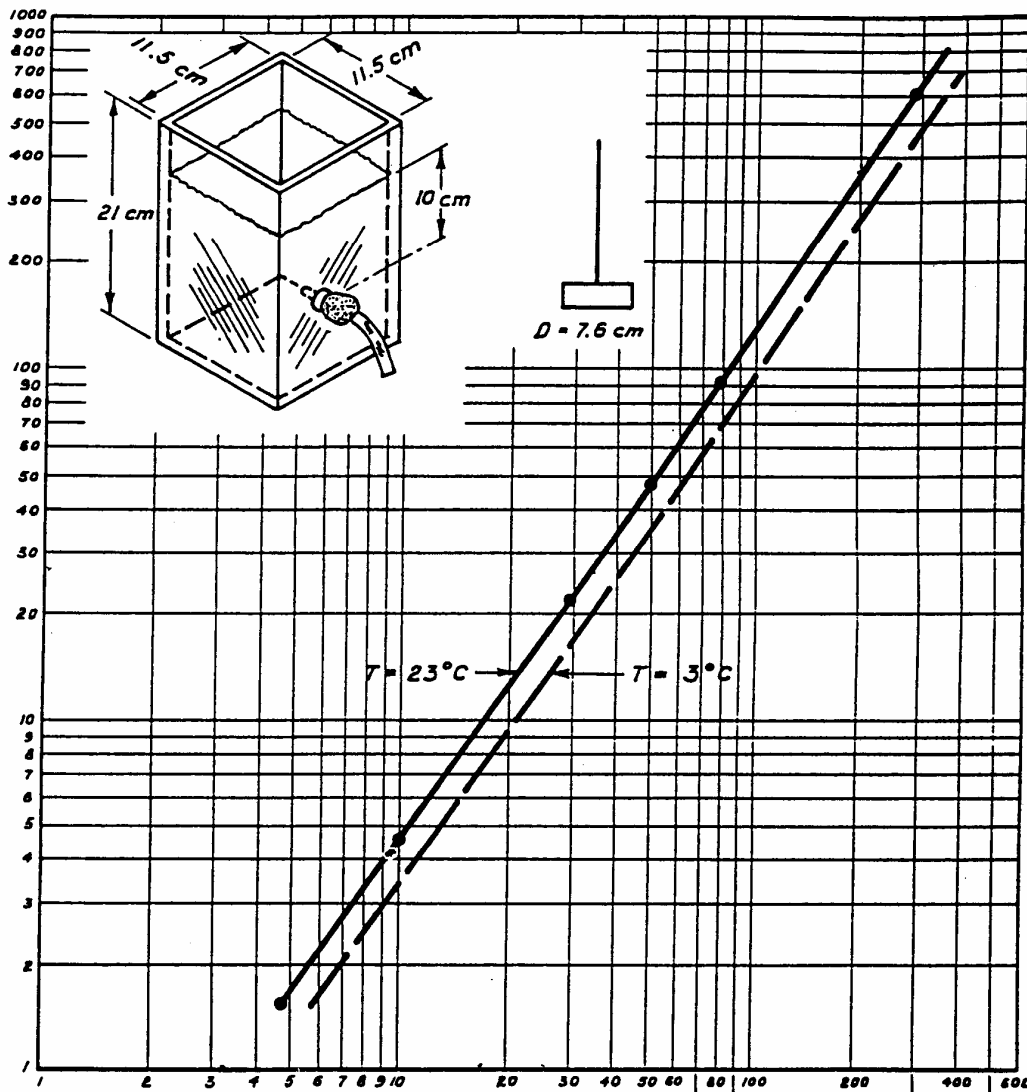


Fig. 3.8 G curve for flat paddle in the gator jar.

3.2.5 Measurement of Floc Size and Structure

A particle size analyzer (Mastersizer 2000, Malvern, UK) with a small angle static light scattering (SASLS), which consists of a 5-mW Helium-Neon laser (wavelength is about 632 nm) as the light source and an optic lens and photosensitive detectors, was used to directly monitor the dynamics of flocs growth during coagulation process and the structure of kaolin flocs. The materials in the range from 0.02 μm to 2000 μm are available for size measurement. The similar jar tests were performed to observe the dynamics of coagulation for the study. During coagulation, the suspension was pumped to the particle size analyzer by a peristaltic pump (EW-7553-70, Cole-Parmer Instrument Co., USA) with a Tygon tubing (Masterflex-06409-16, Cole-Parmer Instrument Co., USA) of 3.1 mm (I.D.), and the sample was recycled back to the mixing vessel at a flow rate of 20 ml/min. Based on the results of previous study (Kan et al., 2002), the shear and disruption of aggregates in such setup are negligible, which as depicted in **Fig. 3.9**.

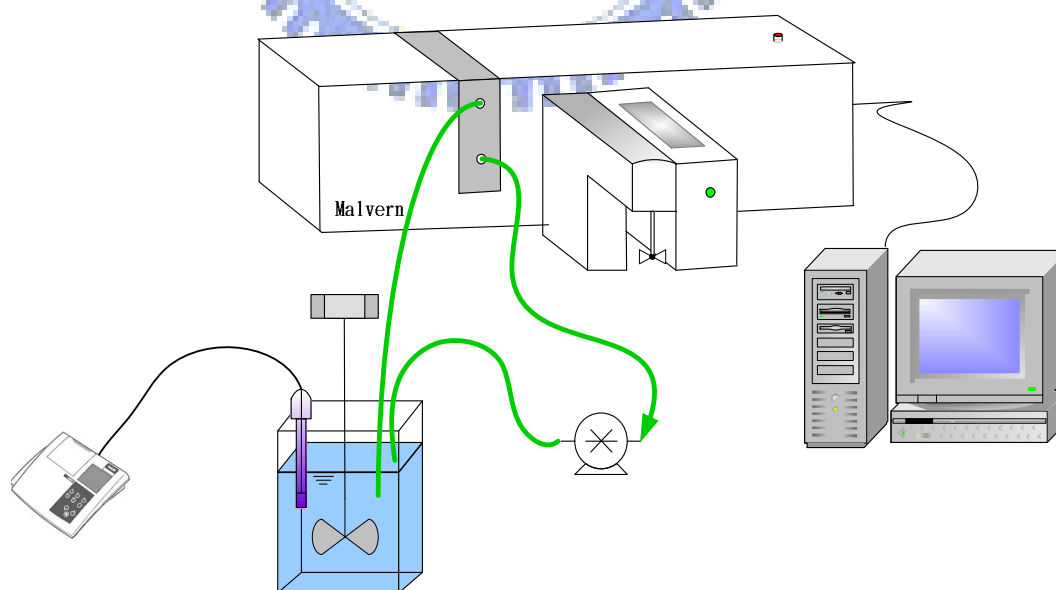


Fig. 3.9 Construction of laboratory coagulation system incorporated with SASLS.

A mass fractal is a mathematical description of highly irregular geometric shapes (Mandelbrot, 1983), which is further applied to demonstrate the complex structure of particle flocs generated in water and wastewater treatment processes (Guan et al., 1998; Li and Ganczarczyk, 1989). The mass fractal suggests that the structure of flocs is self-similar at various length scales or scale invariance. For a mass fractal floc, the mass, M , of a fractal with fractal dimension, D_f , is proportional to its size, R , raised to power D_f (Mandelbrot, 1983):

$$M(R) \propto R^{D_f} \quad (\text{Eq. 3.1})$$

The SASLS has been extensively employed to evaluate the size of particles and aggregates in various suspensions, such as kaolin, latex, and aluminum suspension (Waite et al., 2001; Berka and Rice, 2005). The scattered light intensity I is measured as a function of the magnitude of the scattering wave vector, Q . The relationship between the scattered intensity from the aggregate, $I(Q)$, and the Q is given by (Lin et al., 1989):

$$I(Q) \propto Q^{-D_f} \quad (\text{Eq. 3.2})$$

where

$$Q = \frac{4\pi n \sin(\theta/2)}{\lambda} \quad (\text{Eq. 3.3})$$

Here, n is the refractive index of the fluid, λ is the wavelength in vacuum of the laser light used, and θ is the scattering angle. This relationship is valid when the length

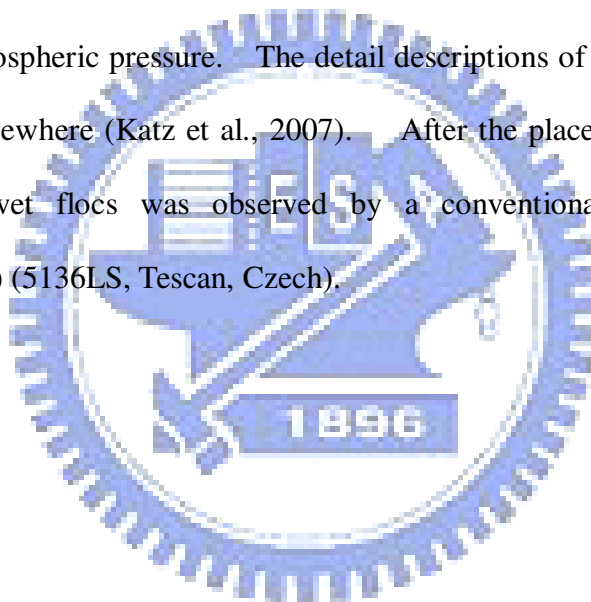
scale of $1/Q$ is much larger than the primary particles and much smaller than aggregates. The mass fractal dimension D_f can be estimated from the absolute slope of $\log I(Q)$ versus $\log Q$ by fitting a straight line through the fractal region of scattering plot. Although the diameter of the primary particles used in this study is larger than the lasers wavelength, the scattering exponents, obtained from SASLS assay (i.e., D_s) does relate to the structure properties of primary flocs rather than entire flocs, which can be explained by the existence of two-level floc structural model that is derived by other investigators (Wu et al., 2002). According to the Q range of original kaolin particles (corresponding to R values of 1.5 μm), the SASLS experiments have been restricted to the 10^{-3} to $4.5 \cdot 10^{-4} \text{ nm}^{-1}$ Q range to allow the power law regime for the structural analysis of flocs (corresponding to R values of 100-250 μm). Many studies also have successfully used SASLS assay to evaluate the fractal dimensions of the floc aggregated from micro-scale primary particles in coagulation process (Annadurai et al., 2004; Chu et al., 2004; Yu et al., 2006). Therefore, the D_s values of micro-scale flocs measured here are comparable.

3.2.6 Solid-state ^{27}Al Magic-angle Spinning Nuclear Magnetic Resonance

The solid-state magic-angle spinning nuclear magnetic resonance (MAS-NMR) spectra were recorded by a Bruker instrument (DSX-400WB, Bruker, Germany) in 4 mm rotors, and the ^{27}Al spectra were recorded at 104.1 MHz. The solid-state ^{27}Al MAS-MNR was performed on freeze-drying PACl-C, PACl-E and PACl- Al_{13} flocs samples at various dosages of coagulant other than the prepared Al_{13} powder. Various flocs formed after coagulation was separated immediately for following drying process. The separated flocs samples were freeze-dried over 24 hours with a vacuum refrigerating instrument.

3.2.7 Wet Scanning Electron Microscope

A novel wet scanning electron microscope (WSEM) that allows directly image the morphology of flocs in liquid system has been used in the field of material development (Gallucci and Scrivener, 2007). Various flocs formed after coagulation were readily withdrawn into a sealed specimen capsule (QX-102, Quantomix Co. Ltd, Israel). The top of the capsule is composed of a thin grid on which flocs were protected from vacuum in the microscope by an electron-transparent partition membrane, which is illustrated in **Fig. 3.10**. Therefore, imaging by this way can make the micron-scale observation of fully hydrated samples or water solution maintained at atmospheric pressure. The detail descriptions of the specimen capsule were presented elsewhere (Katz et al., 2007). After the placement of samples, the morphology of wet flocs was observed by a conventional scanning electron microscope (SEM) (5136LS, Tescan, Czech).



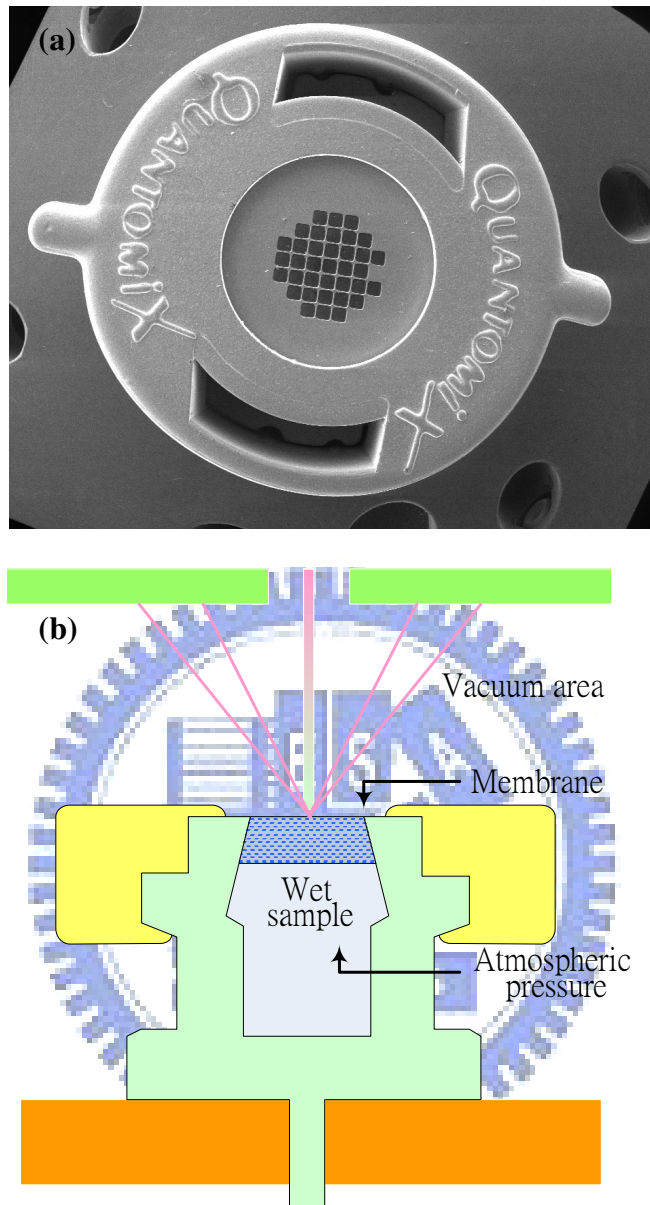


Fig. 3.10 Setup of WSEM: (a) Top scheme of QX-102 capsule and (b) Cross-section scheme of capsule.

3.2.8 Atomic Force Microscope

A Nanoscope III atomic force microscope (AFM) (Multimode, Digital Instruments Inc.) was used to observe the morphology of Al_{13} aggregates. A silicon cantilever with ultrasharp probe (NSC15, MilkroMasch, Spain), whose spring constant, resonance frequency, and nominal tip radius are 20-75 N/m, 265-400 kHz, and less than 10 nm, respectively, was employed to scan the image of sample in the tapping mode AFM (TM-AFM) that can avoid destroying the sample. TM-AFM has been widely applied in liquid environment to in-situ observe the surface morphology of polymer materials or biological matters, which can prevent the condensation of hydrous samples (Arita et al., 2004; Ikai, 1996). All the experiments here were conducted in liquid system at room temperature.

Before each AFM imaging test, mica plates were cleaned by the following process. First, the mica plates were immersed overnight in a 1 M HCl solution. They were then soaked in acetone for 30 min and boiled in a mixture of $5\text{H}_2\text{O}$: $1\text{H}_2\text{O}_2$: $1\text{NH}_4\text{OH}$ at 80 °C for 25 min. After that, the mica plates were washed by DI water. The same cleaning process has been used by other studies (Nalaskowski et al., 1999; Chin et al., 2002). Such a cleaned surface is fully wettable by water, and no contamination is detected by AFM.

After the mica plate was cleaned, the Al_{13} sample was placed on the mica plates, fixed by adsorption, and immediately measured by the tapping mode AFM. To maintain the AFM imaging in liquids, the mica plate with Al_{13} adsorbed on it was determined without resupplying water for at least one hour and the AFM imaging was conducted until the DI water was dropped on the surface of the mica. The setup of TM-AFM is demonstrated in **Fig. 3.11**. The ultrasharp probe was submerged in the meniscus drop and then the AFM scanning was carried out readily.

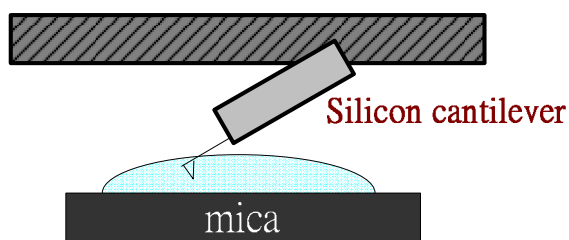


Fig. 3.11 Setup of liquid tapping mode atomic force microscope.

3.2.9 Field-Emission Electron Microscope

A field emission SEM (FE-SEM) (JSM-6330F, JEOL, Japan) equipped with an energy dispersive X-ray (EDX) spectrometer was used to image the $\text{Al}(\text{OH})_3$ -rich as well as Al_{13} -aggregate flocs samples at the acceleration voltage of 15 kV and 10 kV, respectively. Morphology observation for the flocs samples was conducted on high transmission electron microscope (HR-TEM) (JEM-2100F, JEOL, Japan) at the acceleration voltage of 160 kV.

3.2.10 High-resolution X-ray Powder Diffractometer

X-ray diffraction patterns were recorded between 5° and 100° (2θ) at a scanning speed of 1 min^{-1} by using high-resolution X-ray powder diffractometer (HR-XRD) (D1, Bede, UK) with Cu K radiation. All experiment samples were freeze-dried before each examine. The HR-XRD was employed to diagnose the crystalline structure of the prepared Al_{13} powder and various PACl flocs.

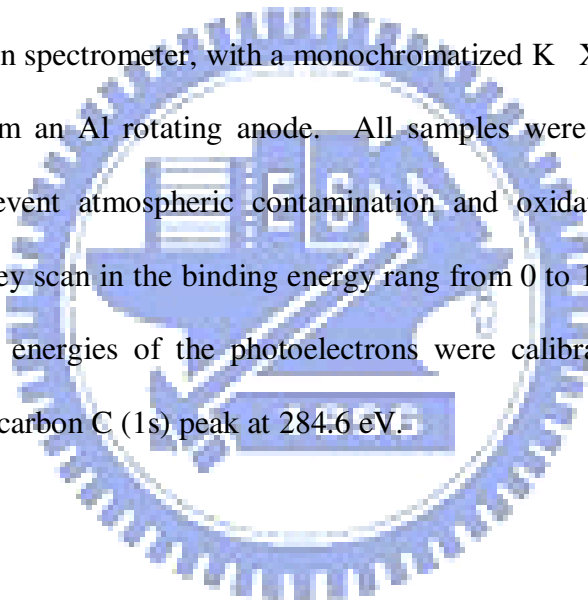
3.2.11 Fourier Transform Infrared Spectra

Fourier transform infrared spectra (FTIR) using KBr pressed disk technique were acquired on Fourier transform infrared spectrometer (DA8.3, Bomem, Canada).

Each sample was mixed with KBr powder grounded in an agate mortar for 5 min to achieve full mixture before making the flakes. The spectra were collected for each measurement in the spectral range of 400–4000 cm^{-1} with a resolution of 1 cm^{-1} . The FTIR was utilized to characteristic vibrations of various functional groups on the surface of the prepared Al_{13} powder.

3.2.12 X-ray Photoelectron Spectroscopy

The X-ray photoelectron spectroscopy (XPS) was applied to determine surface composition of Al-flocs to a depth of less than 10 nm. XPS was performed using an X-ray photoelectron spectrometer, with a monochromatized K X-ray beam at 3.8 kW was generated from an Al rotating anode. All samples were stored in a nitrogen atmosphere to prevent atmospheric contamination and oxidation. Each analysis started with a survey scan in the binding energy rang from 0 to 1000 eV at a step of 1 eV. The binding energies of the photoelectrons were calibrated by the aliphatic adventitious hydrocarbon C (1s) peak at 284.6 eV.



CHAPTER IV

EFFECT OF Al SPECIES TRANSFORMATION ON COLLOID DESTABILIZATION MECHANISMS

In this section, standard jar tests were carried out to evaluate the efficiency of turbidity removal. First, three types of PACl coagulants, namely PACl-C, PACl-E and PACl-Al₁₃, were used to coagulate the suspended kaolin particles. The effects of pH on coagulation were also evaluated. Zeta potential and residual turbidity for each coagulant at 1 mg/L were determined for this evaluation. In addition, three PACl coagulants were characterized by Ferron as well as ²⁷Al-NMR methods, and the effects of pH on Al species transformation was examined to evaluate the destabilization mechanisms of various PACl coagulants. On the other hand, the effects of dosage on particle destabilization mechanisms were further investigated through the analysis of the reactive Al species within flocs by solid-state ²⁷Al-NMR.

4.1 Effects of pH on Coagulation

The pH of solution principally influences the surface charge of particles such as zeta potential that rules the stability of particles in suspension system. Likewise, the Al species and their surface charge are significantly affected by pH values of solution, which leads to the variation in destabilization mechanism of particles. Literatures have indicated that pH change may have a profound impact on PACl coagulation as a result of motley hydrolyzed Al species (Wang et al., 2002; Hu et al., 2006). Therefore, the Al species distributions of various PACl coagulants applied in this study were determined. Several coagulation experiments were conducted to study the effects of pH on the Al species transformation as well as coagulation efficiency.

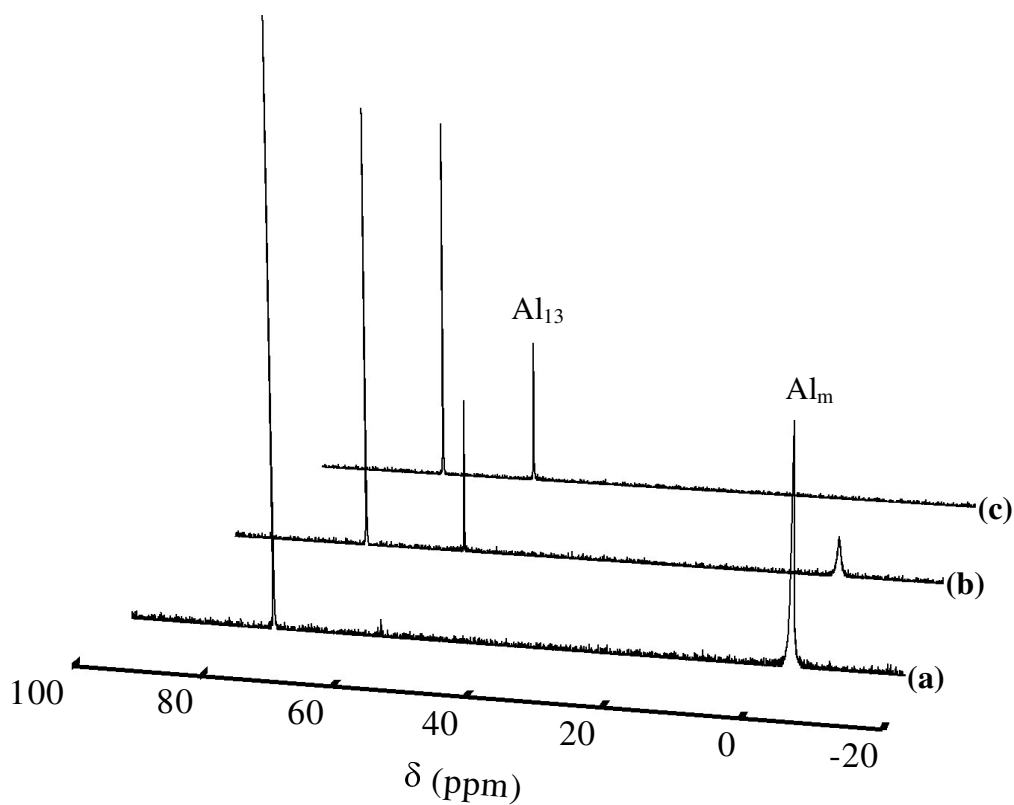
4.1.1 Characterization of Coagulants

The results of Al speciation for three coagulants used in this study are summarized in **Table 4.1**. By Ferron method, the major Al species of PACI-C are the Al_a (monomeric Al) and Al_c (colloidal $Al(OH)_3$), while the majorities of Al species in PACI-E and PACI- Al_{13} are found to be Al_b . The distributions of Al_m and Al_{13} measured by ^{27}Al -NMR correspond to the distributions of Al_a and Al_b obtained by Ferron method, respectively. Although there is a little discrepancy between the composition of Al_b and Al_{13} , both methods have confirmed that PACI-E contains high contents of Al_{13} exceeding 60% of total Al concentration, and the PACI- Al_{13} possesses about 96 % Al_{13} with a little amount of Al_u . Other studies also have indicated that Al_{13} can be roughly represented by Al_b (Parker and Bertsch, 1992; Liu et al., 1999; Shi et al., 2007). With increasing the contents of polymeric Al, the ratio of Al_{13}/Al_b closes to 1, as indicated in **Table 4.1**, and there are more Al_{13} amounts in PACI prepared at higher γ , as evidenced in **Fig. 4.1**. Therefore, the Ferron method can be used to estimate the Al speciation of various PACI coagulants in further studies.

Table 4.1 Characteristics of coagulants by Ferron assay and ^{27}Al -NMR methods

Coagulant	Al_T (M)	$^*\gamma$	pH	Ferron assay (Al %)			^{27}Al -NMR (Al %)			ratio
				Al_a	Al_b	Al_c	Al_m	Al_{13}	Al_u	$\text{Al}_{13}/\text{Al}_b$
PACl-C	0.04	1.4	3.8	42.3	8	49.7	38.4	6.8	54.8	0.85
PACl-E	0.04	2.1	4.06	19	65.8	15.2	16.6	60	23.4	0.91
PACl- Al_{13}	0.05		4.7	3.7	96.3	0	0	95.8	4.2	0.99

$^*\gamma$: [OH/Al] ratio

**Fig. 4.1** ^{27}Al -NMR spectra of (a) PACl-C (b) PACl-E (c) PACl- Al_{13} .

4.1.2 Effects of pH on Turbidity Removal

The coagulant dosages for 50 NTU turbidity water coagulated by PACl-C, PACl-E and PACl-Al₁₃ are held at 1 mg/L, which are applied subsequently in the jar tests to evaluate the optimum pH of coagulation for turbidity removal. The changes of residual turbidity along with zeta potentials during coagulation at various pH values are shown in **Fig. 4.2**. A marked difference between the coagulation by three coagulants is observed. For PACl-C coagulation, the efficient pH region ranges from 7 to 10. The pH for the optimum turbidity removal coincides with the pH at which the zeta potential closes to zero. The efficient turbidity removal also occurs at pH 7.5 and pH 9, where the zeta potential of particles is around 10 mV and -20 mV, respectively.

For PACl-E coagulation, the optimum turbidity removal has been obtained when the pH is at around 9 where the zeta potential closes to zero, which is due to charge neutralization. However, the turbidity removal is also obviously effective when pH is higher than 10 where the relatively negative zeta potential is found, which implies the particles could be destabilized by electrostatic patch. Similarly, the efficient turbidity removal for PACl-Al₁₃ coagulation also occurs when pH is higher than 9. Since the coagulation performance is directly affected by the effective Al species, the effects of pH on coagulation can be explained by its effects on the transformation of Al species.

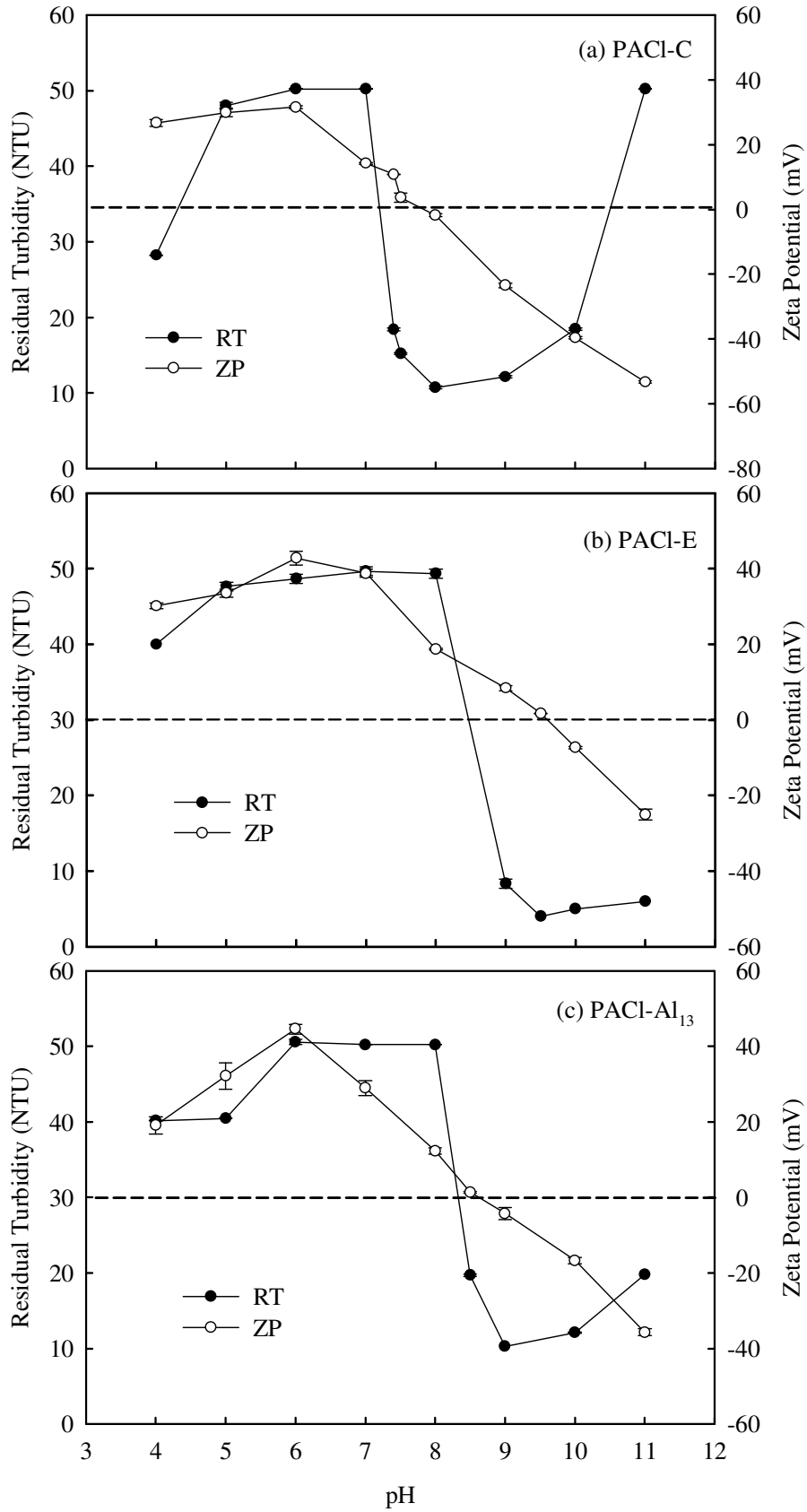


Fig. 4.2 The residual turbidity and the zeta potential for (a) PACI-C (7% Al₁₃) (b) PACI-E (60% Al₁₃) and (c) PACI-Al₁₃ (96% Al₁₃) coagulation at various pH values and 1mg/L as Al.

4.1.3 Effects of pH on Al Speciation in Coagulation

Al speciation of PACl-C, PACl-E and PACl- Al_{13} at various pH values, as measured by Ferron assay, is shown in **Fig. 4.3**, respectively. For PACl-C, the Al_a drops sharply in the range of pH 4 to 5. Very little monomeric Al is detected at neutral pH, but concentrations then rise rapidly at higher pH. The disappearance of Al_a at neutral pH is compensated by the rise in Al_b and Al_c , in which the Al_c is substantially more than Al_b . By contrast, pH has little effect on any of the three species of PACl-E. The most dramatic observation is that the Al_a of PACl-E stays very low, especially at neutral pH, while the Al_b content is quite high, ranging from 60 to 70%. Only a little Al_a of PACl-E transforms into Al_b at neutral pH. In addition, Al_c content of PACl-E decreases slightly in the basic pH region. Likewise, PACl- Al_{13} intrinsically remains the extremely high Al_b content at acidic pH except that very little Al_b transforms into Al_a at alkaline pH as a result of dissolution of Al_{13} .

Study has indicated that a discrepancy between the stability of the Al_b species pre-formed before the dosing and those formed in-situ after dosing, suggesting different Al_b structures (Wang et al., 2004). Although the maximum Al_b is observed at neutral pH for PACl-C, the in-situ formed Al_b species is metastable, and thus probably transforms into Al_c or another Al species immediately after dosing (Hu et al., 2006). By contrast, the pre-hydrolyzed Al_b in PACl-E as well as PACl- Al_{13} remains more stable with varying pH except the content of Al_b slightly drops down when pH is higher than 8. With the increase in pH, the Al_{13} becomes unstable, and thus the Al_{13} transforms into other larger Al species such as Al_{13} aggregates or precipitates at alkaline pH (Van Benschoten and Edzwald, 1990). However, the Al_{13} aggregates could not be identified clearly by Ferron method. Thus, the amount of Al_b could not reflect the real stability of Al_{13} at alkaline pH.

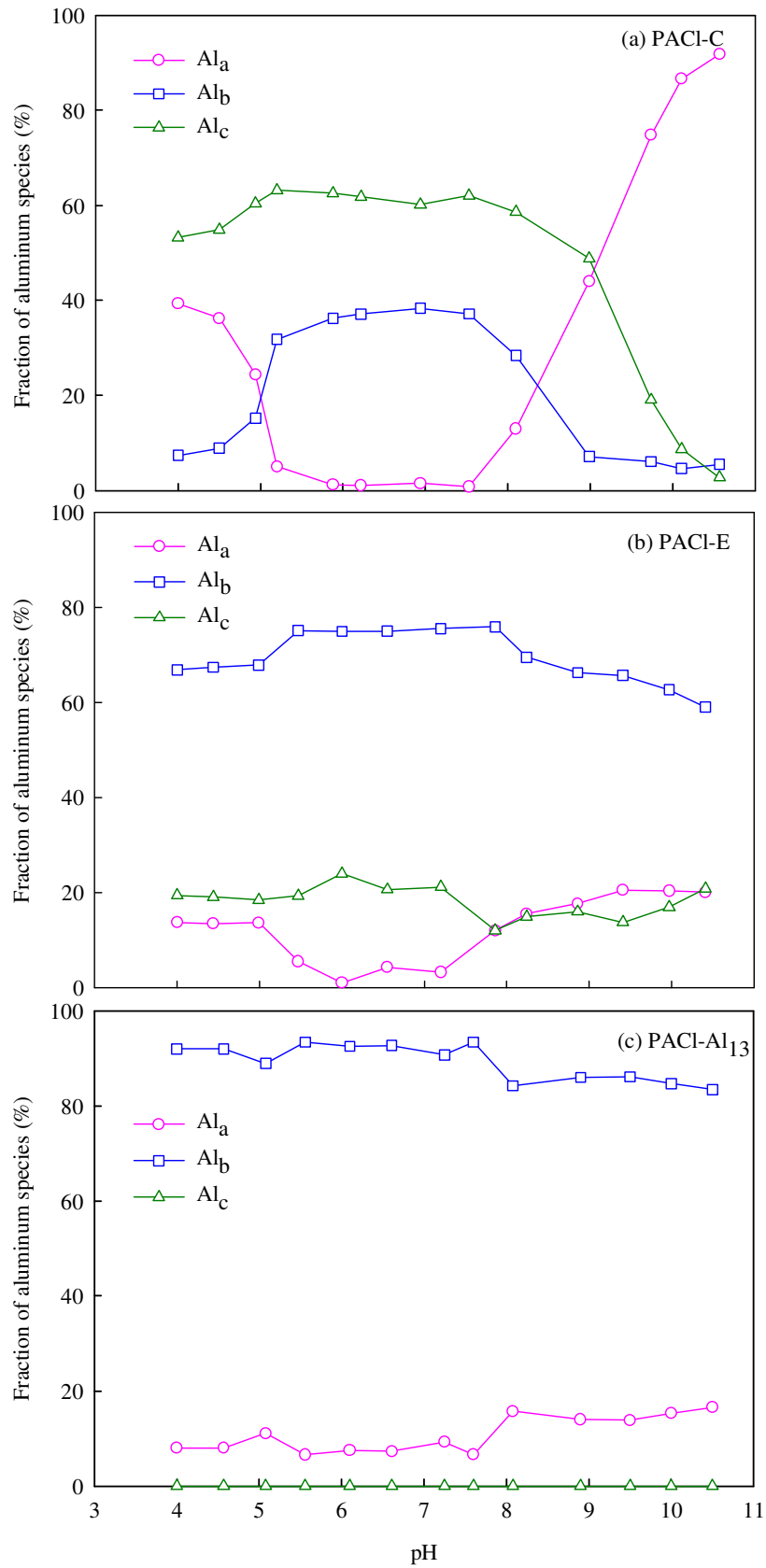


Fig. 4.3 Al speciation of (a) PACI-C (b) PACI-E (c) PACI-Al₁₃ at various pH values under the concentration of 2×10^{-4} mol Al/L.

4.1.4 Effects of Al Speciation on Particle Destabilization Mechanisms

Previous studies have indicated that Al(III) species can transform into voluminous amorphous aluminum hydroxide ($\text{Al}(\text{OH})_{3(\text{am})}$) at neutral pH (Duan and Gregory, 2003; Van Benschoten and Edzwald, 1990). Large amounts of Al_c formed at neutral pH for PACI-C, indicating the formation of significant amount of aluminum hydroxide ($\text{Al}(\text{OH})_{3(\text{am})}$ and colloidal $\text{Al}(\text{OH})_{3(\text{s})}$), and consequently the occurrence of precipitation. In addition, because the in-situ formed Al_b that occurs at neutral pH can quickly transform into Al_c , Al_c dominate over PACI-C coagulation at neutral pH. As a result, enmeshment or sweep flocculation by aluminum hydroxide is responsible for the turbidity removal by PACI-C at neutral pH, even though the charge reversal of particles occurs at such condition, as seen in **Fig. 4.2 (a)**. At alkaline pH, the particles could be destabilized by electrostatic patch of $\text{Al}(\text{OH})_3$ precipitates due to adsorption of precipitates, and then the growth of flocs is formed through precipitation charge neutralization (Dentel, 1988; Ye et al., 2007). Therefore, the particles are destabilized effectively at alkaline pH even though the zeta potential of particles is negative. However, the positive charge of aluminum hydroxide precipitates becomes gradually neutralized with increasing pH, and then the influence of electrostatic patch lessens, which results in the increase of residual turbidity with pH.

Because the Al_b content remains relatively stable throughout the entire pH range studied, as shown in **Fig. 4.3 (b)**, the PACI-E containing more than 60% Al_{13} of total Al concentration, indicating the PACI-E has strong charge neutralization ability, most likely destabilize particles predominately by charge neutralization. Thus, the particles can be rapidly restabilized at low pH, while still keep coagulation efficient at high pH. Meanwhile, the similar results are found for PACI- Al_{13} coagulation at pH

10. On the other hand, the coagulation efficiency of PACI-E is superior to that of PACI-C when pH is higher than 10 where the zeta potential is rather negative, which implies the more particles are favorably destabilized by electrostatic patch. Since Al_{13} favors aggregation when pH is over 6 (Furrer et al., 1992), Al_{13} aggregates are thus easily formed at high alkaline pH at which the Al_{13} molecules are mainly absorbed onto the isolated regions of particles with negative surface charge and then could further restructure and aggregate to form Al_{13} aggregates (Ye et al., 2007). At such condition, some regional charge heterogeneity can occur, which results in electrostatic patch as polymer flocculation (Gregory, 1973). As a result, PACI-E coagulation could be favorable for particle destabilization at alkaline pH to form larger flocs by electrostatic patch with larger Al_{13} aggregates, resulting in more efficient turbidity removal. In the case of PACI- Al_{13} coagulation, the tendency of changes in the zeta potentials and residual turbidity is similar to PACI-E coagulation; however, the coagulation efficiency of PACI- Al_{13} is worse, which is ascribed to higher negative zeta potential of particles that results in the stronger repulsion among particles coagulated by PACI- Al_{13} , as indicated in **Fig. 4.2 (c)**. This impedes the occurrence of sufficient particles destabilization and aggregation.

4.2 Effects of Dosage on Coagulation Efficiency

The dosage of coagulant can influence the amounts of hydrolyzed Al species adsorbed onto the surface of particles and the conformation of hydrolyzed polymeric Al species adhered to the surface of particles; as a consequence, the destabilization mechanism induced by polymeric species are affected (Zhou and Franks, 2006). PACI-C favors enmeshment or sweep flocculation at neutral pH, and in order to testify whether Al_{13} aggregates formed at alkaline pH are able to cause other mechanisms such as interparticle bridging in addition to electrostatic patch as high dosage of PACI-E and PACI- Al_{13} is applied. The effects of dosage on the efficiency of particle destabilization were evaluated at pH 7.5 for PACI-C coagulation and pH 10 for PACI-E and PACI- Al_{13} coagulation, respectively.

4.2.1 Effects of Dosage on Particle Destabilization

The changes in the residual turbidity and zeta potential with dosage during coagulation are illustrated in **Fig. 4.4**. For PACI-C coagulation, as shown in **Fig. 4.4 (a)**, the removal of turbidity increases with dosage, which accompanies the increasing zeta potentials. The efficient turbidity removal is still found at high dosage, even though the charge reversal of particles takes place, which is attributed to the occurrence of enmeshment or sweep flocculation that is considered to be not affected by repulsion between particles.

By contrast, the turbidity decreases rapidly after the addition of PACI-E as well as PACI- Al_{13} at pH 10, and then reaches a minimum. The magnitude of the negative zeta potential sharply decreases with dosage at low dosage (< 2 mg/L), while the negative zeta potential nearly levels off, and approaches to zero when the dosage is higher than 8 mg/L where the coagulant dosage reaches the plateau of adsorption, as

shown in **Fig. 4.4 (b) and Fig. 4.4 (c)**. The plateau of almost zero zeta potential implies that the charge neutralization ability of Al_{13} is reduced. Wu et al. (2007) have indicated that highly positively charged Al_{13} adsorbs onto the surface of particles by monolayer adsorption. Then, the saturation of surface coverage occurs rapidly and the retabilization of particles is due to the strong repulsion between polycations. However, the destabilized particles with zero zeta potential at high dosage are still found in this study, which could be ascribed to the low charge neutralization ability of Al_{13} aggregates (Bottero et al., 1987; Bertsch, 1987).

Al_{13} , which has a +7 valence, could be modified by deprotonation that release the protons in pairs and yield the weakly positively charged Al_{13} such as Al_{13}^{5+} , Al_{13}^{3+} and Al_{13}^{+} while pH is raised, and the aggregation and precipitation of Al_{13} occurs above pH 6, at which the charge of aggregated Al_{13} became weak (Furrer et al., 1992). In addition, the size and the electrophoretic mobility of Al_{13} aggregates principally vary with pH of solution and the concentration of Al_{13} (Furrer et al., 1999; Dubbin and Sposito, 2005). Although Rakotonarivo et al. (1988) have addressed that Al_{13} aggregates formed at various Al concentrations almost have zero surface charge at pH 8, Al_{13} aggregates may form at alkaline pH and still have certain charge neutralization ability to cause efficient coagulation (Chen et al., 2006). This is due to the fact that Al_{13} aggregates formed at different concentration of Al_{13} and pH values responds to their different neutralization charge ability.

As shown in **Fig. 4.5**, the zeta potential of Al species for PACl- Al_{13} coagulation without kaolin particles at pH 10 is around zero and almost insensitive to dosage, which implies that the Al_{13} aggregates with nearly zero surface charge formed at alkaline pH and high dosage for PACl-E and PACl- Al_{13} coagulation could not cause the strong charge neutralization. However, different concentrations of Al_{13} applied

can influence the formation rate of Al_{13} aggregates in kaolin suspension. Because Al_{13} require time to form Al_{13} aggregates, the weakly positively charged Al_{13} may form at pH 10 and low dosage before the formation of Al_{13} aggregates and then be adsorbed rapidly onto particles to neutralize their partial negative charge. At high dosage, because the formation of Al_{13} aggregates is faster, almost neutrally charged Al_{13} aggregates can quickly cloud the particles by adsorption, which leads to nearly zero zeta potential of the particles, even though the dosage is continuously increased. This demonstrates that at alkaline pH the different coagulation mechanisms could be induced by PACl-E and PACl- Al_{13} at low and high dosage, respectively.



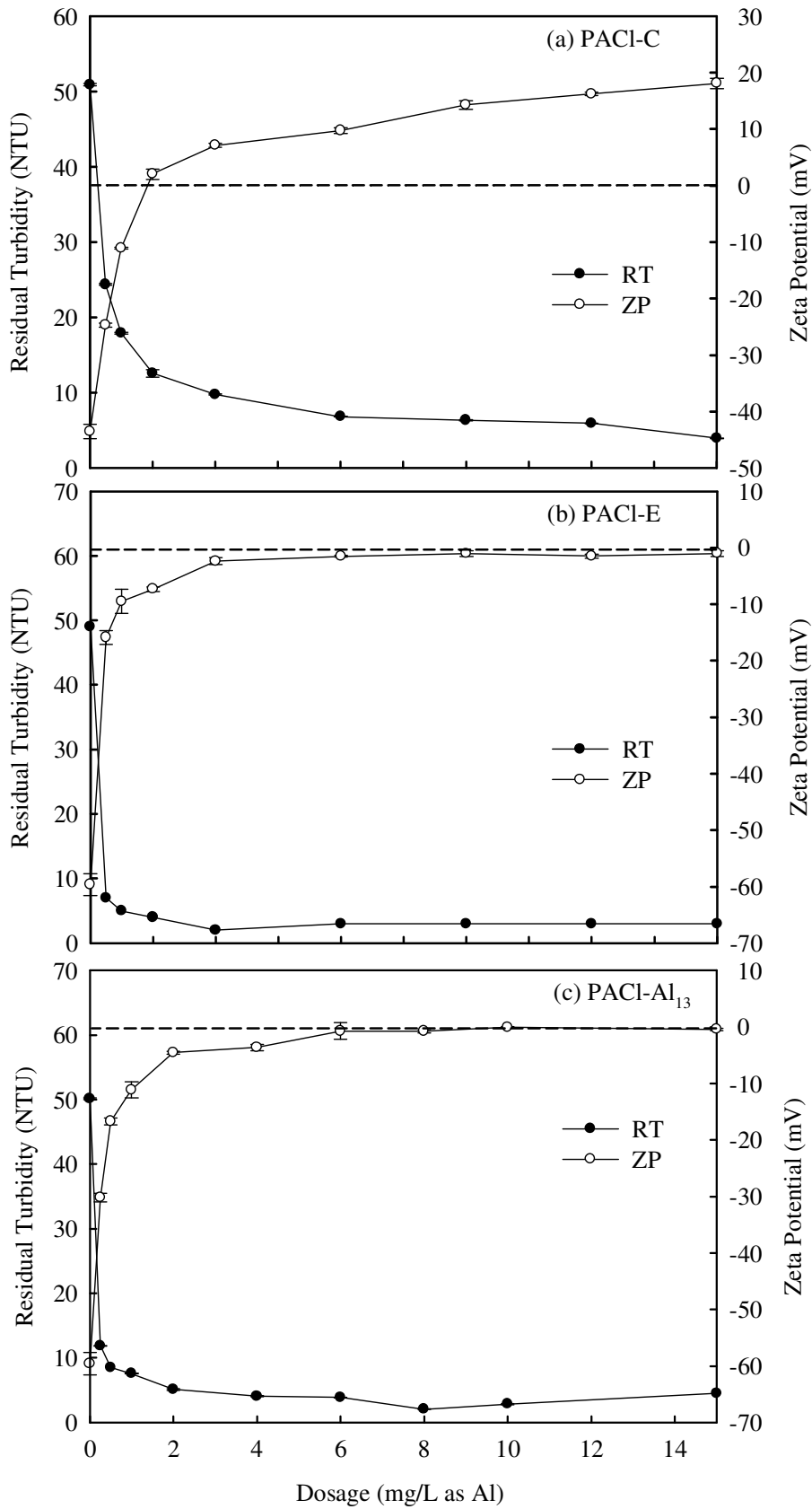


Fig. 4.4 Dosage effects on the residual turbidity and the zeta potential for (a) PACI-C (7% Al₁₃) coagulation at pH 7.5 (b) PACI-E (60% Al₁₃) and (c) PACI-Al₁₃ (96% Al₁₃) coagulation at pH 10.

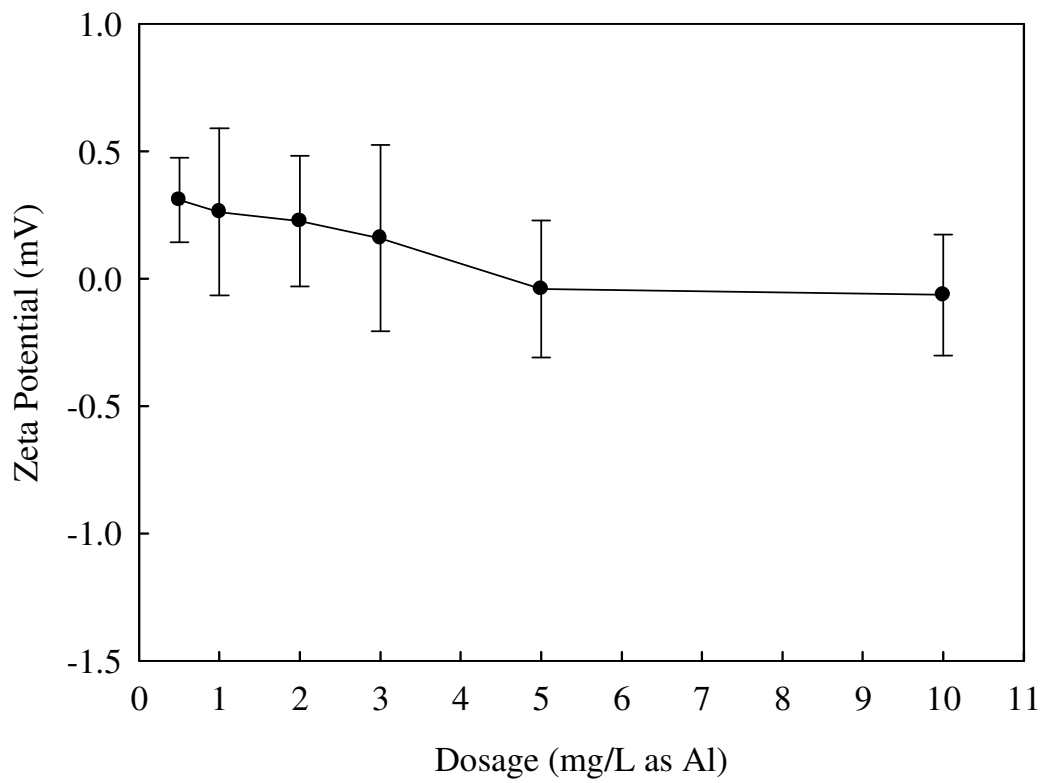
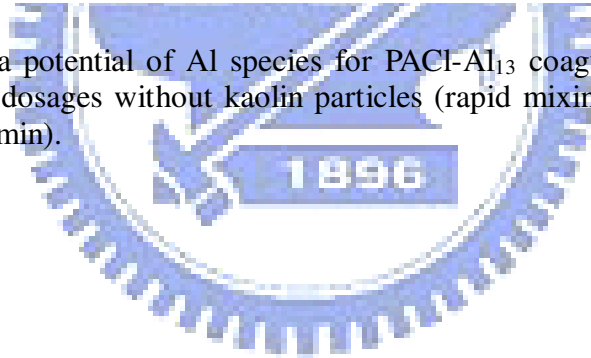


Fig. 4.5 The zeta potential of Al species for PACl-Al₁₃ coagulation at pH 10 and various dosages without kaolin particles (rapid mixing: 200 rpm; reaction time: 1 min).



4.2.2 Reactive Al Species of Floccs

In order to further verify that the predominant coagulation mechanism of three coagulants, the solid-state ^{27}Al -NMR was used to identify the Al speciation within the floccs. **Fig. 4.6** shows the ^{27}Al -NMR spectra of floccs coagulated by PACI-C at neutral pH and by PACI-E as well as PACI- Al_{13} at pH 10 at various dosages. An intensive peak at 0 ppm is found within PACI-C floccs, while a weak peak at 33 ppm is only observed when the dosage is increased. On the other hand, the spectra for PACI-E floccs formed at 8 mg/L exhibits two distinct resonances at about 0 ppm and 63 ppm, whereas the spectra for PACI-E and PACI- Al_{13} floccs formed at 1 mg/L displays one prominent resonance at 0 ppm and very weak resonance at 63 ppm.

The symmetric peak appears at 0 ppm corresponds to octahedrally coordinated aluminum and the peak occurs at 63 ppm corresponds to tetrahedral aluminum (Bottero et al., 1980). The 33 ppm signal of PACI-C floccs, indicating a five-coordinate Al, is attributed to the process of freeze-drying of sediments (Wood et al., 1990). Only the octahedral aluminum is found in PACI-C floccs even at high dosage, which suggests enmeshment or sweep flocculation plays an important role for PACI-C coagulation at neutral pH. For PACI-E and PACI- Al_{13} coagulation, because of the weaker surface charge of Al_{13} at alkaline pH, less Al_{13} could react with the negatively charged kaolin particles, which leads to the unobvious 63 ppm signal. However, the unambiguous resonance at 63 ppm is detected when the dosage of coagulant increases, which could be attributed to the aggregation of the Al_{13} . At high dosage, more and larger Al_{13} aggregates form and adsorb onto the particles, resulting in PACI-E and PACI- Al_{13} floccs with extensive characteristic resonance of Al_{13} . Since the central AlO_4 is almost unreactive when the aggregation of Al_{13} occurs (Phillips et al., 2000), the 63 ppm signal remains intensive even though the

aggregated Al_{13} is formed. Although previous studies have proved that the signal at around 62 ppm is still obtained from solid-state ^{27}Al -NMR experiments of Al precipitates formed at high $[\text{OH}^-]/[\text{Al}]$ ratio (Bottero et al., 1980; Bottero et al., 1987; Furrer et al., 2002), the conditions of preparation such as concentration of total Al and $[\text{OH}^-]/[\text{Al}]$ ratio could significantly affect the characteristics of Al species, including noncrystalline and crystalline Al species. At different conditions, the noncrystalline and crystalline Al species may show the same chemical properties, but differ in particle size and reactive surface. The results of Al species distribution in coagulation suggests that the flocs formation by PACl-C coagulation at neutral pH relies on $\text{Al}(\text{OH})_3$ precipitates regardless of dosage applied, while Al_{13} and Al_{13} aggregates are the predominant species to interact with kaolin particles for PACl-E and PACl- Al_{13} coagulation at alkaline pH.



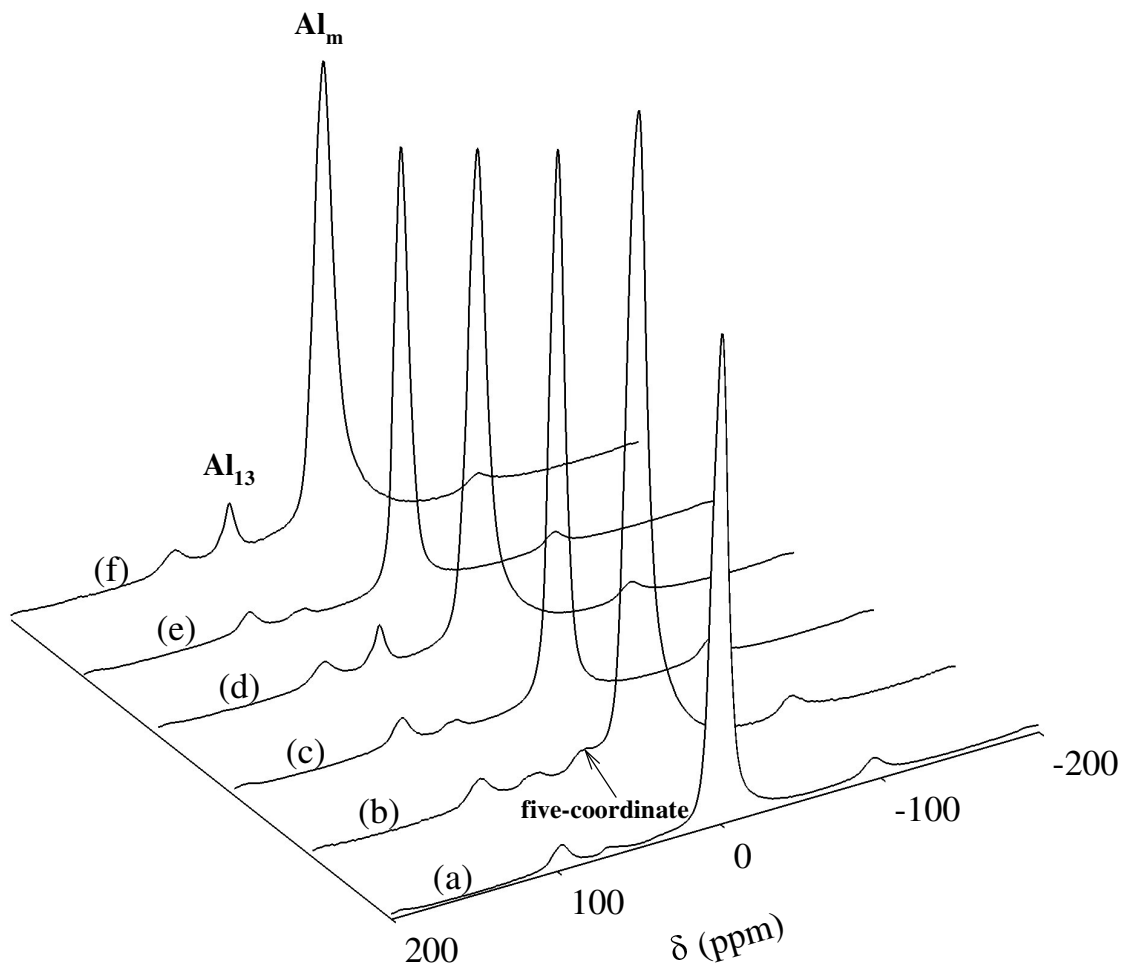


Fig. 4.6 Solid-state ^{27}Al MAS-NMR spectra of freeze-dried kaolin flocs coagulated by three coagulants at various dosages. PACl-C:(a) 1 mg/L (b) 8 mg/L; PACl-E:(c) 1 mg/L (d) 8 mg/L; PACl- Al_{13} :(e) 1 mg/L (f) 8 mg/L

4.3 Summary

The major Al species of PACI-C are monomeric and colloidal Al, while the majority of Al species in PACI-E and PACI-Al₁₃ is Al_b (i.e., Al₁₃), especially for PACI-Al₁₃ that contains more than 95% Al₁₃ of total Al concentration. It is found that Al₁₃ can be roughly represented by Al_b. PACI-C responds to pH differs from PACI-E as well as PACI-Al₁₃. Large amounts of Al_c form at neutral pH for PACI-C, while the pre-hydrolyzed Al_b in PACI-E as well as PACI-Al₁₃ remains more stable with varying pH except alkaline pH. The flocs formation by PACI-C coagulation at neutral pH relies on Al(OH)₃ precipitates regardless of the dosage applied. In addition, either electrostatic patch or interparticle bridging induced by Al₁₃ aggregates may be responsible for particle destabilization and aggregation for PACI-E and PACI-Al₁₃ coagulation at alkaline pH, depending on the dosage. At low dosage, the partially neutralized particles by electrostatic patch are easier to occur for PACI-E and PACI-Al₁₃ coagulation at alkaline pH. Contrary to low dosage, the plateau of most zero zeta potential occurs even though high dosage is applied. At such condition, more and larger Al₁₃ aggregates could form at such condition and adsorb onto the surface of kaolin particles, which could increase the opportunities of interparticle bridging. Accordingly, the interparticle bridging may play more important role in particle destabilization and aggregation when sufficient and large Al₁₃ aggregates form.

CHAPTER V

FORMATION AND STRUCTURE OF FRACTAL FLOCS INDUCED BY VARIOUS DESTABILIZATION MECHANISMS

Coagulation mechanisms could significantly affect the dynamics of particle aggregation and dominate the aggregates size and structure. The interactions of the hydrolyzed Al species with particles during coagulation in water are contributed by different coagulation mechanisms, which thereafter affect the aggregation dynamics of particles and the structure of flocs (Van Benschoten and Edzwald, 1990; Licskó, 1997). Research has demonstrated that charge neutralization induced by PACl can bring more rapid particle aggregation than enmeshment induced by alum (Matsui et al., 1998), and the flocs induced by charge neutralization become more compact that resist shear stress (McCurdy et al., 2004). Coagulation dynamics of various destabilization mechanisms and the properties of resulting flocs such as size and fractal dimension were investigated by SASLS. The morphology of flocs induced by various destabilization mechanisms were observed by WSEM. On the other hand, the morphology of Al_{13} aggregates molecules was scanned by TM-AFM in liquid environment. The proposed destabilization mechanisms and particles aggregation modes for coagulation by various PACl coagulants are also presented in this section.

5.1 Dynamic Growth of Al-Flocs

The growth profile of the flocs for PACl-C coagulation at neutral pH, PACl-E and PACl-Al₁₃ coagulation at alkaline pH, as shown in **Fig. 5.1**, where the floc size is presented by the median equivalent diameter (d_{50}). There marked differences between the growth trends of PACl-C flocs (sweep flocs), PACl-E and PACl-Al₁₃ flocs. As shown in **Fig. 5.1 (a)**, the growth rate of the PACl-C flocs raises with dosage. More particles are destabilized throughout efficient collisions when the dosage is increased, which leads to abrupt increase of the aggregation rate at the initial aggregation. The most dramatic observation is that, at high dosage (8 mg/L) the floc size sharply increases at the initial aggregation and then reaches a maximum, but decreases gradually over time, which could be explained by the breakage of flocs.

It has been accepted that the growth of flocs depends on a balance between the formation and breakage of flocs (Biggs and Lant, 2000; Ducoste and Clark, 1998). Moreover, the aggregates size during coagulation is limited by local physical-chemical conditions such as dosage of coagulant or shear-induced mixing. During the rapid initial formation of flocs, the flocculation of primary flocs dominates the evolution of particles size, then the influence of breakage increases as floc size increases until a steady-state size is approached. As the largest flocs form, the number of the primary particles will decrease to a minimum before the steady-state flocs is reached, which results in the significant decrease of collision rate as well as the increase in breakage rate. With PACl-C coagulation, the more dosage is applied, the larger the sweep flocs that contain large porosity and then are easily broken by surface erosion of eddies splitting (i.e., large-scale fragment) that is dependent of flocs structure (Jarvis et al., 2005). Consequently, the breakage rate of the sweep flocs at high PACl dosage is faster. Because the breakage of flocs is relatively

obvious at high dosage where the d_{50} size of flocs decrease from 450 μm to 350 μm , the possible breakage mode is surface erosion resulting in an increase in the small particle size ranges.

For PACI-E coagulation, the size of flocs also increases with dosage, and the equilibrium d_{50} size of flocs coagulated with various dosages remains 300 μm to 400 μm , as illustrated in **Fig. 5.1 (b)**. At the same low dosage (1 mg/L), the d_{50} size of flocs coagulated by PACI-E is much larger than that by PACI-C in response to electrostatic patch induced with Al_{13} aggregates. Meanwhile, since PACI-C coagulation favors enmeshment, larger sweep flocs formed at high dosage are observed as a result of the occurrence of abundant $\text{Al}(\text{OH})_3$ precipitates. However, the initial growth of PACI-E flocs is more rapid than that of sweep flocs at various dosages studied. Enmeshment is generally slower than other coagulation mechanisms because $\text{Al}(\text{OH})_3$ precipitates require a few seconds to form in coagulation (Letterman et al., 1973). Therefore, PACI-E coagulation that favors charge neutralization (or electrostatic patch) can give faster particle coagulation. In addition, the size of PACI-E flocs formed at 8 mg/L also decreases over time, but the breakage rate of them is slower than that of sweep flocs. This suggests that PACI-E flocs possess a stronger resistance to shear stress due to stronger attractive forces between particles within PACI-E flocs under charge neutralization. Out of the minor decrease in floc size for PACI-E coagulation at high dosage, the breakage mode is inferred to be large-scale fragmentation that is the cleavage of flocs into several pieces of a size similar to parent flocs (Jarvis et al., 2005).

In the case of PACI- Al_{13} coagulation, the d_{50} of PACI- Al_{13} flocs increases with increasing dosage and ranges from 200 μm to 250 μm with dosage used, as presented in **Fig. 5.1 (c)**. The d_{50} size of PACI- Al_{13} flocs formed at the 8 mg/L slowly

decreases with the flocculation time, similar to PACI-E coagulation. However, the PACI- Al_{13} coagulation has a higher breakage rate of flocs at such condition, which implies that PACI-E flocs are stronger than PACI- Al_{13} flocs.

The results of coagulation dynamics show that the dosage of PACI strongly affects the balance between efficient collision and the breakage of the flocs. The magnitude of flocs breakage during coagulation is well correlated with destabilization mechanisms. Therefore, the structure of flocs will be dependent of the dosage of coagulants as well as the predominant destabilization mechanisms.



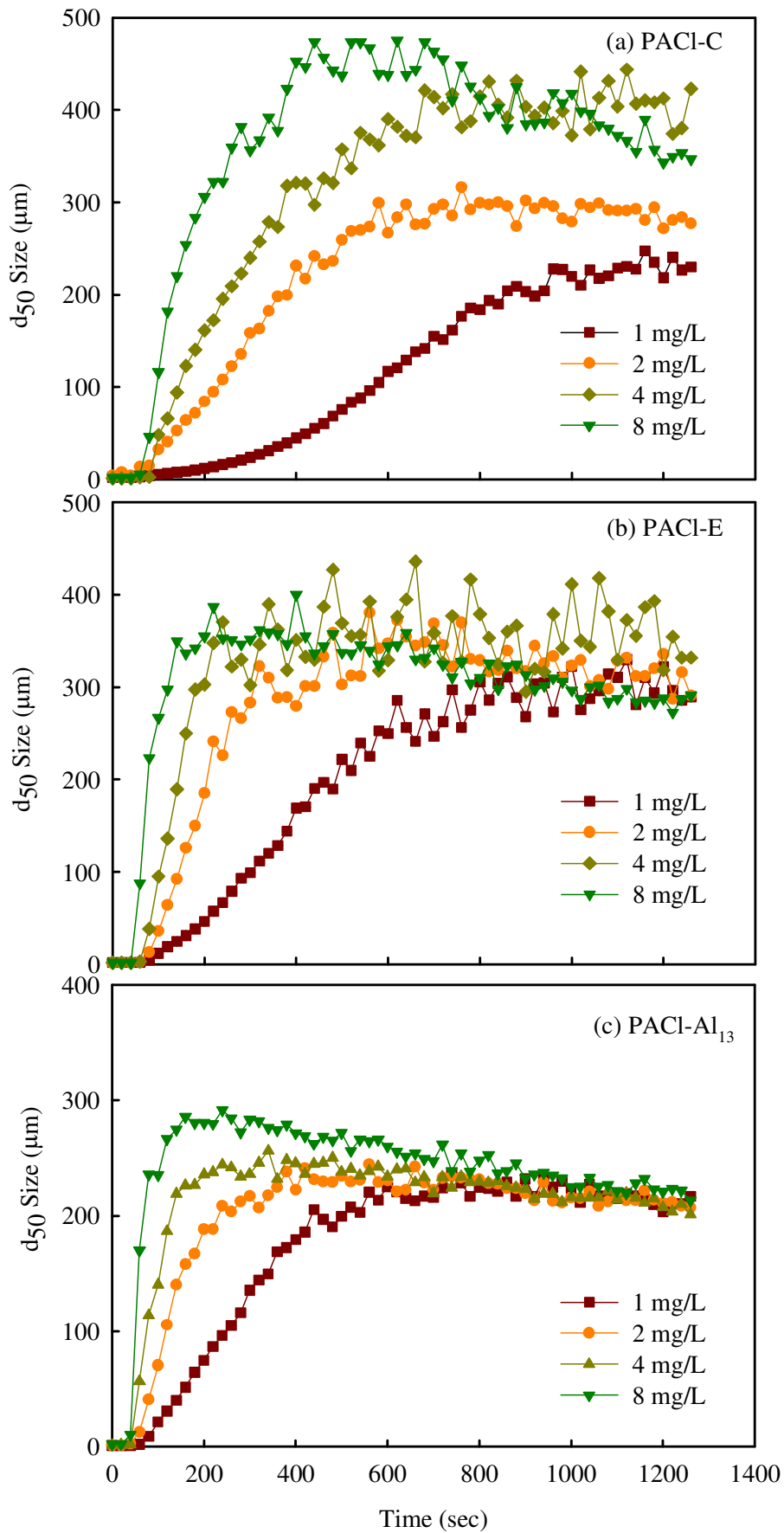


Fig. 5.1 The particle aggregation dynamics induced by (a) PACI-C coagulation at pH 7.5 and (b) PACI-E and (c) PACI- Al_{13} coagulation at pH 10.

5.2 Fractal Structure of Al-Flocs

The concept of fractal geometry has been applied successfully in the illustration of colloidal aggregation dynamics. Flocs formed by coagulation in water and wastewater treatment are considered to be the fractal structure (Thomas et al., 1999). Fractal structure of flocs is subject to the process of flocs growth, involving particle aggregation and the breakage of flocs, which results in the change of fractal structure. Many studies have proved that the structure of alum-kaolin flocs is correlated to floc size (Francois, 1987; Francois, 1988; Chakraborti et al., 2003). The following experiments were performed to understand the relationship between floc size and fractal structure for coagulation by various PACl coagulants.

5.2.1 Effects of Dynamic Growth of Floc on Fractal Structure

The mean size and fractal dimension (D_s) of the flocs formed by PACl-C, PACl-E and PACl- Al_{13} coagulation at various dosages are presented in **Fig. 5.2**. For PACl-C coagulation, the mean size and D_s of sweep flocs increase with dosage except for at the high dosage (8 mg/L) where a drop of mean size occurs, as shown in **Fig. 5.2 (a)**. In theory, fractal dimensions do not change as a function of floc size. However, the virtual relationship between fractal dimensions and floc size tremendously hinges on the mode of particle coagulation at various conditions (Chakraborti et al., 2000; Jiang and Logan, 1996). Particle aggregation is dictated by aggregation limiting regimes, including diffusion-limited aggregation (DLA) when there is no repulsive force between the colloidal particles and reaction-limited aggregation (RLA) where additional repulsive forces caused by electrostatic forces or steric interaction prevents the particles from aggregation (Elimelech et al., 1995). The variation of the fractal dimension of kaolin flocs with the change in slow mixing time also can reflect the

regimes of coagulation kinetics (Berka and Rice, 2005).

As shown in **Fig. 4.4 (a)** and **Fig. 5.1 (a)**, the charge reversal of particles occurs when the dosage is higher than 1 mg/L for PACl-C coagulation, but the efficient aggregation and turbidity removal still occurs. Because the shear stress induced by mixing overcomes the repulsion among particles during slow mixing, the particles can aggregate after encounter each other over time, suggesting the PACl-C coagulation at high dosage is governed by RLA. The higher dosage the stronger is the repulsion between particles, which causes low collision efficiency. As a result, particles or clusters need to collide many times before sticking occurs as the increase in dosage, ranging from 2 mg/L to 8 mg/L. This gives more opportunities to explore other configurations, and then particles are able to penetrate into a cluster before encountering another particle and sticking (Lin et al., 1989); as a consequence, more compact flocs are obtained. Furthermore, the breakage of flocs and an increase in the D_s of the sweep flocs coagulated by PACl-C at 8 mg/L simultaneously occur with slow mixing time, as illustrated in **Fig. 5.2 (a)** and **Table 5.1**, indicating the flocs are restructuring during flocs breakage process. Similar studies have reported that a restructuring of primary particles within flocs due to breakage and re-aggregation that occurs in response to ambient shear (Clark and Flora, 1991; Oles, 1992). In this research, the rearrangement of primary particles within flocs can be caused by the breakage of flocs through a longer flocculation time and then are restructured throughout the new balance between the reformation and breakage of flocs with time. This process possibly makes flocs into a denser and more compact structure. Therefore, the D_s values of sweep flocs sharply increase from 2.2 to 2.33 when the breakage of flocs occurs. Contrary to high dosage, the change of the D_s values of sweep flocs formed at 1 mg/L is not obvious with mixing time because restructuring

caused by the breakage of flocs does not happen.

Similar tendency of changes in mean size and fractal dimension of flocs is also found for PACI-E coagulation, as illustrated in **Fig. 5.2 (b)**. PACI-E coagulation favors electrostatic patch at low dosage and charge neutralization at high dosage. With increasing dosage, the more efficient particle coagulation is obtained due to the weaker repulsion among particles that leads to the shorter distance between particles within the flocs and the flocs of higher D_s are thus formed. At high dosage, although the PACI-E flocs experience breakage, as shown in **Fig. 5.1 (b)**, the almost invariant D_s of PACI-E flocs are observed to be in the range from 2.2 to 2.21 during flocs breakage. The change in fractal dimension of PACI-E flocs formed at low dosage is similar to that at high dosage. This demonstrates that a stable structure of flocs is formed because the breakage of PACI-E flocs does not result in the occurrence of interflocs restructuring. It is likely that the PACI-E coagulation at 8 mg/L is induced by charge neutralization at which the nearly zero charged particles can aggregate by DLA. In general, cluster-cluster flocs have fractal dimension values of around 1.8 at DLA and 2.1 at RLA, respectively (Lin et al., 1989). However, the sweep flocs and PACI-E flocs formed at RLA and DLA have higher D_s values around 2.3 and 2.2, which could be assigned to the breakage of flocs resulting particle-cluster aggregation that creates a denser internal structure within flocs.

By contrast, the different observation on the trends of change in mean size and D_s value of PACI- Al_{13} flocs is found when dosage is gradually increased. The mean size and D_s values of the flocs after the addition of PACI- Al_{13} at various dosages are presented in **Fig. 5.2 (c)**. The mean size of PACI- Al_{13} flocs slowly increases with dosage, while the D_s value of PACI- Al_{13} flocs decreases with increasing dosage from 2.18 to 2.03. Evidently, the change in flocs structure with increasing dosage for

PACI- Al_{13} coagulation is contrary to that for PACI-C and PACI-E coagulation. At alkaline pH, although the trends in particle destabilization by PACI- Al_{13} with increasing dosage is similar to PACI-E coagulation, as shown in **Fig. 4.4**, the resulting floc structure is markedly different, meaning that PACI-E and PACI- Al_{13} coagulation at alkaline pH and high dosage are dictated by different destabilization mechanisms. This can be attributed to the potential effect of Al_{13} aggregates on particle coagulation. Because other Al species such as monomeric Al and colloidal Al involves in PACI-E in addition to Al_{13} , the sufficient large Al_{13} aggregates could not generate easily at alkaline pH and high dosage as result of mutual influence between various Al species. At the same condition, because PACI- Al_{13} contains the extremely high content of Al_{13} , which facilitates the aggregation of Al_{13} , the formation of larger Al_{13} aggregates are more rapidly occurred to cause interparticle bridging. As shown in **Table 5.1**, at low dosage, the D_s increases slightly with slow mixing time, while the almost invariable D_s ranging from 2.04 to 2.05 at high dosage where the zero zeta potential is found, which is analogous to that for PACI-E coagulation at high dosage. Studies have suggested that the invariable fractal dimension of flocs represents cluster-cluster aggregation induced by DLA with no reconstruction and rearrangement in shear coagulation by interparticle bridging with polymers (Biggs et al., 2000; Yu et al., 2006). The results suggest that the larger Al_{13} aggregates formed by PACI- Al_{13} coagulation at high dosage could promote particle aggregation via interparticle bridging rather than charge neutralization, even though the zeta potential of destabilized particles are close to almost zero.

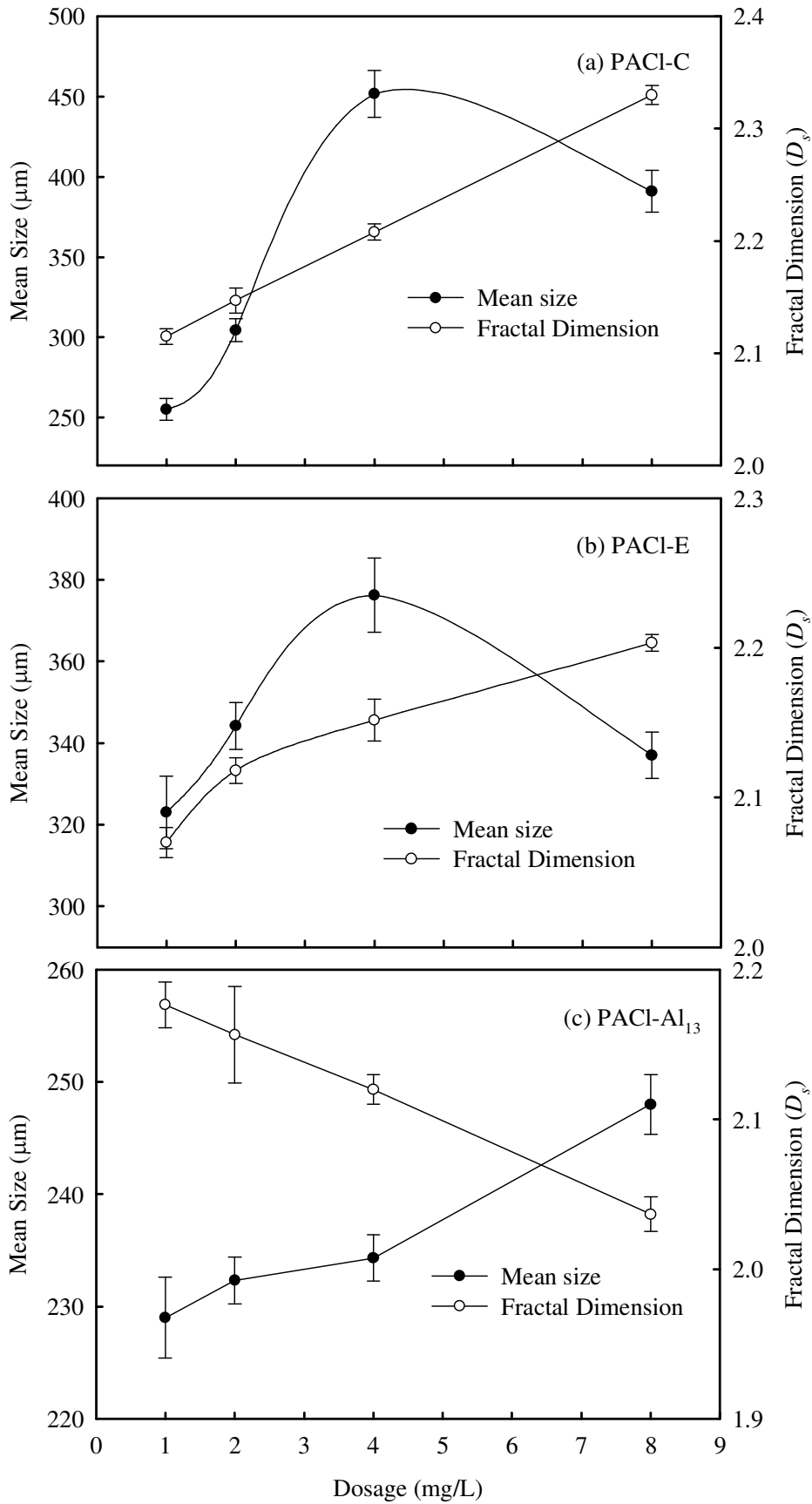


Fig. 5.2 The fractal dimensions (D_s) of flocs coagulated by (a) PACI-C at pH 7.5 and (b) PACI-E and (c) PACI- Al_{13} at pH 10 and various dosages.

Table 5.1 Fractal dimension (D_s) of various flocs during coagulation

Coagulants	Time (min)	*Fractal dimension (D_s)	
		1 mg/L	8 mg/L
PACl-C	10	2.09	2.28
	15	2.11	2.30
	20	2.11	2.33
PACl-E	10	2.06	2.20
	15	2.07	2.21
	20	2.08	2.21
PACl- Al_{13}	10	2.11	2.04
	15	2.12	2.04
	20	2.14	2.05

* D_s : Mean values of scattering exponent measured by SASLS assay



5.2.2 In-situ Observation on the Morphology of Floccs

In this research, the WSEM is used to observe the morphology and principal structure of primary floccs in the moist condition for the first time in order to further understand the interactions of various Al species and kaolin particles under different coagulation mechanisms induced by PACl-C, PACl-E and PACl-Al₁₃. The WSEM images of floccs coagulated by various PACl coagulants at low and high dosage are given in **Fig. 5.3**. There are marked differences between the sweep floccs formed coagulated by PACl-C at low and high dosage. At low dosage, sweep floccs have some spherical nuclei, but contain many amorphous matters at high dosage, as shown in **Fig. 5.3 (a)** and **Fig. 5.3 (b)**. Because the PACl-C coagulation at neutral pH undergoes enmeshment or sweep flocculation mostly, the particle can be aggregated as sweep floccs by both surface precipitation and adsorption of aluminum hydroxide precipitates on the surface of particles (heterocoagulation) (Chowdhury and Amy, 1991). In enmeshment or sweep flocculation, there are external particles (aluminum hydroxide precipitates), which cloud the surface where the nucleation and growth occurs. Less amorphous hydroxide precipitates can only diffuse onto the particles by shear when low dosage is applied, which results in insufficient nucleation or precipitation charge neutralization induced by colloidal Al(OH)_{3(s)}. By contrast, more amorphous hydroxide precipitates are formed at high dosage and cover the surface of particles, which causes the formation of larger sweep floccs with a rough and ragged contour. However, the opportunities may increase for particle interpenetration during floc breakage because more floc conformations are exposed, which can influence the aggregation modes. The occurrence of particle-cluster aggregation will become relatively easier when floccs suffer breakage. As a result, the principal structure of sweep floccs formed by PACl-C coagulation at 8 mg/L is

more compact than that at 1 mg/L.

As shown in **Fig. 5.3 (c)** and **Fig. 5.3 (d)**, the flocs formed by PACI-E coagulation at 8 mg/L are larger and more compact than that at 1 mg/L. At high dosage, since DLA induced by charge neutralization predominately governs the PACI-E coagulation without structuring of flocs, where the particles attach permanently to other particles at the first contact, PACI-E flocs are possibly formed by cluster-cluster aggregation, as reported by Torres et al. (1991). When the breakage of flocs occurs, the particle-cluster aggregation is likely formed, which results that the edge of the PACI-E flocs is loosely associated but the interior is so densely packed that primary particles is not easily observed. As a result, a larger and higher fractal dimensional PACI-E floc with a smooth and glossy contour is observed at 8 mg/L. Below overdose, since the breakage of PACI-E flocs does not occur, they have a more open structure induced by electrostatic patch in response to cluster-cluster aggregation.

The WSEM micrographics of PACI- Al_{13} flocs formed at low and high dosage are shown in **Fig. 5.3 (e)** and **Fig. 5.3 (f)**. A distinct difference between flocs formed at low and high dosage is found. The flocs formed at low dosage are more compact and smaller, while the flocs formed at high dosage have a looser structure and are larger. At low dosage, weakly charged Al_{13} only can partially neutralize the negatively charged particles by adsorption, which results that many incomplete fully neutralized surfaces of particles are exposed. As a result, the flocs possess a higher fractal dimensional structure potentially due to electrostatic patch. At high dosage, the surface of kaolin particles is saturated with adsorbed Al_{13} aggregates that extend to attach other particles in the interior of PACI- Al_{13} flocs, which leads to looser structure of flocs caused by interparticle bridging. These results of WSEM imaging are in accordance with the observation from SASLS.

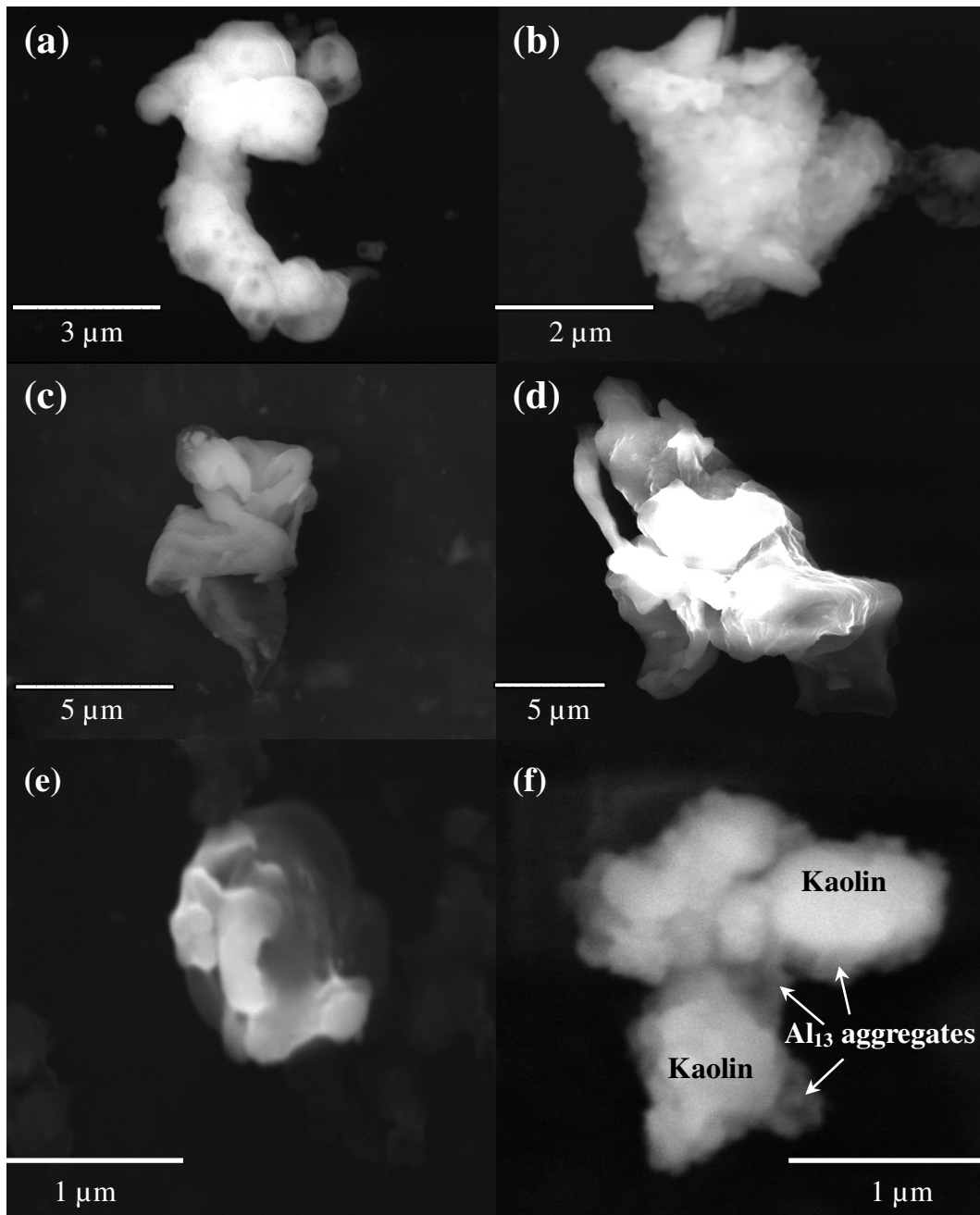


Fig. 5.3 The WSEM micrographics of flocs coagulated at various coagulants and dosages under 1 min rapid mixing followed by 20 min slow mixing. PACI-C: (a) 1mg/L and (b) 8 mg/L; PACI-E: (c) 1 mg/L and (d) 8 mg/L; PACI-Al₁₃: (e) 1 mg/L and (f) 8 mg/L.

5.3 In-situ Observation on the Morphology of Al₁₃ Aggregates

In fact, it is difficult to quantify the Al₁₃ aggregates in coagulation due to the variety of Al₁₃ aggregates size. Study has indicated that the size of Al₁₃ aggregates increase gradually from 570 nm at pH 4.35 to 1200 nm at round pH 6.5 at a given concentration of Al₁₃ (Dubbin and Sposito, 2005). In the past, Al₁₃ molecule of various PACl coagulants has been observed by Hu et al. (2005). TM-AFM was used to observe the morphology of Al₁₃ adsorbed onto the mica in air. The Al₁₃ molecule, however, will condense at such condition. In this study, in-situ observation of the morphology of Al₁₃ aggregates was performed by liquid TM-AFM to provide more evidences for the role of Al₁₃ aggregates in the PACl-Al₁₃ coagulation. The morphology of Al₁₃ aggregates generated during PACl-Al₁₃ coagulation at high dosage (8 mg/L) without suspended kaolin particles in reactor was observed by TM-AFM, as shown in **Fig. 5.4**. At a high dosage, as seen in **Fig. 5.4 (a)**, a few micro-scale linear Al₁₃ aggregates are composed of a chain of small coiled Al₁₃. The various coiled Al₁₃ aggregates are also observed in **Fig. 5.4 (b)**. These single coiled Al₁₃ aggregates are 300 to 400 nm, which is similar to the results of size measurement, as shown in **Fig. 5.5**. Moreover, they are 2 to 3 nm in vertical height. Although study has suggested that the condensation of the nanoclusters into an x-ray amorphous gel that eventually forms bayerite with time (Bradley et al., 1993), the Al₁₃ aggregates formed in our experiments should not further transform into Al(OH)₃ precipitates in such a short period of coagulation. Also, the surfaces of these Al₁₃ aggregates are smoother than amorphous Al(OH)₃ precipitates, as evidenced in **Fig. 5.4 (c)**, and they have coiled contour as well as a flat configuration of 2-3 nm. Thus, the Al₁₃ aggregates formed in this study are certainly not Al(OH)₃ precipitates.

On the other hand, many studies have suggested the formation of Al_{13} aggregates is through the rearrangement of structure with aging (Bertsch et al., 1986a; Kloprogge et al., 1992). However, several researchers have advocated that the deprotonation of Al_{13} is the most possible reason for the self-assembling of Al_{13} (Letterman and Asoleker, 1990; Furrer et al., 1992). In this research, because the reaction time of coagulation is short, the exterior bound water ligands of a single Al_{13} can rapidly deprotonate as pH rises (Phillip et al., 2000), and the exposed surface OH group of the Al_{13} has weaker charge when the dosage is increased at alkaline pH. This leads to the aggregation of defected Al_{13} with high affinity for cation in a coiled structure, as proved in **Fig. 5.5**. Different fractal dimensions imply that Al_{13} in the solution are random self-assembling in different shapes and adsorb onto the surface of the mica. As long as the efficient collision among coiled Al_{13} aggregates formed at sufficient PACI- Al_{13} dosage is achieved, these restructured Al_{13} can easily and quickly aggregate by van der Waals attractive forces. The results echo that the higher fractal dimensional Al_{13} aggregates is attributed to the denser Al_{13} within the Al_{13} aggregates (Axeols et al., 1986). The linear Al_{13} aggregates formed in the alkaline condition has also been proposed by Bottero et al. (1987) in the model calculation on the configuration of aggregated Al_{13} with small angle X-ray scattering (SAXS).

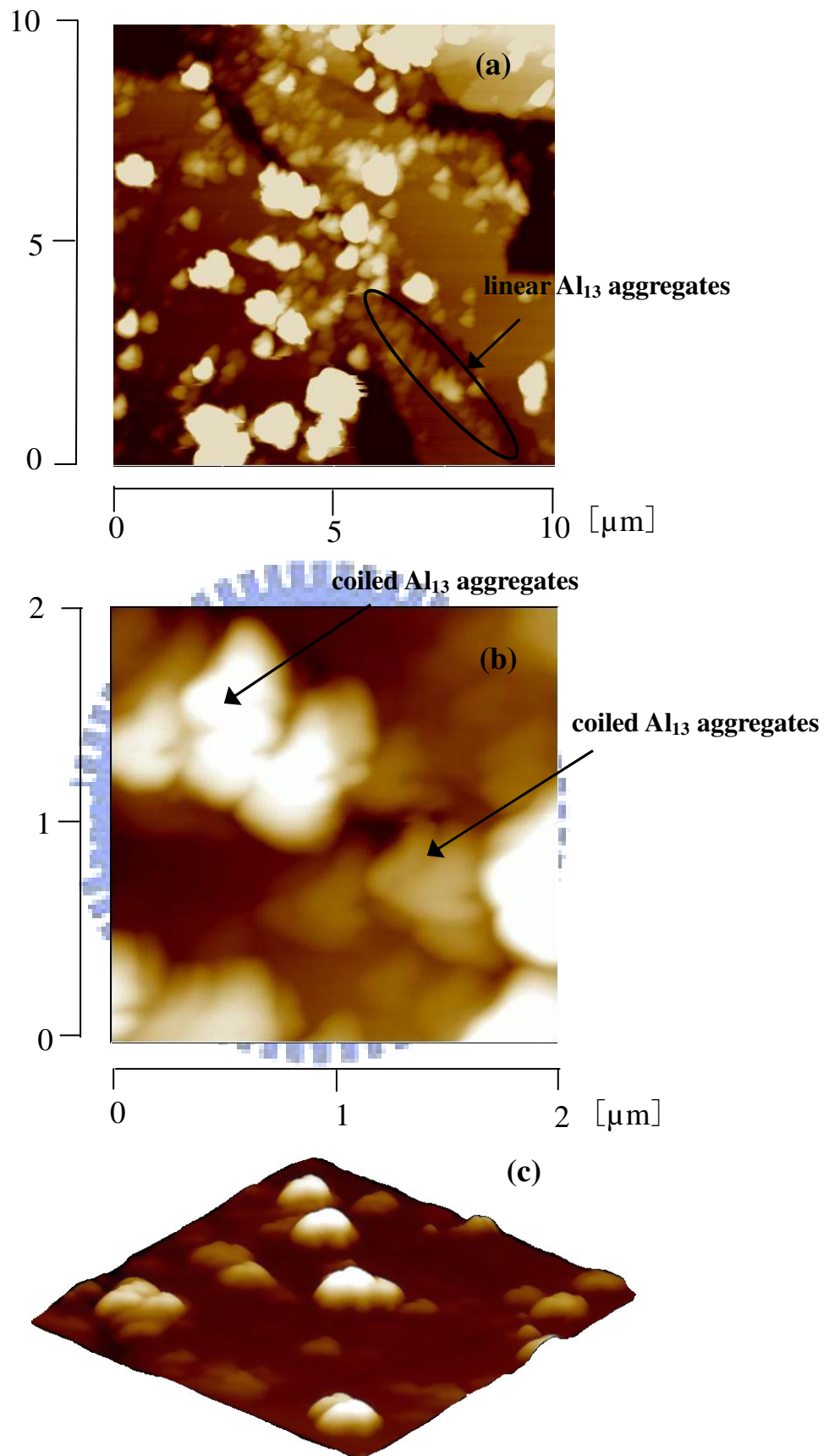


Fig. 5.4 TM-AFM topographic image of the Al_{13} adsorbed on the mica in liquid system for PACl- Al_{13} coagulation at 8 mg/L and pH 10 without kaolin particles. (a) and (b) two-dimension (c) three-dimension.

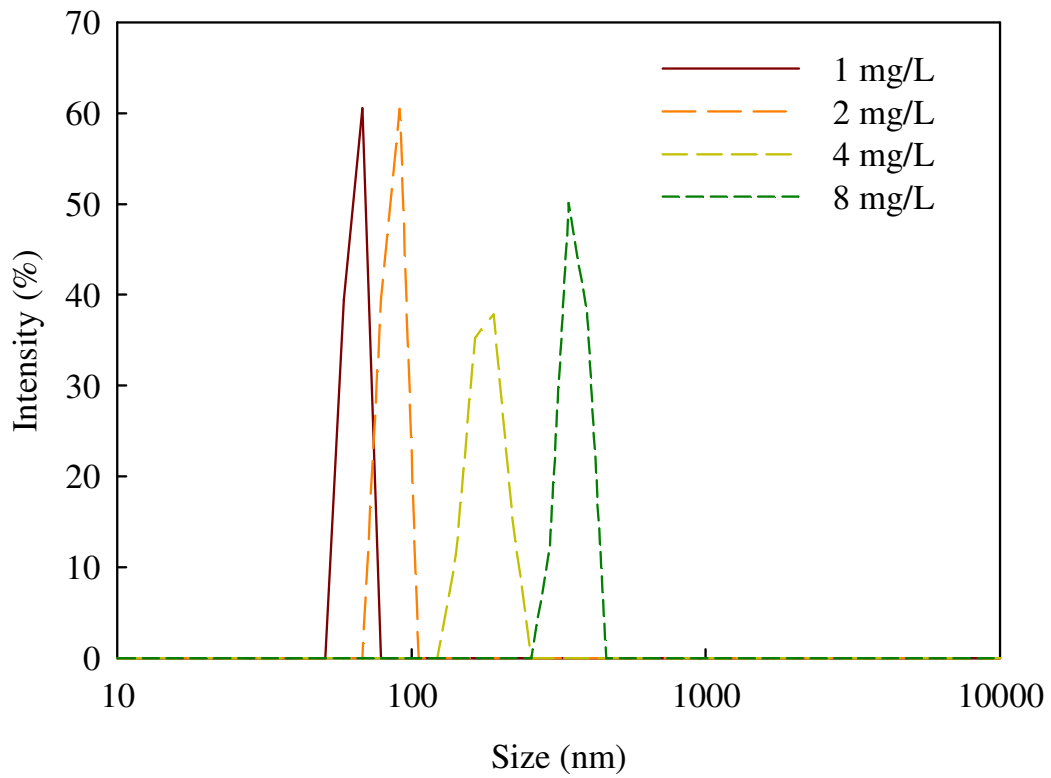
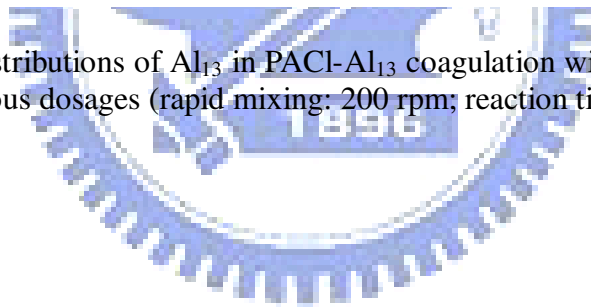


Fig. 5.5 Size distributions of Al₁₃ in PACI-Al₁₃ coagulation without kaolin particles at various dosages (rapid mixing: 200 rpm; reaction time: 1 min).



5.4 Predominant Destabilization Mechanisms Model

Hydrolyzed $\text{Al}(\text{OH})_3$ precipitates are generally considered to destabilize particles by surface precipitation or precipitate charge neutralization through adsorption. However, the size of amorphous aluminum hydroxide formed at such condition depends on dosage, which affects the destabilization efficiency. The schematic representation of the predominant coagulation mechanisms of PACl-C at neutral pH is presented in **Fig. 5.6**. Because the majority of PACl-C is monomeric and colloidal $\text{Al}(\text{OH})_{3(s)}$, sweep flocs are formed at neutral pH by both surface precipitation and adsorption of aluminum hydroxide precipitates on the surface of particles. At neutral pH, as dosage of PACl-C exceeds solubility product, there are external aluminum hydroxide precipitates ($\text{Al}(\text{OH})_{3(\text{am})}$) and colloidal $\text{Al}(\text{OH})_{3(s)}$ that cloud the surface of particles and then the nucleation occurs to entrap particles, resulting in a larger amorphous precipitate that can sufficiently sweep particles from water. At low dosage, smaller and less positively charged aluminum hydroxide precipitates form and are attracted to larger negatively charged particles by precipitation charge neutralization (i.e., heterocoagulation), leading to the formation of smaller flocs that is unfavorable for particle removal through precipitation.

On the other hand, the coagulation mechanisms of cationic polymers in coagulation of colloidal particles are well known, including charge neutralization, interparticle bridging and electrostatic patch (Gregory, 1973). These mechanisms can happen concurrently and are frequently competing with each other. The coagulant dosage also has influences on the conformation of polymer and consequently the adsorption on the surface of particles, which causes different mechanisms of coagulation (Zhou and Franks, 2006). As a result, the Al_{13} conformation on the surface of particles will change at different PACl- Al_{13} dosage,

inducing different coagulation mechanisms.

For coagulation by PACl-E and PACl- Al_{13} at high alkaline pH, since increasing the dosage accompanies the formation of larger Al_{13} aggregates, the mechanisms between the reaction of Al_{13} aggregates and particles will change correspondingly. However, PACl-E coagulation responds to dosage differs from PACl- Al_{13} coagulation at alkaline pH. The schematic representation of the predominant mechanisms of Al_{13} aggregates is presented in **Fig. 5.7**. For PACl- Al_{13} coagulation, because the larger Al_{13} aggregates could not be easily generated at low dosage via Al_{13} self-assembling, the weakly positively charged Al_{13} may adsorb onto the surface as flattened configuration and then cluster in a region to perform the particle coagulation by electrostatic patch where the partial charge neutralization of particles occurs, which contributes to patched flocs of high D_s . At high dosage, linear Al_{13} aggregates with a given dimension or other dimensional Al_{13} aggregates with neutralized charge can form rapidly via the collisions of coiled Al_{13} aggregates and then adsorb onto the surface of kaolin particle as extended configuration when the surfaces of particles are clouded. Therefore, the extended Al_{13} aggregates adsorbed on particle surface can assemble particles by interparticle bridging, which results in bridged flocs of low D_s . On the other hand, since PACl-E contains certain monomeric and colloidal Al except for Al_{13} , the aggregation of Al_{13} could be postponed by other Al species at alkaline pH, which limits the formation of larger Al_{13} aggregates. Thus, the insufficient large Al_{13} aggregates can not cause interparticle bridging, even though high dosage is applied. As such, PACl-E coagulation at alkaline pH is favorable for electrostatic patch or charge neutralization, which is dependent of dosage applied.

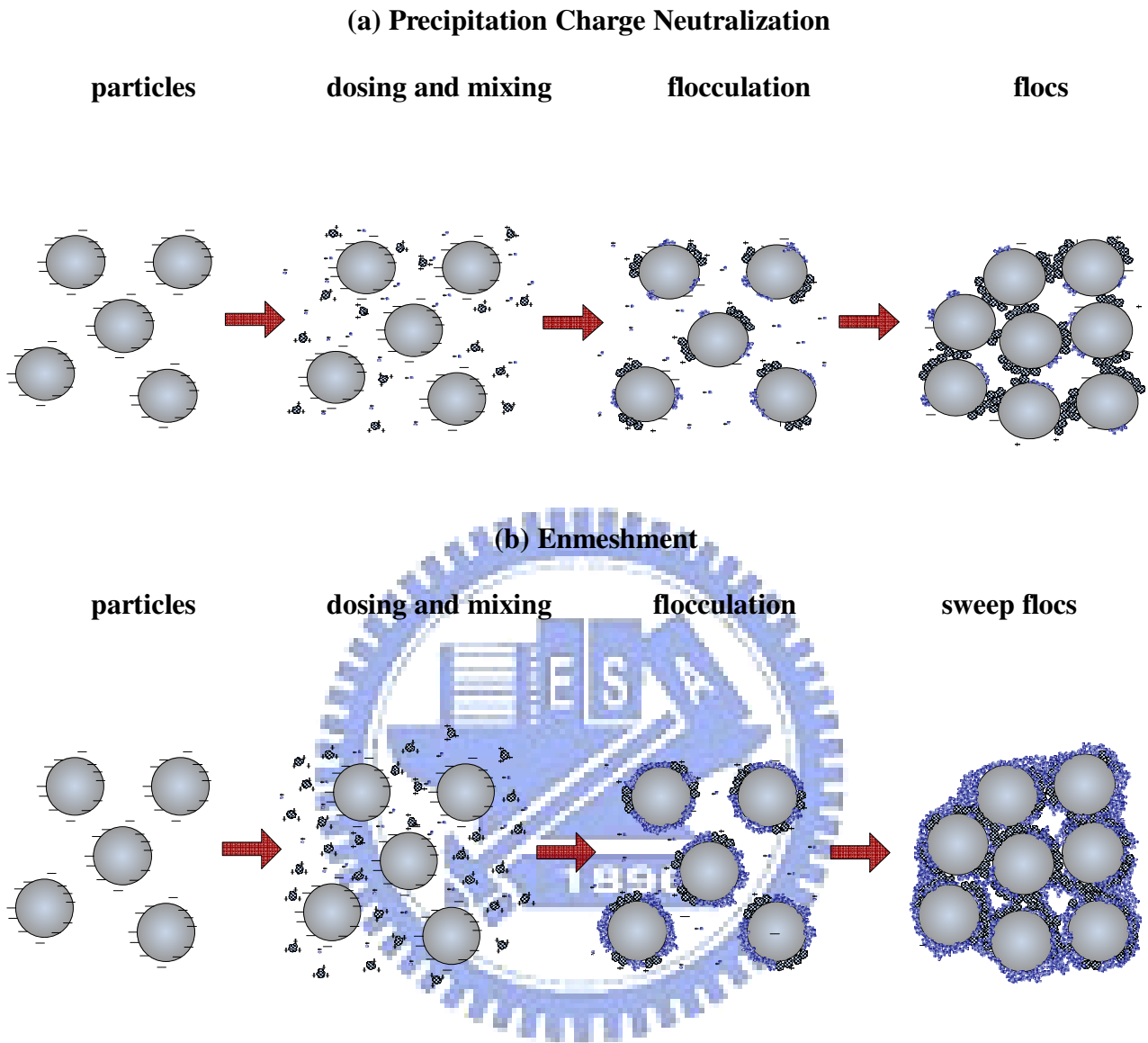
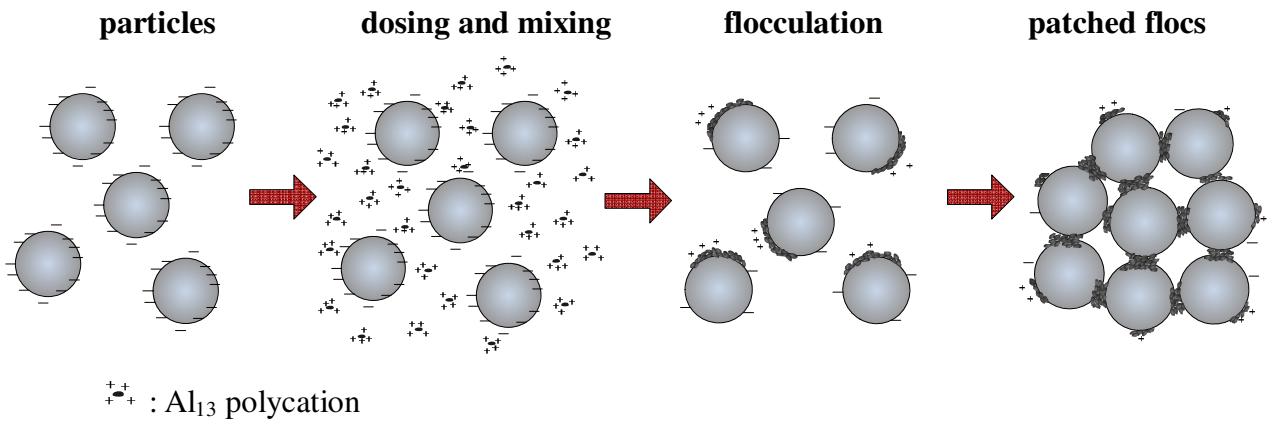


Fig. 5.6 Schematic representation of the destabilization mechanism induced by PACl-C coagulation at neutral pH. (a) Precipitation Charge Neutralization (b) Enmeshment.

(a) Electrostatic Patch



(b) Interparticle Bridging

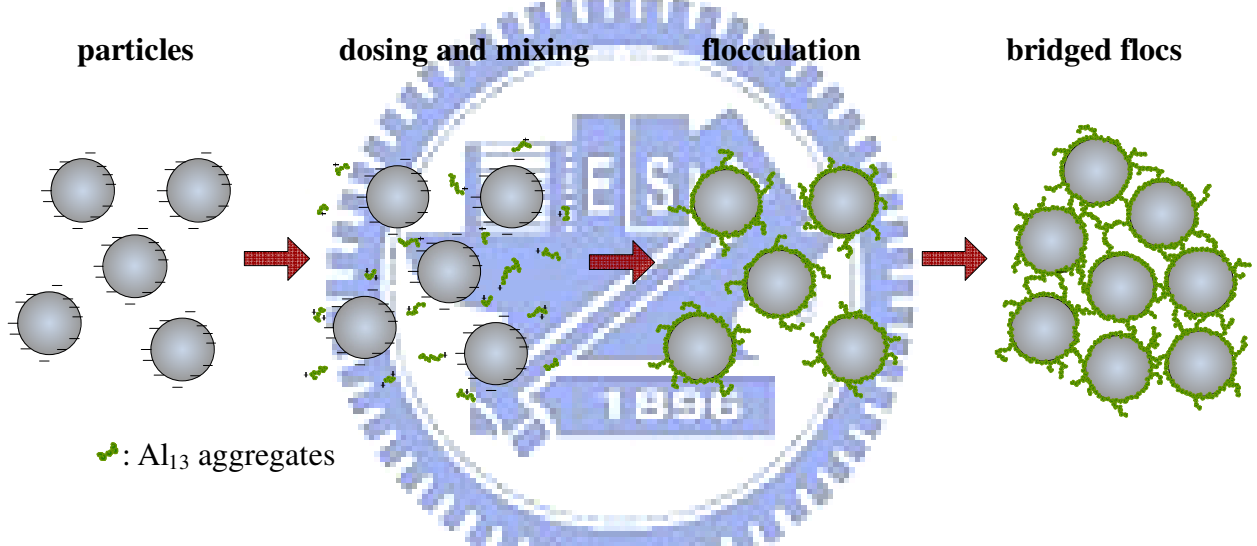


Fig. 5.7 Schematic representation of the destabilization mechanism induced by Al_{13} aggregates. (a) Electrostatic Patch (b) Interparticle Bridging.

5.5 Summary

At neutral pH, the PACI-C with monomeric and colloidal Al species favors enmeshment or sweep flocculation in response to the occurrence of abundant $\text{Al}(\text{OH})_3$ precipitates at high dosage, while precipitate charge neutralization become the major destabilization mechanism at low dosage. By contrast, the PACI-E containing a high percentage of Al_{13} causes either electrostatic patch or charge neutralization mechanisms with Al_{13} aggregates at pH 10. The breakage of flocs induced by enmeshment (or sweep flocculation) and electrostatic patch occur at overdosing. The breakage rate of sweep flocs is faster than that of PACI-E flocs. The structure of sweep flocs formed at RLA becomes denser with dosage, in which the breakage of sweep flocs can cause the increase in fractal dimension of flocs. At DLA, PACI-E flocs formed by electrostatic patch become more compact with dosage and have a stronger resistance to shear stress during coagulation.

PACI- Al_{13} coagulation induced by electrostatic patch is responsible for particle destabilization at low dosage and pH 10, which results in the higher fractal dimensional flocs. Interparticle bridging becomes the major mechanism when the sufficient high dosage is applied due to the formation of Al_{13} aggregates with nearly zero charge, which leads to flocs of low fractal dimension. The PACI- Al_{13} flocs formed by interparticle bridging are more easily broken during coagulation processes by shear stress. On the other hand, enmeshment or sweep flocculation causes sweep flocs with a rough and ragged contour, while electrostatic patch or charge neutralization induces flocs with a smooth and glossy surface. Interparticle bridging brings about PACI- Al_{13} flocs of a looser structure with a fluffy contour. At such condition, some larger linear Al_{13} aggregates composed of a chain of coiled Al_{13} and several coiled Al_{13} aggregates with different dimensions are found.

CHAPTER VI

SURFACE Al COMPOSITION OF Al(OH)₃-RICH AND Al₁₃-AGGREGATE FLOCS

For coagulation by Al-based coagulants, it is essential to realize the distribution of various Al species on the surface of flocs, which can reflect the reactions between predominant hydrolyzed Al species and particles. By using an X-ray photoelectron spectroscopy (XPS) that has been applied to quantify surface Al composition of various solid materials (Duong et al., 2005; Kloprogge et al., 1999), the interactions between various hydrolyzed Al species and particles during PACl coagulation can be further identified. Although Al₁₃ molecules can aggregate and eventually transform into Al(OH)₃ precipitates with time, the composition and structure of Al₁₃ aggregates differs from Al(OH)₃. The following experiments were carried out to differentiate the properties of Al(OH)₃-rich and Al₁₃-aggregate flocs to further understand the difference of Al(OH)₃ precipitates and Al₁₃ aggregates.

Based on the results of previous study, the flocs formed by PACl-C coagulation at neutral pH and PACl-Al₁₃ coagulation at pH 10 under 8 mg/L are considered to be Al(OH)₃-rich and Al₁₃-aggregate flocs. To realize the predominant Al species on the surface of these flocs, their surface characteristics were examined by various surface analysis technology. The SEM as well as HR-TEM was used to observe the morphology of various PACl-kaolin flocs. The HR-XRD was also employed to examine the crystalline structure of these flocs. The WSEM was employed to inspect the formation of Al(OH)₃ precipitates. In addition, the XPS was applied to identify the quantity of octahedral Al (Al^{VI}) and tetrahedral Al (Al^{IV}) on the surface of various PACl-kaolin flocs.

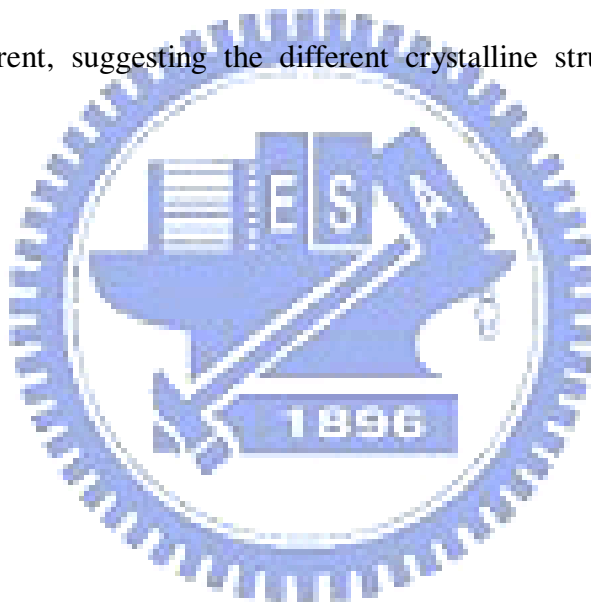
6.1 Structure of Al-Flocs

In coagulation, the structure of flocs provides the advantageous information for the understanding of the interaction between coagulant and particles. In general, coagulated flocs have a multilevel structure (Wu et al., 2002). In fact, coagulation by different Al-based coagulants results in different structures of Al-flocs due to the effect of hydrolyzed Al species on the surface structure of Al-flocs. In addition, the crystalline structure of Al-flocs also can reflect the characteristics of reactive species in coagulation. In this study, the $\text{Al}(\text{OH})_3$ -rich flocs are formed by various Al species, while the crystalline structure of Al_{13} -aggregate flocs is under investigation. The following observation on surface and crystalline structure of these Al-flocs were performed by SEM as well as HR-XRD to further explore their structure.

6.1.1 Surface structure of Flocs

Surface structure of flocs is related to their morphology. **Fig. 6.1** exhibits that the morphology of $\text{Al}(\text{OH})_3$ -rich and Al_{13} -aggregate flocs, respectively. As shown in **Fig. 6.1 (a)**, the larger $\text{Al}(\text{OH})_3$ -rich flocs are clearly observed. Their inner structure are compact but the porous and looser structure is visible in their edge where several colloids with the size of around $2\ \mu\text{m}$ are found, as seen in **Fig. 6.1 (b)**, which is assigned to a large number of colloidal Al in PACI-C. The results of EDX analysis indicate that these colloids are rich in Al element, suggesting $\text{Al}(\text{OH})_{3(s)}$ are certainly adsorbed onto the particles. This also strongly substantiates the occurrence of particle-cluster aggregation for PACI-C coagulation at neutral pH. By contrast, the Al_{13} -aggregate flocs are smaller, as shown in **Fig. 6.1 (c)**. Close-up examination of this image reveals a network of strips which are composed of NaCl crystal, as illustrated in **Fig. 6.1 (d)**. Furthermore, the nano-scale $\text{Al}(\text{OH})_{3(am)}$ surrounding the

edge of $\text{Al}(\text{OH})_3$ -rich flocs is found through HR-TEM observation, as illustrated in **Fig. 6.2 (a)**, which proves that surface precipitation or the adsorption of hydrolyzed $\text{Al}(\text{OH})_{3(\text{am})}$ precipitates onto the surface of the kaolin particles occurs for PACl-C coagulation at neutral pH and high dosage. There has no other apparent crystalline structure within the Al_{13} -aggregate flocs, as shown in **Fig. 6.2 (b)**. Because PACl- Al_{13} coagulation was conducted at high dosage and alkaline pH, the Al_{13} aggregates most likely cloud the surface of kaolin so that the polygonal crystals (i.e., kaolin crystals) are not observed. The SEM and HR-TEM observation of flocs indicate that the surface morphology of $\text{Al}(\text{OH})_3$ -rich and Al_{13} -aggregate flocs are significantly different, suggesting the different crystalline structure exist in these flocs.



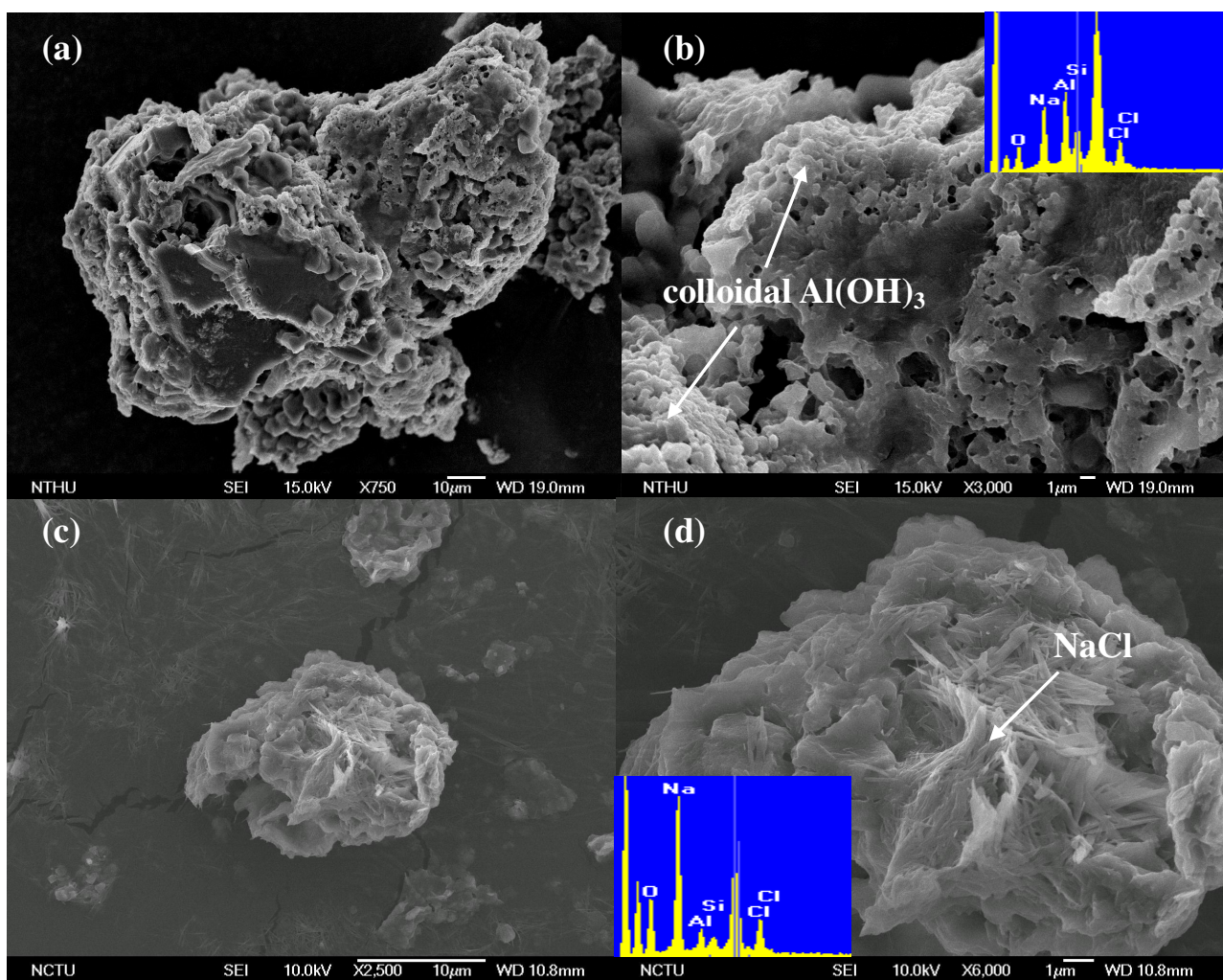


Fig. 6.1 SEM micrographics of Al(OH)₃-rich and Al₁₃-aggregate floes formed by PACI-C and PACI-Al₁₃ coagulation at 8 mg/L as Al.

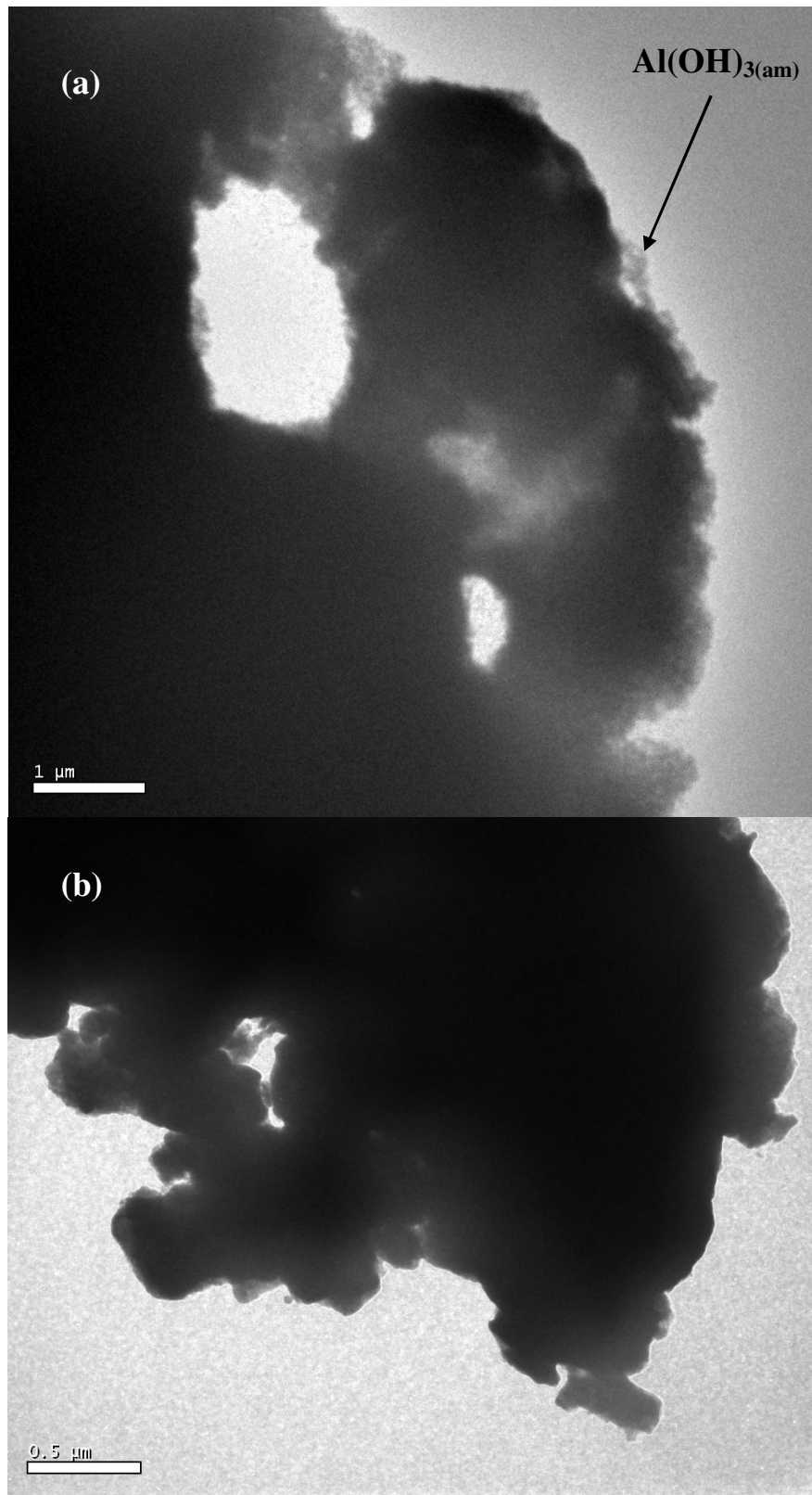


Fig. 6.2 HR-TEM images of (a) Al(OH)_3 -rich and (b) Al_{13} -aggregate flocs formed by PACl-C and PACl- Al_{13} coagulation at 8 mg/L as Al.

6.1.2 Crystalline Structure of Floccs

To further verify the possibility that other specific crystal Al species adsorbed on the surface of the $\text{Al}(\text{OH})_3$ -rich and Al_{13} -aggregate floccs, these floccs were examined by HR-XRD. The HR-XRD patterns of $\text{Al}(\text{OH})_3$ -rich and Al_{13} -aggregate floccs are depicted in **Fig. 6.3**. To discriminate the Al crystal from kaolin particle, the kaolin powder was also determined by XRD. **Fig. 6.3 (a)** shows two extensive peaks occur at about 12° and 24° for the kaolin samples. By contrast, $\text{Al}(\text{OH})_3$ -rich floccs do not have well-formed crystalline structures compare to the kaolin crystals, as shown in **Fig. 6.3 (b)**. For $\text{Al}(\text{OH})_3$ -rich floccs, the signal of $\text{Al}(\text{OH})_{3(\text{am})}$ or colloidal $\text{Al}(\text{OH})_{3(\text{s})}$ is broad and ranges from 18° to 25° , which is in good agreement with the characteristic spectrum of aluminum hydroxide in the Joint Committee on Powder Diffraction Standards (JCPDS) database. On the other hand, because the kaolin suspension contains certain amount of NaOCl_4 , the presence of square or threadlike NaCl crystals on the surface of flocc, as seen in **Fig. 6.1 (d)**, results in the crystalline signal between 20° and 30° (Linnow et al., 2007). Likewise, the peak of NaCl crystals is also acquired for the Al_{13} -aggregate floccs, as shown in **Fig. 6.3 (c)**, in addition to the occurrence of a weak signal at around 8° , which can be assigned to Al_{13} -like crystalline structure (Cheng and Chou, 2000). Out of high stability of internal tetrahedral Al (AlO_4) within Al_{13} (Phillips et al., 2000), the Al_{13} aggregates formed through the bridging of deprotonated octahedral Al may keep Al_{13} -like structure (Akitt, 1989). The results of HR-XRD scanning suggest that the crystalline structure of Al_{13} aggregates differs from that of $\text{Al}(\text{OH})_3$.

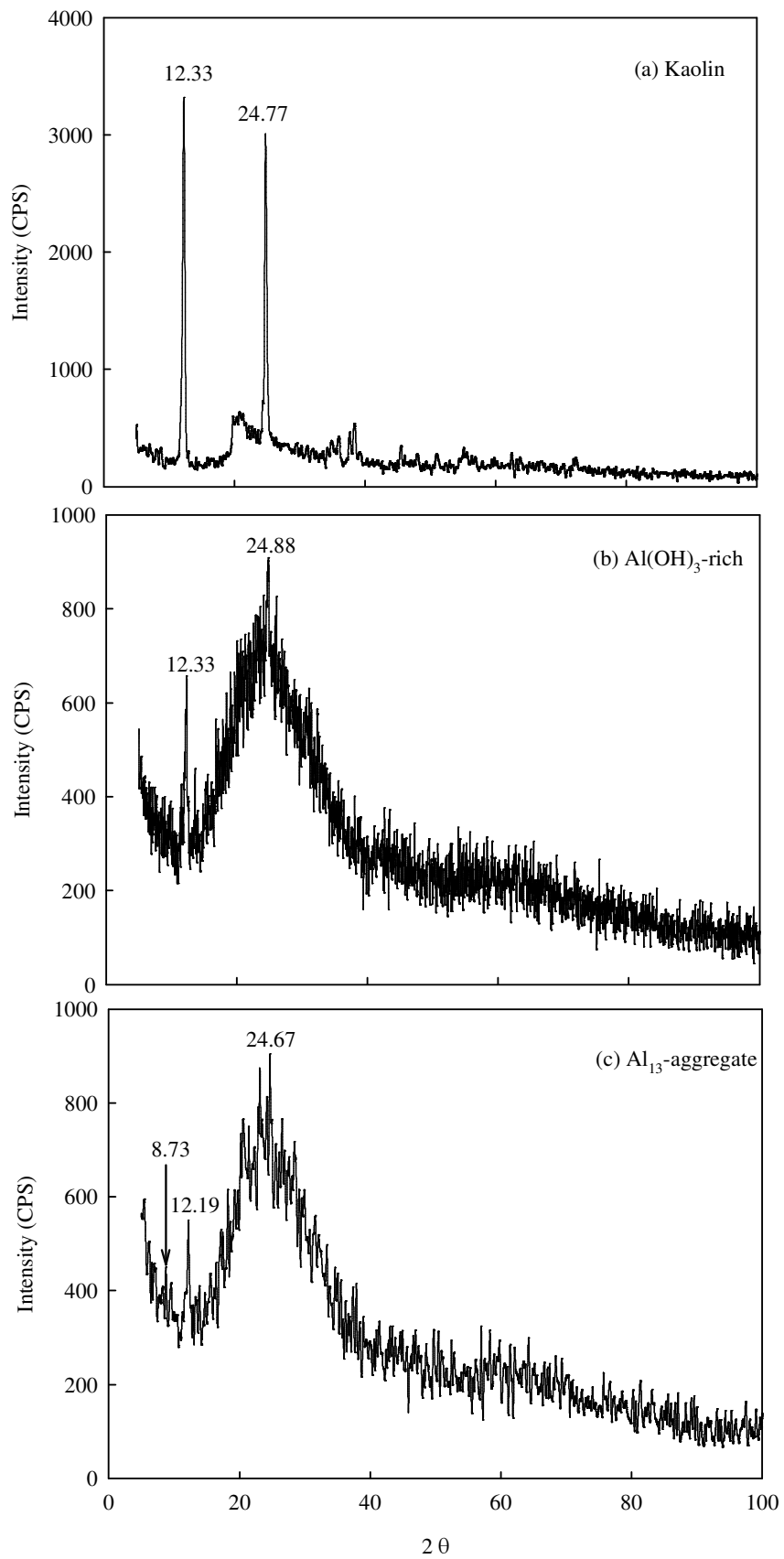


Fig. 6.3 HR-XRD patterns of (a) Kaolin powder (b) Al(OH)_3 -rich and (c) Al_{13} -aggregate flocs.

6.2 In-situ Observation of Al(OH)₃ Precipitates

Al(OH)₃ precipitates possess various types and shapes in liquid with aging. Because PACI-C coagulation favors the formation of Al(OH)₃ precipitates, presumably the surface Al composition of Al(OH)₃-rich flocs depends on the types of the Al(OH)₃ precipitates adsorbed on the surface of kaolin particles. As shown in **Fig. 6.1 (b)** and **Fig. 6.2 (a)**, two types of Al(OH)₃ precipitates are markedly observed. In order to in-situ identify the Al(OH)₃ precipitates clearly, the PACI-C coagulation was carried out at neutral pH and high dosage (8 mg/L) without adding kaolin particles to form abundant Al(OH)₃ precipitates. The WSEM micrographics of Al(OH)₃ precipitates are shown in **Fig. 6.4**. As shown in **Fig. 6.4 (a)**, a considerable number of Al(OH)_{3(am)} form and precipitate after the addition of PACI-C, which is attributed to an enormous amount of colloidal Al(OH)_{3(s)} that are intrinsic to PACI-C. The size of these precipitates is more than 1 μm, and they are obviously sphere-like in shape and rigged, as illustrated in **Fig. 6.4 (b)**. These colloidal Al(OH)_{3(s)} precipitates have a pit on their surface, indicating the colloidal Al(OH)_{3(s)} has a sunken surface. On the other hand, several smaller amorphous Al(OH)₃ precipitates were observed on the surface of the colloidal Al(OH)_{3(s)}. In general, the formation of colloidal Al(OH)_{3(s)} is slower, which increases the opportunity to grow larger nuclei, while Al(OH)_{3(am)} is prone to in-situ formed rapidly by the hydrolysis of Al(III) resulting the smaller and irregular precipitates. The result substantiates that in-situ formed and preformed Al(OH)₃ precipitates are divergent in morphology, which implies the different Al composition are among Al(OH)_{3(am)} and colloidal Al(OH)_{3(s)}.

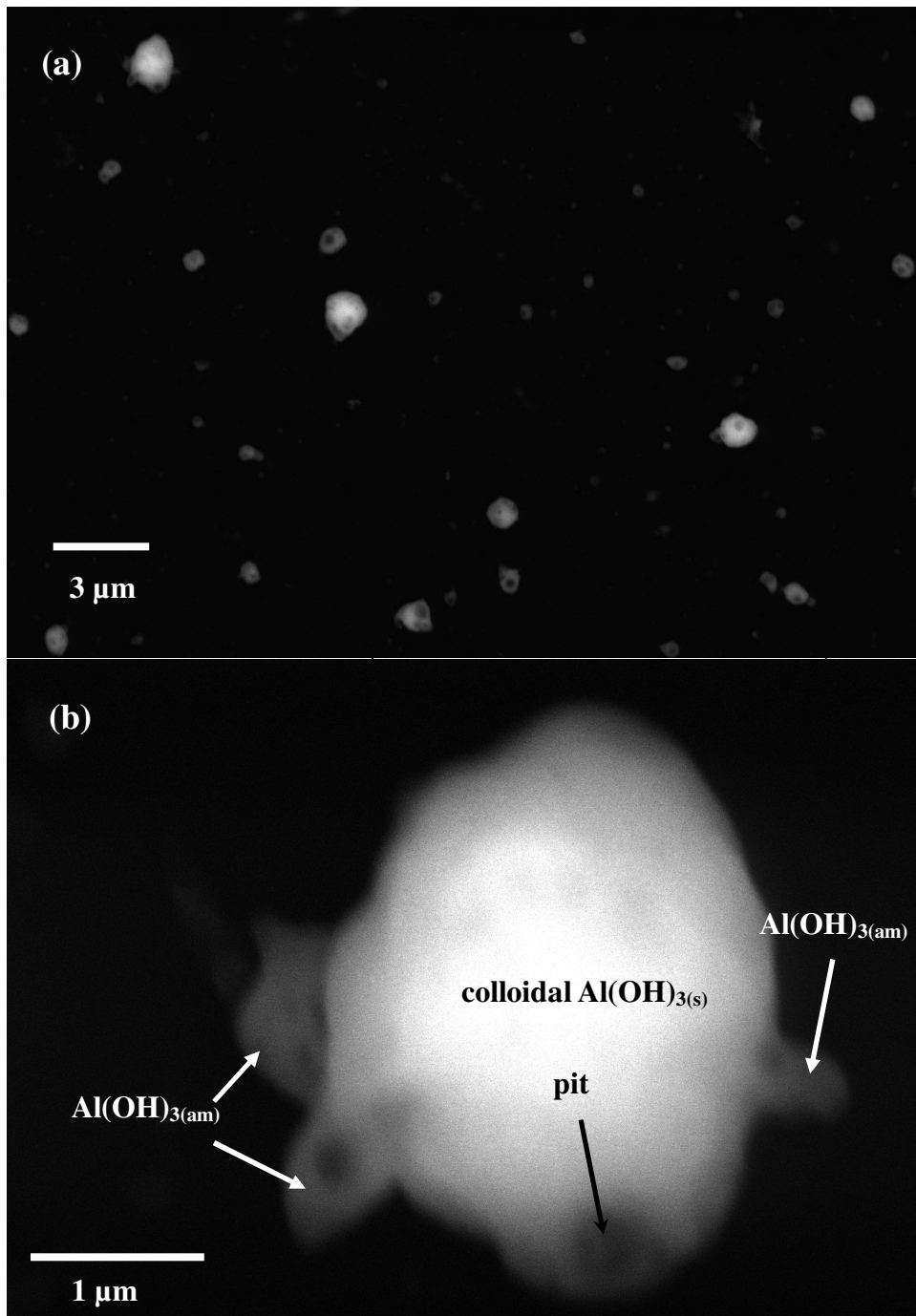


Fig. 6.4 WSEM micrographics of Al(OH)_3 precipitates formed after 1 min rapid mixing at 200 rpm: (a) ($\times 3,750$); (b) ($\times 50,000$).

6.3 Surface Composition of Al-Flocs

The $\text{Al}(\text{OH})_3$ precipitates and Al_{13} possess a specific Al composition, and they keep a particular ratio between tetrahedral Al (Al^{IV}) and octahedral Al (Al^{VI}). To further understand the Al composition on the surfaces of $\text{Al}(\text{OH})_3$ -rich and Al_{13} -aggregate flocs, the quantitative analysis of the various Al species was identified by XPS. The high resolution XPS scans of the aluminum are presented in **Fig. 6.5**. The aluminum high resolution scans show the single Al 2p transitions with binding energies of 74 eV for kaolin powder, while two overlapping bands associated with two different Al 2p transitions with binding energies of 72 and 74 eV, corresponding to Al^{IV} and Al^{VI} (Duong et al., 2005). In general, tetrahedrally coordinated aluminum has a lower binding energy than octahedrally coordinated aluminum.

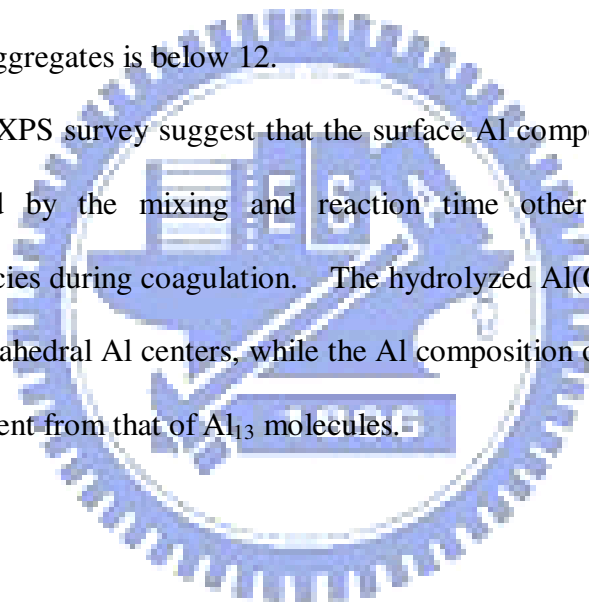
For $\text{Al}(\text{OH})_3$ -rich flocs, the Al 2p with lower binding energy around 72 eV is assigned to Al^{IV} , while the Al 2p with higher binding energy at 74 eV is assigned to Al^{VI} , as illustrated in **Fig. 6.5 (b)**. The ratio between Al^{IV} and Al^{VI} is 1:1.63, which implies these $\text{Al}(\text{OH})_3$ precipitates on the surface of particles are intrinsically different. Because the kaolin only contains single Al^{IV} , as proved in **Fig. 6.5 (a)**, it is unlikely that the presence of abundant Al^{IV} originates from kaolin powder. In addition, $\text{Al}(\text{OH})_3$ mainly possesses a Al^{VI} center (Masion et al., 2000; Isobe et al., 2003). Therefore, it is clear that there has a large number of $\text{Al}(\text{OH})_3$ with a Al^{IV} center on the $\text{Al}(\text{OH})_3$ -rich flocs, which is similar to previous ^{27}Al -NMR study of amorphous $\text{Al}(\text{OH})_3$ that contains tetrahedral and pentahedral coordinations of $\text{Al}(\text{O})_4$ and $\text{Al}(\text{O})_5$ as well as octahedral coordination of $\text{Al}(\text{O})_6$ (Isobe et al., 2003). This result can be explained by the condensation of in-situ formed Al_{13} . In this study, there are only two species in aqueous solutions that have $\text{Al}(\text{O})_4$ (Al^{IV}): the

monomeric $\text{Al}(\text{OH})_4^-$ (aq) and Al_{13} (aq). For PACI-C coagulation at neutral pH, Al_{13} represents much more of the total $\text{Al}(\text{O})_4$ than $\text{Al}(\text{OH})_4^-$. The monomeric Al of PACI-C transforms into metastable Al_{13} rapidly during initial coagulation where the in-situ formed Al_{13} can become solid aluminum hydroxide via the condensation of Al_{13} (Sposito, 1996). Although other study has proposed that the metastable Al_{13} will undergo directly structure rearrangement to form gibbsite with sufficient aging (Hsu, 1988), Furrer et al. (2002) have proved the speciation of $\text{Al}(\text{OH})_{3(\text{am})}$ flocs in natural rivers are originated from the aggregation of Keggin Al_{13} polycation as a result of the rapid mixing and episodic reaction in which they probably remain a $\text{Al}(\text{O})_4$ center. This phenomenon is accentuated particularly for this study. On the other hand, the condensation of outer Al-OH groups may accompany the formation of partial Al-O-Al strained linkage, leading to the occurrence of five-coordinate $\text{Al}(\text{O})_5$ and six-coordinate $\text{Al}(\text{O})_6$ in aluminum hydroxide (Piedra and Fitzgerald, 1996). As evidenced in **Fig. 4.3**, the ratio between Al_b (Al_{13}) and Al_c ($\text{Al}(\text{OH})_3$) is about 1:1.6, which is in accordance with the results of XPS survey. As a result, though the PACI-C flocs involves abundant $\text{Al}(\text{OH})_3$ precipitates that mainly possess Al^{VI} , parts of them still remain Al^{IV} centers potentially due to rapid mixing for a short period.

A distinct change in the characteristic peak of tetrahedrally coordinated aluminum is apparent in the XPS survey data of Al_{13} -aggregate flocs. The characteristic peak of Al 2p with a binding energy of 73 eV is obvious, as shown in **Fig. 6.5 (c)**. This may be due to the changes in binding energy between the Al_{13} aggregates and the surface of particles. From the data of XPS survey for Al_{13} -aggregate flocs, it is found that the Si/Al is about 0.6 that is higher than that for $\text{Al}(\text{OH})_3$ -rich flocs, indicating the existence of more Si-O units on the surface of

Al₁₃-aggregate flocs. For aluminum in oxide environments, the higher Si/Al ratio can progressively forces the Al-O bond to be more ionic and thus the Al 2p binding energy increases (Barr et al., 1997). This demonstrates that the binding energy of Al^{IV}-O on the surface of the Al₁₃-aggregate flocs is higher than that on the surface of Al(OH)₃-rich flocs. For Al₁₃ molecules, the proportion of Al^{IV} to Al^{VI} should be 1:12 in theory (Johansson, 1960). On the surface of Al₁₃-aggregate flocs, however, the Al^{IV}/Al^{VI} ratio is about 1:9.9, suggesting the existence of Al₁₃ aggregates. During the formation of Al₁₃ aggregates, Al₁₃ molecules condense and aggregate result from the decomposition of the outer octahedral structure. Accordingly, the Al^{VI}/Al^{IV} of Al₁₃ aggregates is below 12.

The results of XPS survey suggest that the surface Al composition of flocs also could be affected by the mixing and reaction time other than predominant hydrolyzed Al species during coagulation. The hydrolyzed Al(OH)_{3(am)} precipitates contain certain tetrahedral Al centers, while the Al composition of Al₁₃ aggregates is significantly different from that of Al₁₃ molecules.



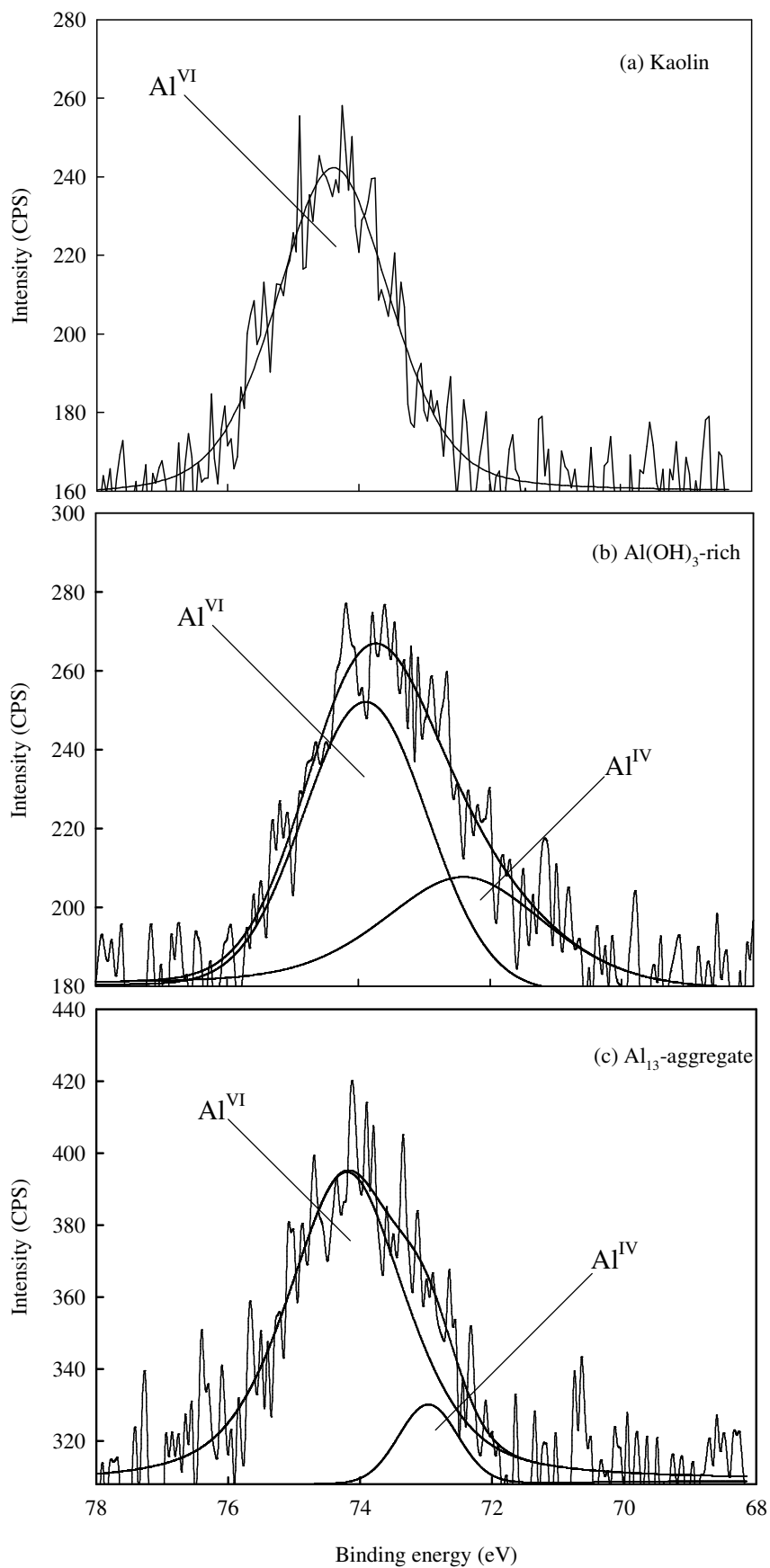
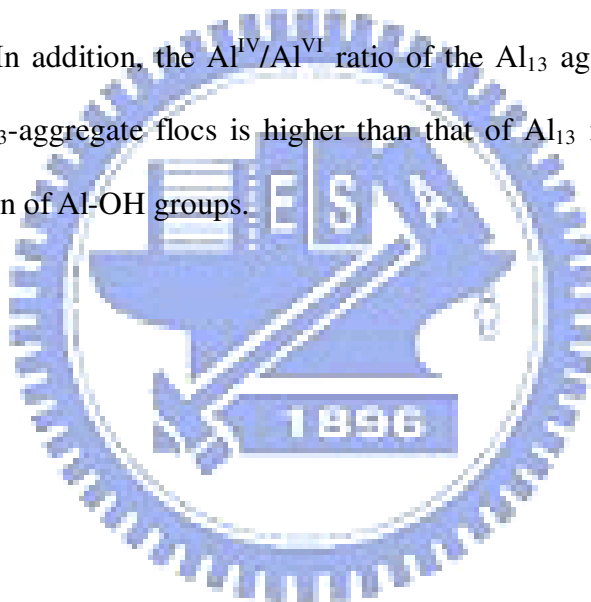


Fig. 6.5 Al 2p scans of XPS for (a) Kaolin powder (b) Al(OH)₃-rich and (c) Al₁₃-aggregate flocs.

6.4 Summary

The Al(OH)_3 -rich flocs are larger and have a ragged and fuzzy exterior with an looser structure, while the Al_{13} -aggregate flocs are smaller with smooth contour. The Al(OH)_3 -rich flocs do not possess well-formed crystalline structure, while the Al_{13} aggregates with Al_{13} -like structure is found within the Al_{13} -aggregate flocs. The preformed colloidal $\text{Al(OH)}_{3(s)}$ in PACI-C is spherical-like and has a sunken surface. On the surface of the Al(OH)_3 -rich flocs, there are multitude of amorphous Al(OH)_3 precipitates that involve either Al(O)_4 or Al(O)_6 center, where the $\text{Al}^{\text{IV}}/\text{Al}^{\text{VI}}$ ratio is almost equal to 2:3, similar to the ratio of Al_b/Al_c during coagulation measured by Ferron method. In addition, the $\text{Al}^{\text{IV}}/\text{Al}^{\text{VI}}$ ratio of the Al_{13} aggregates observed on the surface of Al_{13} -aggregate flocs is higher than that of Al_{13} molecules potentially due to condensation of Al-OH groups.



CHAPTER VII

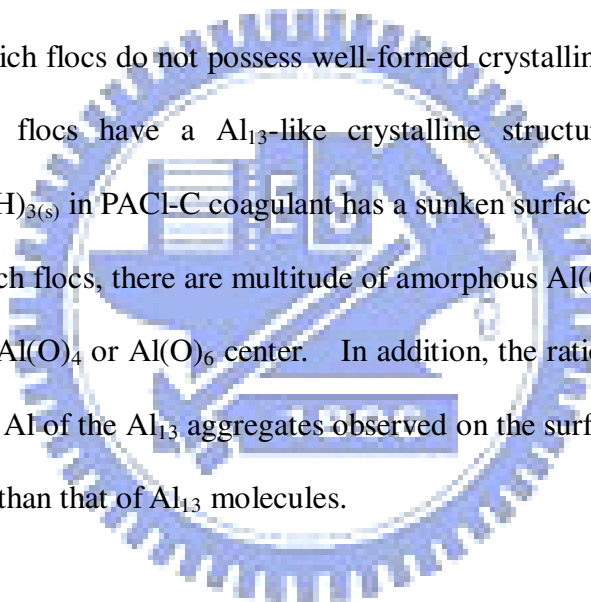
CONCLUSIONS AND RECOMMENDATIONS

Based on the results of this study, the following conclusions could be drawn:

7.1 Conclusions

1. The PACI-C with monomeric and colloidal Al species favors enmeshment or sweep flocculation at neutral pH in response to the occurrence of abundant $\text{Al}(\text{OH})_3$ precipitates, including $\text{Al}(\text{OH})_{3(\text{am})}$ and colloidal $\text{Al}(\text{OH})_{3(\text{s})}$. By contrast, the PACI-E containing 60% Al_{13} of total Al concentration causes either electrostatic patch or charge neutralization mechanisms with Al_{13} aggregates at pH 10. At such pH, interparticle bridging becomes the major destabilization mechanism at sufficient dosage (8 mg/L as Al) for PACI- Al_{13} coagulation, while electrostatic patch rules the particle destabilization at low dosage (1 mg/L as Al). At alkaline pH, the coagulation efficiency of PACI-E is superior to that of PACI- Al_{13} and PACI-C.
2. The aggregation modes under various destabilization mechanisms can be differentiated via the growth and structure of flocs during coagulation. The structure of sweep flocs formed by enmeshment or sweep flocculation and PACI-E flocs formed by electrostatic patch becomes more compact with dosage, where the breakage of sweep flocs increases the fractal dimension of flocs, while PACI-E flocs have a stronger resistance to shear stress during coagulation. For PACI- Al_{13} coagulation, the structure of PACI- Al_{13} flocs becomes looser with dosage as a result of interparticle bridging which results in the formation of fragile flocs.

3. For the investigation on the formation of Al_{13} aggregates, some micro-scale linear Al_{13} aggregates composed of a chain of coiled Al_{13} and coiled Al_{13} aggregates with different dimensions are observed on the mica. The surface of the Al_{13} aggregates is softer and smoother, and their size ranges from 300 nm to 400 nm as a flat conformation of 2-3 nm.
4. Enmeshment causes the sweep flocs with a rough and ragged contour. By contrast, electrostatic patch or charge neutralization induces flocs with a smooth and glossy surface. Interparticle bridging brings about the Al_{13} -aggregate flocs with a looser and fluffy contour.
5. The $Al(OH)_3$ -rich flocs do not possess well-formed crystalline structure, while the Al_{13} -aggregate flocs have a Al_{13} -like crystalline structure. The preformed colloidal $Al(OH)_{3(s)}$ in PACl-C coagulant has a sunken surface. On the surface of the $Al(OH)_3$ -rich flocs, there are multitude of amorphous $Al(OH)_3$ precipitates that involve either $Al(O)_4$ or $Al(O)_6$ center. In addition, the ratio between tetrahedral and octahedral Al of the Al_{13} aggregates observed on the surface of Al_{13} -aggregate flocs is higher than that of Al_{13} molecules.



7.2 Recommendations

The following recommendations were made on the application of various PACl coagulants and further investigation on PACl coagulation for the destabilization of colloidal particles.

1. In practice, commercial PACl containing voluminous monomeric Al and colloidal $\text{Al}(\text{OH})_{3(s)}$ can be generally applied to coagulate the turbid water at neutral pH. PACl with more than 60% Al_{13} of total Al concentration is suitable to coagulate the water or wastewater with alkaline pH (e.g., Chemical Mechanical Polishing (CMP) wastewater) for efficient turbidity removal.
2. Further investigations on the interaction forces between colloids is necessary to determine the forces model, involving DLVO forces or non DLVO forces, induced by Al_{13} aggregates through force-mode AFM with colloidal probe.
3. The coagulation dynamics of particles coagulated by various PACl coagulants should be further investigated by calculating convection modes such as Brownian-induced or shear-induced motions with the theoretical diffusion equation (e.g., Peclet number) to understand the effect of Al species on collisions between particles of different size.

BIBLIOGRAPHY

Akari, S., Schrepp, W. and Horn, D. Imaging of single polyethylenimine polymers adsorbed on negatively charged latex spheres by chemical force microscopy. *Langmuir* **12(4)**, 857-860, 1996.

Akitt, J. W. and Elders, J. M. Multinuclear magnetic resonance studies of the hydrolysis of aluminum(III). VIII. Base hydrolysis monitored at very high magnetic field. *J. Chem. Soc. Dalton Trans.* **5**, 1347-1355, 1988.

Akitt, J. W. and Farthing, A. Aluminum-27 nuclear magnetic resonance studies of the hydrolysis of aluminum(III). II. Gel-permeation chromatography. *J. Chem. Soc. Dalton Trans.* **7**, 1606-1608, 1981.

Akitt, J. W. Multinuclear studies of aluminum compounds. *Prog. NMR Spectrosc.* **21**, 1-149, 1989.

Allouche, L., Gérardin, C., Loiseau, T., Férey, G. and Taulelle, F. Al₃₀: A giant aluminum Polycation. *Angew. Chem. Int. Ed.* **39**, 511-514, 2000.

Amirtharajah, A. and Mills, K. M. Rapid-mix design for mechanism of alum coagulation. *J. Am. Water Works Assoc.* **74**, 210-216, 1982.

Annadurai, G., Sung, S. S. and Lee, D. J. Optimization of floc characteristics for treatment of highly turbid water. *Sep. Sci. Technol.* **39**, 19-42, 2004.

Arita, T., Kanda, Y. and Higashitani, K. In situ observation of single polymers adsorbed onto mica surfaces in water. *J. Colloid Interf. Sci.* **273**, 102-105, 2004.

Aubert, C. and Cannell, D. S. Restructuring of colloidal silica aggregates. *Phys. Rev. Lett.* **56(7)**, 738-741, 1986.

AWWA. Jar Testing. In *Operation Control of Coagulation and Filtration Processes*. AWWARF. Ed., 1-41, 1992.

Axeols, M. A. V., Tchoubar, D. and Jullien, R. X-ray scattering functions of fractal structures: comparison between simulations and experiments. *J. Phys.* **47(10)**, 1843-1847, 1986.

Bache, D. H., Johnson, C., McGilligan, J. F. and Rasool, E. A conceptual view of floc structure in the sweep floc domain. *Water Sci. Technol.* **36(4)**, 49-56, 1997.

Baes, C. F. and Mesmer, R. E. *The Hydrolysis of Cations*. Jhon Wiley & Sons, New York, 1976.

Barr, T. L., Seal, S., Wozniak, K. and Klinowski, J. ESCA studies of the coordination state of aluminium in oxide environments. *J. Chem. Soc., Faraday Trans.* **93(1)**, 181-186, 1997.

Benefield, L. D., Judkins, Jr. J. F. and Weand, B. L. *Process Chemistry for Water and Wastewater Treatment*. Prentice Hall, New Jersey, 1982.

Berka, M. and Rice, J. A. Relation between aggregation kinetics and the structure of kaolinite aggregates. *Langmuir* **21**, 1223-1229, 2005.

Bertsch, P. M. Conditions for Al₁₃ polymer formation in partially neutralized aluminum solutions. *Soil Sci. Soc. Am. J.* **51**, 825-828, 1987.

Bertsch, P. M., Barnhisel, R. I., Thomas, G. W., Layton, W. J. and Smith, S. L. Quantitative determination of aluminum-27 by high resolution nuclear magnetic resonance spectrometry. *Anal. Chem.* **58(12)**, 2583-2585, 1986a.

Bertsch, P. M., Layton, W. J. and Barnhisel, R. I. Speciation of hydroxyaluminum solutions by wet chemical and aluminum. *Soil Sci. Soc. Am. J.* **50**, 1449-1454, 1986b.

Biggs, C. A. and Lant, P. A. Activated sludge flocculation: on-line determination of floc size and the effect of shear. *Water Res.* **34**, 2542-2550, 2000.

Biggs, S., Habgood, M., Jameson, G. and Yan, Y. D. Aggregate structures formed via a bridging flocculation mechanism. *Chem. Eng. J.* **80**, 13-22, 2000.

Bottero, J. Y., Axelos, M., Tchoubar, D., Cases, J. M., Fripiat, J. J. and Flessinger, F. Mechanism of formation of aluminum trihydroxide from Keggin Al₁₃ polymers. *J. Colloid Interf. Sci.* **117**, 47-57, 1987.

Bottero, J. Y., Cases, J. M., Fiessinger, F. and Poirier, J. E. Studies of hydrolyzed aluminum chloride solutions. I. Nature of aluminum species and composition of aqueous solutions. *J. Phys. Chem.* **84**, 2933-2939, 1980.

Bottero, J. Y., Tchoubar, D., Cases, J. M. and Flessinger, F. Investigation of the hydrolysis of aqueous-solutions of aluminum-chloride. II. Nature and structure by small-angle X-ray-scattering. *J. Phys. Chem.* **86**, 3667-3673, 1982.

Bradley, S. M., Kydd, R. A. and Howe, R. F. The structure of Al-gels formed through base hydrolysis of Al³⁺ aqueous solutions. *J. Colloid Interf. Sci.* **159**, 405-412, 1993.

Brakalov, L. B. A connection between orthokinetic coagulation capture efficiency of aggregates and their maximum size. *Chem. Eng. Sci.* **42**, 2373-2383, 1987.

Chakraborti, R. K., Atkinson, J. F. and Van Benschoten, J. E. Characterization of alum floc by image analysis. *Environ. Sci. Technol.* **34**, 3969-3976, 2000.

Chakraborti, R. K., Gardner, K. H., Atkinson, J. F. and Van Benschoten, J. E. Changes in fractal dimension during aggregation. *Water Res.* **37**, 873-883, 2003.

Chen, Z. Y., Fan, B., Peng, X. J., Zhang, Z. G., Fan, J. H. and Luan, Z. K. Evaluation of Al₃₀ polynuclear species in polyaluminum solutions as coagulant for water treatment. *Chemosphere* **64**, 912-918, 2006.

Cheng, K. K. and Chou, T. C. Crystal Structure Transformation of Solid Polyaluminium Chloride. *International Chemical Congress of Pacific Basin Societies*, Hawaii, Dec. 14-19, 2000.

Chin, C. J., Yiacoumi, S. and Tsouris, C. Influence of metal ion sorption on colloidal surface forces measured by atomic force microscopy. *Environ. Sci. Technol.* **36**, 343-348, 2002.

Chowdhury, Z. K. and Amy, G. L. Coagulation of submicron colloids in water treatment by incorporation into aluminum hydroxide floc. *Environ. Eng. Sci.* **25**, 1766-1773, 1991.

Chu, C. P., Lee, D. J. and Peng, X. F. Structure of conditioned sludge flocs. *Water Res.* **38**, 2125-2134, 2004.

Clark, M. M. and Flora, J. R. V. Floc restructuring in varied turbulent mixing. *J. Colloid Interf. Sci.* **147**, 407-420, 1991.

Dentel, S. K. Application of the precipitation-charge neutralization model of coagulation. *Environ. Sci. Technol.* **22**, 825-832, 1988.

Derjaguin, B. V. and Landau, L. D. Theory of the stability of strongly charged lyophobic sols and of the adhesion of strongly charged particles in solutions of electrolytes. *Acta Physicochimica URSS* **14**, 733-762, 1941.

Duan, J. and Gregory, J. Coagulation by hydrolyzing metal salts. *Adv. Colloid Interf. Sci.* **100-102**, 475-502, 2003.

Dubbin, W. E. and Sposito, G. Copper-glyphosate sorption to microcrystalline gibbsite in the presence of soluble Keggin Al-13 polymer. *Environ. Sci. Technol.* **39**, 2509-2514, 2005.

Ducoste, J. J. and Clark, M. M. The influence of tank size and impeller geometry on turbulent flocculation: I. Experimental. *Environ. Eng. Sci.* **15(3)**, 215-224, 1998.

Duong, L. V., Wood, B. J. and Klopogge, J. T. XPS study of basic aluminum sulphate and basic aluminium nitrate. *Materials Letters* **59(14-15)**, 1932-1936, 2005.

Elimelech, M., Gregory, J., Jia, X. and Williams, R. A. *Particle Deposition and Aggregation: Measurement, Modeling and Simulation*. Butterworth-Heinemann Ltd., Oxford, 1995.

Francois, R. J. Growth kinetics of hydroxide flocs. *J. Am. Water Works Assoc.* **80**, 92-96, 1988.

Francois, R. J. Strength of aluminium hydroxide flocs. *Water Res.* **21**, 1023-1030, 1987.

Fu, G., Nazar, L. F. and Bain, A. D. Aging processes of aluminum sol-gels: characterization of new aluminum polyoxycations by ^{27}Al NMR spectroscopy. *Chem. Mater.* **3(4)**, 602-610, 1991.

Furrer, G., Gfeller, M. and Wehrli, B. On the chemistry of the Keggin Al_{13} polymer: Kinetics of proton-promoted decomposition. *Geochim. Cosmochim. Acta.* **63**, 3069-3076, 1999.

Furrer, G., Ludwig, C. and Schindler, P. W. On the chemistry of the Keggin Al_{13} polymer. I. Acid-base properties. *J. Colloid Interf. Sci.* **149**, 56-67, 1992.

Furrer, G., Phillips, B., Ulrich, K. U., Pöthig, R. and Casey, W. H. The origin of aluminum flocs in polluted streams. *Science* **297**, 2245-2247, 2002.

Gallucci, E. and Scrivener, K. In situ dynamic SEM imaging of hydration of cement using WETSEM technology. *Adv. Appl. Ceram.* **106**, 319-326, 2007.

Gao, B. Y., Chu, Y. B., Yue, Q. Y., Wang, B. J. and Wang, S. G. Characterization and coagulation of a polyaluminum chloride (PAC) coagulant with high Al_{13} content. *J. Environ. Manage.* **76**, 143-147, 2005.

Glasgow, L. A. and Luecke, R. H. Mechanisms of deaggregation for clay-polymer flocs in turbulent systems. *Ind. Eng. Chem. Fundam.* **19(2)**, 148-156, 1980.

Gregory, J. and Dupont, V. Properties of flocs produced by water treatment coagulants. *Water Sci. Technol.* **44(10)**, 231-236, 2001.

Gregory, J. Flocculation by polymers and polyelectrolytes. In *Solid/liquid dispersions*. Ed. by Tadros, T. F. Academic Press, London, 163-181, 1987.

Gregory, J. Polymer adsorption and flocculation in sheared suspensions. *Colloid Surface* **31**, 231-253, 1988.

Gregory, J. Polymer adsorption and flocculation. In *Industrial water soluble polymers*. Ed. by Finch, C. A. Royal Society of Chemistry, London, 62-75, 1996.

Gregory, J. Rates of flocculation of latex particles by cationic polymers. *J. Colloid Interf. Sci.* **42**, 448-456, 1973.

Gregory, J. The density of particle aggregates. *Wat. Sci. Tech.* **36(4)**, 1-13, 1997.

Guan, J., Waite, T. D. and Amal, R. Rapid structure characterization of bacterial aggregates. *Environ. Sci. Technol.* **32**, 3735-3742, 1998.

Hsu, P. H. Mechanisms of gibbsite crystallization from partially neutralized aluminum chloride solutions. *Clays Clay Miner.* **36**, 25-30, 1988.

Hu, C. Z., Liu, H. J. and Qu, J. H. Preparation and characterization of polyaluminum chloride containing high content of Al₁₃ and active chlorine. *Colloid Surface A* **260**, 109-117, 2005.

Hu, C. Z., Liu, H. J., Qu, J. H., Wang, D. S. and Ru, J. Coagulation behavior of aluminum salts in eutrophic water: significance of Al₁₃ species and pH control. *Environ. Sci. Technol.* **40**, 325-331, 2006.

Ikai, A. STM and AFM of bio/organic molecules and structures. *Surface Science Reports* **26**, 261-332, 1996.

Isobe, T., Watanabe, T., d'Espinose de la Caillerie, J. B., Legrand, A. P. and Massiot, D. Solid-state H-1 and Al-27 NMR studies of amorphous aluminum hydroxides. *J. Colloid Interf. Sci.* **261(2)**, 320-324, 2003.

Israelachvili, J. N. *Intermolecular and surface forces*. 2nd Ed. Academic Press, London, 1991.

Jarvis, P., Jefferson, B., Gregory, J. and Parsons, S. A. A review of floc strength and breakage. *Water Res.* **39**, 3121-3137, 2005.

Jiang, Q. and Logan, B. E. Fractal dimensions of aggregates determined from steady-state size distributions. *Environ. Sci. Technol.* **25**, 2031-2038, 1991.

Jiang, Q. and Logan, B. E. Fractal dimensions of aggregates from shear devices. *J. Am. Water Works Assoc.* **88(2)**, 100-113, 1996.

Johansson, G. On the crystal structures of some basic aluminum salts. *Acta Chem. Scand.* **14**, 771-773, 1960.

Johnston, C. T., Sposito, G. and Erickson, C. Vibrational probe studies of water interactions with montmorillonite. *Clay Clay Miner.* **40**, 722-730, 1992.

Kan, C. C., Huang, C. P. and Pan, J. R. Time requirement for rapid-mixing in coagulation. *Colloid Surface A* **203**, 1-9, 2002.

Katz, A., Bentur, A. and Kovler, K. A novel system for in-situ observations of early hydration reactions in wet conditions in conventional SEM. *Cement Concrete Res.* **37**, 32-37, 2007.

Kazpard, V., Lartiges, B. S., Frochot, C., d'Espinose de la Caillerie, J. B., Viriot, M. L., Portal, J. M., Görner, T. and Bersillon, J. L. Fate of coagulant species and conformational effects during the aggregation of a model of a humic substance with Al₁₃ polycations. *Water Res.* **40**, 1965-1974, 2006.

Kloprogge, J. T. and Frost, R. L. Raman microscopy study of basic aluminum sulfate. *J. Mater. Sci.* **34**(17), 4199-4202, 1999.

Kloprogge, J. T., Seykens, D., Jansen, J. B. H. and Geus, J. W. A ²⁷Al nuclear magnetic resonance study. *J. Non-Cryst. Solids* **142**, 94-102, 1992.

Kostansek, E. Controlled coagulation of emulsion polymers. *JCT Res.* **1**, 41-44, 2004.

Kusters, K. A. *The influence of turbulence on aggregation of small particles in agitated vessels*. Ph. D. Thesis, Eindhoven University of Technology. The Netherlands, 1991.

Lee, C. and Kramer, T. A. Prediction of three-dimensional fractal dimensions using the two-dimensional properties of fractal aggregates. *Adv. Colloid Interf. Sci.* **112**, 49-57, 2004.

Lee, D. G., Bonner, J. S., Garton, L. S., Ernest, A. N. S. and Autenrieth, R. L., Modeling coagulation kinetics incorporating fractal theories: comparison with observed data. *Water Res.* **36**, 1056-1066, 2002.

Lerman, A. *Geochemical Processes*. New York, Wiley Interscience, 1979.

Letterman, R. D. and Asolekar, S. R. A. Surface ionization of polynuclear species in Al(III) hydrolysis-1. Titration results. *Water Res.* **24**, 931-939, 1990.

Letterman, R. D., Quon, J. K. and Gemmel, R. S. Influence of rapid mix parameters on flocculation. *J. Am. Water Work Assoc.* **65**, 716-725, 1973.

Letterman, R. D., Vanderbrook, S. G. and Sricharoenchaikit, P. Electrophoretic mobility measurements in coagulation with alum salts. *J. Am. Water Work Assoc.* **74**, 44-51, 1982.

Li, D. H. and Ganczarczyk, J. J. Fractal Geometry of Particle Aggregates Generated in Water and Wastewater Treatment Processes. *Environ. Sci. Technol.* **23**, 1385-1389, 1989.

Li, J., Fitz-Gerald, J. M., Oberhauser, J. P. Novel wet SEM imaging of organically modified montmorillonite clay dispersions. *Appl. Phys. A-Mater.* **87(1)**, 97-102, 2007.

Licskó, I. Realistic coagulation mechanisms in the use of aluminium and iron(III) salts. *Water Sci. Technol.* **36(4)**, 103-110, 1997.

Lin, M. Y., Lindsay, H. M., Weitz, D. A., Ball, R. C., Klein, R. and Meakin, P. Universality in colloid aggregation. *Nature* **339**, 360-362, 1989.

Linnow, K., Juling, H. and Steiger, M. Investigation of NaCl deliquescence in porous substrates using RH-XRD. *Environ. Geol.* **52(2)**, 383-393, 2007.

Liu, G. G., Qu, J. H. and Tang, H. G. The electrochemical production of highly effective polyaluminum chloride. *Water Res.* **33**, 807-813, 1999.

Lyklema, J. *Fundamentals of Interface and Colloid Science*. Academic Press. New York vol II, 4.1-4.120, 1995.

Madejova, J., Janek, M., Komadel, P., Herbert, H. J. and Moog, H. C. FTIR analyses of water in MX-80 bentonite compacted from high salinary salt solution systems. *Appl. Clay Sci.* **20**, 255-271, 2002.

Mandelbrot, B. B. *The Fractal Geometry of Nature*. Freeman, San Francisco, 1982.

Mandelbrot, B. B. *The Fractal Geometry of Nature*; W. H. Freeman and Co.: New York, 1983.

Martin, Y., Williams, C. C. and Wickramasinghe, H. K. Atomic force microscope force mapping and profiling on a sub 100-Å scale. *J. Appl. Phys.* **61(10)**, 4723-4729, 1987.

Masion, A., Vilgé-Ritter, A., Rose, J., Stone, W. E. E., Teppen, B. J., Rybacki, D. and Bottero, J. Y. Coagulation-flocculation of natural organic matter with Al salts: speciation and structure of the aggregates. *Environ. Sci. Technol.* **34(15)**, 3242-3246, 2000.

Matsui, Y., Yuasa, A., Furuya, Y. and Kamei, T. Dynamic analysis of coagulation with alum and PACl. *J. Am. Water Works Assoc.* **90(10)**, 96-106, 1998.

Matsumoto, T. and Adachi, Y. Effect of ionic strength on the initial dynamics of flocculation of polystyrene latex with polyelectrolyte. *J. Colloid Interf. Sci.* **204**, 328-335, 1998.

McCurdy, K., Carlson, K. and Gregory, D. Flocc morphology and cyclic shearing recovery: comparison of alum and polyaluminium chloride coagulants. *Water Res.* **38**, 486-494, 2004.

Meakin, P. and Witten, T. A. Growing interface in diffusion-limited aggregation. *Phys. Rev. A* **28**, 2985-2989, 1983.

Meakin, P. Fractal aggregates. *Adv. Colloid Interface Sci.* 28(4), 249-331, 1988.

Mikkelsen, L. H. and Keiding, K. The shear sensitivity of activated sludge: an evaluation of the possibility for a standardised floc strength test. *Water Res.* **36**, 2931-2940, 2002.

Molis, E., Thomas, F., Bottero, J. Y., Barres, O. and Masion, A. Chemical and structural transformation of aggregated Al-13 polycations, promoted by salicylate ligand. *Langmuir* **12(13)**, 3195-3200, 1996.

Nalaskowski, J., Veeramasoneni, S., Hupka, J. and Miller, J. D. Interactions between fossil resin and coal in the presence of anionic and cationic surfactants. *Colloid Surface A* **154**, 103-113, 1999.

Oles, V. Shear-induced aggregation and breakup of polystyrene latex particles. *J. Colloid Interf. Sci.* **154**, 351-358, 1992.

Parker, D. R. and Bertsch, P. M. Identification and quantification of the Al₁₃ tridecameric polycation using ferron. *Environ. Sci. Technol.* **26**, 914-913, 1992.

Parthasarathy, N. and Buffle, J. Study of polymeric aluminum(III) Hydroxide solutions for application in waste water treatment. Properties of the polymer and optimal conditions of preparation. *Water Res.* **19(1)**, 25-36, 1985.

Pelssers, E. G., Cohen, M., Stuart, M. A. and Fleer, G. J. Kinetic aspects of polymer bridging: Equilibrium flocculation and nonequilibrium flocculation. *Colloid Surface* **38**, 15-25, 1989.

Pernitsky, D. J. and Edzwald, K. Solubility of polyaluminium coagulants. *J. Water Suppl.: Res. Technol.-AQUA* **52**, 395-406, 2003.

Phillips, B. L., Casey, W. H. and Karlsson, M. Bonding and reactivity at oxide mineral surfaces from model aqueous complexes. *Nature* **404**, 379-382, 2000.

Piedra, G., Fitzgerald, J. J., Dando, N., Dec, S. F. and Maciel, G. E. Solid-state ¹H NMR studies of aluminum oxide hydroxides and hydroxides. *Inorg. Chem.* **35**, 3474-3478, 1996.

Potantin, A. A. On the computer-simulation of the deformation and breakup of colloidal aggregates in shear-flow. *J. Colloid Interf. Sci.* **157**, 399-410, 1993.

Pouillot, M. and Suty, H. High-basicity polymeric aluminum salts for drinking-water production. *Water Supply*, **10(4)**, 133-153, 1992.

Putman, C. A. J., van der Werf, K. O., De Grooth, B. G., Van Hulst, N. F. and Greve, J. Tapping atomic-force microscopy in liquid. *Appl. Phys. Lett.* **64**, 2454-2456, 1994.

Rakotonarivo, E., Bottero, J. Y., Thomas, F., Poirier, J. E. and Cases, J. M. Electrochemical modeling of freshly precipitated aluminum hydroxide-electrolyte interface. *Colloid Surface* **33**, 191-207, 1988.

Rowell, J. and Nazar, L. F. Speciation and thermal transformation in alumina sols: Structures of the polyhydroxyoxoaluminum cluster and its δ -Keggin moiety. *J. Am. Chem. Soc.* **122**, 3777-3778, 2000.

Shi, B. Y., Li, G. H., Wang, D. S. and Tang, H. X., Separation of Al_{13} from polyaluminum chloride by sulfate precipitation and nitrate metathesis. *Sep. Purif. Technol.* **54**, 88-95, 2007.

Shu, L., Schlüter, A. D., Ecker, C., Severin, N. and Rabe, J. P. Extremely long dendronized polymers: synthesis, quantification of structure perfection, individualization, and SFM manipulation. *Angew. Chem. Int. Ed.* **40(24)**, 4666-4669, 2001.

Smith, R. W. Reactions among equilibrium and nonequilibrium aqueous species of aluminum hydroxyl complexes. *Adv. Chem. Ser.* **106**, 250-279, 1971.

Sonntag, R. C. and Russel, W. B. Structure and breakup of flocs subjected to fluid stresses I. Shear Experiments. *J. Colloid Interf. Sci.* **113**, 399-413, 1986.

Spicer, P. T. and Pratsinis, S. E. Shear-induced flocculation: the evolution of floc structure and the shape of the size distribution at steady state. *Water Res.* **30**, 1049-1056, 1996.

Sposito, G. *Characterization of particle surface charge. Environmental Particles.* B. J. v. HP. Lewis Publishers, Boca Raton. **1**, 291-314, 1993.

Sposito, G. *The Environmental Chemistry of Aluminum.* 2nd Ed. CRC press, 1996.

Stipp, S. L. S. In situ, real-time observations of the adsorption and self-assembly of macromolecules from aqueous solution onto an untreated, natural surface. *Langmuir* **12(7)**, 1884-1891, 1996.

Tambo, N. and Hozumi, H. Physical characteristics of flocs. 2. Strength of floc. *Water Res.* **13**, 421-427, 1979.

Tambo, N. and Watanabe, Y. Physical aspect of flocculation process: I. Fundamental treatise. *Water Res.* **13**, 429-439, 1979.

Thomas, D. C. Transport characteristics of suspension: VIII. A note on the viscosity of Newtonian suspensions of uniform spherical particles. *J. Colloid Interf. Sci.* **20**, 267-327, 1965.

Thomas, D. N., Judd, S. J. and Fawcett, N. Flocculation modeling: a review. *Water Res.* **33**, 1579-1592, 1999.

Torres, F. E., Russel, W. B. and Schowalter, W. R. Simulations of coagulation in viscous flows. *J. Colloid Interf. Sci.* **145**, 51-73, 1991.

Van Benschoten, J. E. and Edzwald, J. K. Chemical aspects of coagulation using aluminum slats-2. Coagulation of fulvic acid using alum and polyaluminum chloride. *Water Res.* **24**, 1519-1526, 1990.

Verwey, E. J. W. and Overbeek, J. Th. G. *Theory of the stability of lyophobic colloids*. Elsevier, Amsterdam, 1948.

Violante, A. and Huang, P. M. Influence of inorganic and organic-ligands on the formation of aluminum hydroxides and oxyhydroxides. *Clays Clay Miner.* **33**, 181-191, 1985.

Wadu-Mesthrige, K., Amro, N. A., Garno, J., C., Cruchon-Dupeyrat, S. and Liu, G. Y. Contact resonance imaging-A simple approach to improve the resolution of AFM for biological and polymeric materials. *Applied Surface Science* **175-176**, 391-398, 2001.

Waite, T. D. Measurement and implications of floc structure in water and wastewater treatment. *Colloid Surface A* **151**, 27-41, 1999.

Waite, T. D., Cleaver, J. K. and Beattie, J. K. Aggregation kinetics and fractal structure of gamma-alumina assemblages. *J. Colloid Interf. Sci.* **241**, 333-339, 2001.

Wang, D. S., Hong, L., Chunhua, L. and Hongxiao, T. Removal of humic acid by coagulation with nano- Al_{13} . *Wat. Sci. Tech.* **6(1)**, 59-67, 2006.

Wang, D. S., Sun, W., Xu, Y., Tang, H. X. and Gregory, J. Speciation stability of inorganic polymer flocculant-PACl. *Colloid Surface A* **243**, 1-10, 2004.

Wang, D. S., Tang, H. X. and Gregory, J. Relative importance of charge neutralization and precipitation on coagulation of kaolin with PACl: Effect of sulfate ion. *Environ. Sci. Technol.* **36**, 1815-1820, 2002.

Wang, W. Z. and Hsu, P. H. The nature of polynuclear OH-Al complexes in laboratory-hydrolyzed and commercial hydroxyaluminum solutions. *Clays Clay Miner.* **42**, 356-368, 1994.

- Williams, R. A., Peng, S. J. and Naylor, A. In situ measurement of particle aggregation and breakage kinetics in a concentrated suspension. *Powder Tech.* **73**, 75-83, 1992.
- Witten, Jr. T. A. and Sander, L. M. Diffusion-limited aggregation, a kinetic critical phenomenon. *Phys. Rev. Lett.* **47**, 1400-1403, 1981.
- Wood, T. E., Siedle, A. R., Hill, J. R., Skarjune, R. P. and Goodbrake, C. J. Hydrolysis of aluminium. Are all gels created equal? *Better Ceram. Chem. IV, Symp.* **180**, 97-116, 1990.
- Wu, R. M., Lee, D. J., Waite, T. D. and Guan, J. Multilevel structure of sludge flocs. *J. Colloid Interf. Sci.* **252**, 383-392, 2002.
- Wu, X. H., Ge, X. P., Wang, D. S. and Tang, H. X. Distinct coagulation mechanism and model between alum and high Al₁₃-PACl. *Colloid Surface A* **305**, 89-96, 2007.
- Xu, T., Wang, D. S., Liu, H., Lu, Y. Q. and Tang, H. X. Optimization of the separation and purification of Al-13. *Colloid Surface A* **231**, 1-9, 2003.
- Yamamoto, T., Fukushima, T., Kanda, Y. and Higashitani, K. Molecular-scale observation of the surface of polystyrene particles by AFM. *J. Colloid Interf. Sci.* **292**, 392-396, 2005.
- Yan, M. Q., Wang, D. S., Qu, J. H., He, W. J. and Chow, C. W. K. Relative importance of hydrolyzed Al(III) species (Ala, Alb, and Alc) during coagulation with polyaluminum chloride: A case study with the typical micro-polluted source waters. *J. Colloid Interf. Sci.* **316**, 482-489, 2007.
- Ye, C. Q., Wang, D. S., Shi, B. Y., Yu, J. F., Qu, J. H., Edwards, M. and Tang, H. X. Alkalinity effect of coagulation with polyaluminum chlorides: Role of electrostatic patch. *Colloid Surface A* **294**, 163-173, 2007.
- Yu, J. F., Wang, D. S., Ge, X. P., Yan, M. Q. and Yang, M. Flocculation of kaolin particles by two typical polyelectrolytes: A comparative study on the kinetic and flocs structures. *Colloid Surface A* **290**, 288-294, 2006.
- Zhong, Q., Inniss, D., Kjoller, K. and Elings, V. B. Fractured polymer silica fiber surface studied by tapping mode atomic-force microscopy. *Surf. Sci.* **290(1-2)**, L688-L692, 1993.
- Zhou, Y. and Franks, G. V. Flocculation mechanism induced by cationic polymers investigated by light scattering. *Langmuir* **22**, 6775-6786, 2006.

VITA

(1) Background

The author, Jr-Lin Lin, was born on February 9, 1979 in Yunlin, Taiwan. He received a B.S. degree in Water Resource & Environmental Engineering from the Tamkang University, Taipei, Taiwan, in 2001 and then soon initiated his graduate studies focused on sludge conditioning at the Institute of Water Resource & Environmental Engineering, Tamkang University. In 2003, he joined the research group of Dr. Chih-Ping Huang and started his further studies on coagulation behavior of colloidal particles in the Ph.D. programs at the National Chiao-Tung University, Hsinchu, Taiwan.

(2) Publication

(a) Referred Papers

1. **Jr-Lin Lin**, Chihpin Huang, Ching-Ju M. Chin and Jill R. Pan, Coagulation dynamics of fractal flocs induced by enmeshment and electrostatic patch mechanisms. *Water Research* (accepted on August 1, 2008) (SCI, IF: 3.427)
2. **Jr-Lin Lin**, Ching-Ju M. Chin, Chihpin Huang, Jill R. Pan, and Dongsheng Wang, Coagulation Behavior of Al₁₃ Aggregates. *Water Research* (accepted on July 10, 2008) (SCI, IF: 3.427)
3. **Jr-Lin Lin**, Chihping Huang, Jill Ruhsing Pan, and Dongsheng Wang, Effect of Al(III) Speciation on Coagulation of Highly Turbid Water. *Chemosphere*, 72, 189-196, 2008. (SCI, IF: 2.739)
4. Chi-Wang Li, **Jr-Lin Lin**, Shyh-Fang Kang and Chung-Lin Liang, Acidification and alkalization of textile chemical sludge: Volume/solid reduction, dewaterability, and Al(III) recovery. *Separation and Purification Technology*, 42(1), 31-37, 2005. (SCI, IF: 2.142)
5. Chihping Huang, Wen-Shan Lee, Bingqing Zhao and **Jr-Lin Lin**, Effect of coagulation mechanism on membrane filtration characteristics in coagulation-microfiltration process for spent filter backwash water treatment. (submitted to *Water Research*)

(b) Conference Papers

1. **J. L. Lin**, C. J. M. Chin, C. P. Huang and J. R. Pan (2008) "Coagulation behavior of Al_{13} aggregates", Proceedings of 5th International Conference Interfaces Against Pollution 2008, June 1-4, Kyoto, Japan. **(Oral presentation)**
2. J. R. Pan, C. P. Huang and **J. L. Lin** (2007) "Optimization of Sludge Dewatering In Water Treatment Plant: Effects of Polymer Dosing and Dosing Point", Proceedings of IWA Conference: Facing Sludge Diversities: Challenges, Risks and Opportunities, March 28-30, Antalya, Turkey. **(Oral presentation)**
3. **J. L. Lin**, C. P. Huang and J. R. Pan (2006) "Effects of PACl Speciation on Coagulation for High Turbidity Water", The 2nd Pan-Pacific International Workshop on Water Management and Technology, March 20, Taipei, Taiwan. **(Oral presentation)**
4. **林志麟**、黃志彬、秦靜如、袁如馨 "Al₁₃聚集體對高純度聚氯化鋁凝膠羽特性之影響", 第二十四屆自來水研究發表會, 中壢, 民國九十六年十一月。
5. 黃志彬、**林志麟**、吳政倫、李志行 "以MF薄膜處理回收淨水廠砂濾反沖洗水" 第二十一屆自來水研究發表會, 臺北, 民國九十四年十一月。
6. **林志麟**、李奇旺、康世芳 "酸化處理對染整化學污泥減量及其脫水性之影響", 第二十八屆廢水處理技術研討會, 台中, 民國九十二年十二月。
7. 康世芳、劉明仁、**林志麟** "台灣地區淨水污泥餅特性及資源化之發展趨勢", 第十九屆自來水研討會, 臺北, 民國九十一年十一月。

(c) 國內期刊論文

1. 黃志彬、**林志麟**、陳韋弘 "聚氯化鋁 Al_{13} 含量對高濁度原水濁度移除之影響" 自來水會刊, 24(3), pp 95-106, 民國九十四年。
2. 康世芳、廖志祥、陳雅君、**林志麟** "酸化處理化學污泥以減量及回收凝劑", 環保月刊, 2(8), pp 132-140, 民國九十年。